Tampere University

MARKKU HANNULA

Atomic Layer Deposited Titanium Dioxide Thin Films for Photoelectrochemical Water Splitting

Tampere University Dissertations 165

Tampere University Dissertations 165

MARKKU HANNULA

Atomic Layer Deposited Titanium Dioxide Thin Films for Photoelectrochemical Water Splitting

ACADEMIC DISSERTATION
To be presented, with the permission of
the Faculty of Engineering and Natural Sciences
of Tampere University,
for public discussion in the Auditorium SA203
of the Sähkötalo Building, Korkeakoulunkatu 3, 33720 Tampere,
on November 25th, 2019, at 12 o'clock.

ACADEMIC DISSERTATION
Tampere University, Faculty of Engineering and Natural Sciences
Finland

Responsible supervisor and Custos
Professor
Mika Valden
Tampere University
Finland

Pre-examiners
Professor
Kari Laasonen
Aalto University
Finland

Adjunct Professor
Pekka Laukkanen
University of Turku
Finland

Opponent
Professor
Joachim Schnadt
Lund University
Sweden

Cover design: Roihu Inc.

ISBN 978-952-03-1332-6 (print)
ISBN 978-952-03-1333-3 (pdf)
ISSN 2489-9860 (print)
ISSN 2490-0028 (pdf)
http://urn.fi/URN:ISBN:978-952-03-1333-3

PunaMusta Oy – Yliopistopaino
Tampere 2019

PREFACE

The experimental research presented in this Thesis was mostly carried out in the Surface Science Laboratory in Tampere University of Technology (Tampere University since 2019) during the years 2015–2019. A small part of the measurements was performed in the MAX IV Laboratory (Lund, Sweden).

First and foremost, I want to thank the Head of the Laboratory, my supervisor Professor Mika Valden for the opportunity to work as a part of his research group and also for the expertise and guidance during all these years ranging from the first summers as a research assistant all the way to the completion of this Thesis. I want to thank Dr. Harri Ali-Löytty for the numerous fruitful conversations about the research topic and also for his assistance with the photoelectrochemical research and the preparation of the manuscripts. I want to thank Dr. Kimmo Lahtonen for the extensive introduction into the details of electron spectroscopic methods during all these years. I am also grateful to all my colleagues who have contributed to the experiments and provided an uplifting atmosphere in the group. Special thanks belong to M.Sc. Lauri Palmolahti, M.Sc. Jesse Saari, Dr. Leena Vuori, and Dr. Marko Ahonen. I want to thank the staff of the MAX IV Laboratory, especially Dr. Alexei Zakharov, for making the SR-PEEM measurements possible.

I am grateful for the financial support provided by the TUT's Graduate School, the Academy of Finland, The Finnish Foundation for Technology Promotion (TES), the National Graduate School in Material Physics (NGSMP), KAUTE Foundation, Emil Aaltonen Foundation, Business Finland, and the Doctoral training network in condensed matter and materials physics (CMMP). This work is a part of the Academy of Finland Flagship Programme, Photonics Research and Innovation (PREIN).

Finally, I want to thank my family and friends for their support during all these years and for providing positive variety and balance for work.

Tampere, November 2019

Markku Hannula

ABSTRACT

Increasing energy consumption is one of the greatest challenges the humankind is facing in the 21st century. Fossil fuels cannot be used to solve the problem due to the already alarming CO_2 concentration in the atmosphere and consequent global warming. A more sustainable solution must be found by replacing the polluting oil and coal based energy production with clean renewable energy sources. From these solar energy is one of the most promising due to its practically unlimited capacity. However, the capacity shows strong fluctuations due to the day/night cycle and intermittent cloud coverage, which necessitates efficient technologies for storing and transporting solar energy. This can be achieved by storing the energy directly into chemical bonds. In photoelectrochemical water splitting water molecules are dissociated into hydrogen and oxygen molecules. Hydrogen has the highest energy density of all fuels and can be stored and converted into electricity on demand. The water splitting reaction takes place on semiconducting metal oxide photoelectrodes.

This Thesis focuses on studying and optimizing the properties of atomic layer deposited (ALD) TiO_2 photoanodes. Titanium dioxide is a versatile material for both light absorbing photoactive layers and for passivating and protecting other semiconductor materials used in photoelectrodes. The ALD method makes it possible to accurately control the thickness of the TiO_2 film and to deposit conformal homogeneous layers even on highly 3D-structured substrates. However, TiO_2 possesses some challenges, as the chemical stability of the as-deposited ultra-thin films is poor in alkaline electrolytes and the large band gap prevents light absorption outside the ultraviolet region. Based on the results of this Thesis, these disadvantages can be remedied or mitigated with thermal treatments following the growth of the TiO_2 thin film. Annealing the films in vacuum at 500–900 °C leads to the formation of O^- species, which were shown to stabilize the TiO_2 film while maintaining the amorphicity. On the other hand, it was found that annealing in oxidizing conditions leads to the crystallization of the film with simultaneous improvement in both stability and catalytic properties. Additionally, TiO_2 derived microstructured TiSi was studied as an intermediate layer for optimizing charge carrier separation and charge transfer in a TiO_2/TiSi/Si heterojunction photoanode. As evident by the results of this Thesis, metal-like TiSi islands can act as effective charge transfer mediators and recombination centers in Z-scheme photoanodes.

This Thesis underlines the importance of the knowledge-based approach to optimize the molecular and electronic properties of the ALD grown thin films in general and in particular, the properties of the TiO_2 thin film for water splitting reaction. Especially the electron spectroscopic techniques in both traditional spectroscopic mode and more novel imaging spectromicroscopic mode will enable a solid base for understanding the optoelectronic properties of various photonic materials for future applications.

CONTENTS

NOMENCLATURE

Abbreviations

AFM	Atomic force microscopy
AL	Attenuation length
ALD	Atomic layer deposition
ASTM	American Society for Testing and Materials, an international standards organization
CB	Conduction band
CBM	Conduction band minimum
CCD	Charge-coupled device
CE	Counter electrode
CLS	Core level shift
CV	Cyclic voltammetry
CVD	Chemical vapor deposition
DI-H_2O	Deionized water
EEC	Electrical equivalent circuit
EF-PEEM	Energy-filtered photoemission electron microscopy
EIS	Electrochemical impedance spectroscopy
ESCA	Electron spectroscopy for chemical analysis
FoV	Field of view
FXS	Focused X-ray source
GIXRD	Grazing incidence X-ray diffraction
HER	Hydrogen evolution reaction
HSA	Hemispherical energy analyzer
IDEA	Imaging double energy analyzer
IMFP	Inelastic mean free path
IPCC	International Panel on Climate Change

IR	Infrared
LEEM	Low energy electron microscopy
MCP	Micro channel plate
NHE	Normal hydrogen electrode
OER	Oxygen evolution reaction
PCA	Principal component analysis
PEC	Photoelectrochemical
PEEM	Photoemission electron microscopy
PES	Photoelectron spectroscopy
ppm	Parts per million
PS	Photosystem
PV	Photovoltaic
RE	Reference electrode
RHE	Reversible hydrogen electrode
sccm	Standard cubic centimeters per minute
SCLS	Surface core level shift
SEM	Scanning electron microscopy
SNR	Signal-to-noise ratio
SPELEEM	Spectroscopic low energy electron microscopy
SR-PEEM	Synchrotron radiation induced photoemission electron microscopy
SR-PES	Synchrotron radiation induced photoelectron spectroscopy
STH	Solar-to-hydrogen
TDMAT	Tetrakis(dimethylamido)titanium(IV) ($Ti(N(CH_3)_2)_4$)
UHV	Ultra-high vacuum
UPS	Ultraviolet photoelectron spectroscopy
UV	Ultraviolet
VB	Valence band
VBM	Valence band maximum
WE	Working electrode
XAS	X-ray absorption spectroscopy
XPS	X-ray photoelectron spectroscopy

Symbols

A	Absorbance
barn	Unit of photoionization cross section (1 barn $= 10^{-28}$ m^2)
c	Speed of light ($c = 299\ 792\ 458$ m s^{-1})
e	Elementary charge ($e = 1.6022 \cdot 10^{-19}$ C)
E	Electric field
E_{acc}	Accelerating electric field
E_b	Electron binding energy
E^0_{cell}	Electrochemical voltage of a cell under standard conditions
E_{dec}	Decelerating electric field
E_F	Fermi level
E_{Fn}	Quasi Fermi level for electrons
E_{Fp}	Quasi Fermi level for holes
$E_{F,s}$	Sample Fermi level
$E_{F,sp}$	Spectrometer Fermi level
E^0_{ox}	Oxidation potential under standard conditions
E_p	Pass energy
E^0_{red}	Reduction potential under standard conditions
E_{vac}	Vacuum level
eV	Electron volt (unit of energy) (1 eV $= 1.6022 \cdot 10^{-19}$ J)
F	Faraday constant ($F = 96485.33$ C mol^{-1})
ΔG	Gibbs free energy change
h	Planck's constant ($h = 6.626 \cdot 10^{-34}$ J s)
$h\nu$	Energy of electromagnetic radiation
HV	High voltage
I	Intensity of a photoelectron peak
I_{emis}	Emission current
I_{fil}	Filament current
Kα	Notation for X-rays emission when an electron relaxes from $n = 2$ to $n = 1$ orbital

K, L, M,...	Labeling system for the core levels in an atom, corresponds to principal quantum numbers n = 1, 2, 3,...
n	Number of electrons in moles
n	Principal quantum number
P	Pressure
px	Pixel
R	Reflectance
S	Relative sensitivity factor
T	Transmittance
T_E	Transmission function of an energy analyzer
V_{acc}	Acceleration voltage
V_{dec}	Deceleration voltage
z	Electron excitation depth

Symbols, Greek alphabet

α	Absorption coefficient
ϵ_0	Vacuum permittivity ($\epsilon_0 = 8.854188 \cdot 10^{-12}$ F m^{-1})
θ	Electron emission angle with respect to surface normal
λ	Attenuation length
λ	Wavelength
ν	Frequency of electromagnetic radiation
σ	Photoionization cross section
ϕ_s	Sample work function
ϕ_{sp}	Spectrometer work function

LIST OF PUBLICATIONS

I. **Hannula, M.**, Ali-Löytty, H., Lahtonen, K., Sarlin, E., Saari, J., and Valden, M. Improved stability of atomic layer deposited amorphous TiO_2 photoelectrode coatings by thermally induced oxygen defects. *Chemistry of Materials*, 30, p. 1199–1208, 2018.

II. Ali-Löytty, H., **Hannula, M.**, Saari, J., Palmolahti, L., Bhuskute, B., Ulkuniemi, R., Nyyssönen, T., Lahtonen, K., and Valden, M. Diversity of TiO_2: Controlling the molecular and electronic structure of atomic layer deposited black TiO_2. *ACS Applied Materials and Interfaces* 11, p. 2758–2762, 2019.

III. **Hannula, M.**, Lahtonen, K., Ali-Löytty, H., Zakharov, A. A., Isotalo, T., Saari, J., and Valden, M. Fabrication of topographically microstructured titanium silicide interface for advanced photonic applications. *Scripta Materialia*, 119, p. 76–81, 2016.

IV. **Hannula, M.**, Ali-Löytty, H., Lahtonen, K., Saari, J., Tukiainen, A., and Valden, M. Highly efficient charge separation in model Z-scheme $TiO_2/TiSi_2/Si$ photoanode by micropatterned titanium silicide interlayer. *Acta Materialia*, 174, p. 237–245, 2019.

AUTHOR'S CONTRIBUTION

This Thesis is based on 4 peer reviewed journal articles. All of them are related to the application and modification of atomic layer deposited TiO_2, which is used as a photoelectrode material in artificial photosynthesis. The detailed contributions of the author of this Thesis and all co-authors are provided below.

Paper I: The Paper focuses on how the photoelectrochemical (PEC) stability of an ALD grown TiO_2 film can be modified by thermal annealing. The sample preparation and treatments were designed by the author and K. Lahtonen. The author performed all sample treatments that were made in ultra-high vacuum and also conducted all X-ray photoelectron spectroscopy (XPS) and ultraviolet photoelectron spectroscopy (UPS) measurements and analyzed the data. The ALD films were grown by K. Lahtonen and J. Saari. H. Ali-Löytty performed the PEC experiments. E. Sarlin carried out the X-ray diffraction measurements. The author wrote most of the manuscript with help from H. Ali-Löytty, and K. Lahtonen. M. Valden co-authored the manuscript and supervised the work.

Paper II: The Paper concentrates on thermal modification of ALD grown TiO_2 in oxidizing conditions and subsequent effects on PEC stability and photoactivity. The author participated in the planning of the experiments and carried out part of the XPS studies and all UPS studies. The author also participated in the manuscript preparation. H. Ali-Löytty planned the experiments and wrote most of the manuscript. J. Saari and K. Lahtonen made the ALD depositions. H. Ali-Löytty and B. Bhuskute performed the PEC experiments and analysis. L. Palmolahti operated the scanning electron microscope (SEM) and R. Ulkuniemi made the conductivity measurements. M. Valden co-authored the manuscript and supervised the work.

Paper III: The Paper presents how an atomic layer deposited (ALD) TiO_2 ultrathin film can be transformed into a highly topographically microstructured TiSi layer. The author designed the experiments and carried out all laboratory based photoelectron spectroscopy measurements

and the TiSi layer fabrication. The author also performed the data analysis and wrote most of the manuscript. K. Lahtonen and J. Saari grew the ALD films. H Ali-Löytty and K. Lahtonen participated in the writing of the manuscript. T. Isotalo carried out the SEM and atomic force microscopy (AFM) measurements. A. A. Zakharov conducted the synchrotron radiation induced photoemission electron microscopy measurements based on the instructions given by the author. M. Valden co-authored the manuscript and supervised the work.

Paper IV: The Paper focuses on establishing an exhaustive understanding of the band structure of a TiO_2/Si heterojunction with and without a microstructured TiSi interlayer. The author planned the experiments together with H. Ali-Löytty. K. Lahtonen and J. Saari made the ALD TiO_2 depositions. The author carried out all XPS and UPS measurements and the TiSi layer fabrication. The author also performed the electron spectroscopy data analysis and wrote the manuscript excluding the PEC section. H. Ali-Löytty performed the PEC experiments and the related data analysis. A. Tukiainen made the grazing incidence X-ray diffraction measurements. M. Valden co-authored the manuscript and supervised the work.

1 INTRODUCTION

Modern technological development and globally rising standard of living set an ever-increasing challenge of supplying the mankind with sufficient amount of energy. The world total energy consumption is about 161 petawatthours with an annual increase of 2.9 % [1, 2]. From this energy 34 % is produced from oil, 27 % from coal and 24 % from natural gas. In addition to the limited reserves, the burning of these energy sources releases vast quantities of CO_2. In 2018 the total CO_2 emissions were almost 34 gigatons with an annual 2.0 % growth [2]. CO_2 is one of the primary greenhouse gases in Earth's atmosphere, and since the beginning of the industrial revolution its concentration has risen from 280 to 414 ppm, with a current increase of 2.2 ppm per year [3]. According to the International Panel on Climate Change (IPCC), a CO_2 level above 450 ppm might cause a global warming of more than 2 °C. This would have severe impacts on ecosystems and human society. [4] The human-induced warming has already reached approximately 1 °C above the pre-industrial levels, and the temperature is increasing 0.1–0.3 °C per decade [5].

A sharp reduction in global CO_2 emissions is required to stop the harmful climate prospects. One solution is a significant increase in renewable energy sources. At the moment renewable energy (solar, wind, geothermal, biomass, waste, and biofuels) constitutes only 4.5 % of all energy consumption [2]. From this 25 % is produced by solar energy. However, the annual growth rate of 28.9 % in solar energy (in 2018) is the fastest of any energy form. Additionally, the exploitable capacity of solar energy is practically unlimited. For example, all current energy consumption could be fulfilled by covering 0.15 % of Earth's surface with 10 % efficient solar panels. In practice, sustainable energy production of course requires a combination of different renewable sources.

One major limitation in solar energy is its intermittent nature because of the day–night cycle and clouds. The fluctuating production and consumption rates are demanding for the electricity transmission networks, and thus large-scale storage

solutions have to be developed and implemented. One promising possibility is to store solar energy in the chemical bonds of molecules in solar fuels. Compared to other storage solutions, such as batteries or gravity-based systems, solar fuels excel in both energy density and ease of transportation. [4] In terms of energy density and also chemical simplicity, H_2 is the most effective solar fuel. H_2 is also abundant, since it can be generated from normal water. Conversion and storage of solar energy into the chemical bonds of H_2 by photoelectrochemical (PEC) water splitting has become an intense research subject. The phenomenon was first discovered by Fujishima and Honda in 1972 on n-type rutile TiO_2 photoelectrode surfaces [6]. Since then the same reaction has been observed and studied on multiple different semiconducting metal oxide photocatalyst surfaces under laboratory conditions. Unfortunately, large-scale cost-effective and efficient hydrogen production systems that can compete with fossil fuels have remained elusive. Currently the best PEC systems have reached solar-to-hydrogen (STH) efficiencies of 5–18 % and the ongoing research keeps improving the performance [7]. Despite this, the energy produced with PEC water splitting is still significantly more expensive than the average electricity prices [8]. The increasing environmental taxes and exhaustible resources of fossil fuels together with the improved PEC efficiency and prolonged lifetime are, however, expected to make the solar energy based hydrogen production a viable option in the future.

The fundamental principle of PEC water splitting is that an aqueous electrolyte is in direct contact with the photoelectrode surface. Incoming solar illumination generates electron–hole pairs inside the electrode material, and an internal electric field separates these charge carriers towards cathodic and anodic parts of the electrode. Electrons traveling to the cathode reduce water molecules into H_2 in hydrogen evolution reaction (HER), and simultaneously holes traveling to the anode oxidize hydroxyl groups into O_2 in oxygen evolution reaction (OER). This direct photoelectrochemical decomposition of water sets strict requirements for the electrode surfaces: the semiconductor materials must generate sufficient voltage for water splitting, the band gap of the electrodes must be small enough to absorb a significant portion of the incoming solar irradiation, the semiconductor band edge locations must straddle the hydrogen and oxygen redox potentials, the electrode surfaces must be stable against photocorrosion under prolonged exposure to electrolyte and the material has to facilitate effective charge transfer across the photoelectrode–electrolyte interface [9]. In large-scale energy production the material has to be also economically feasible compared to the value of the generated energy. Atomic layer

deposited (ALD) TiO_2 fulfills many of these requirements and has attracted tremendous research interest as a photoanode material [10–19] due to its abundancy, cost-effectiveness and non-toxicity. Additionally, the ALD technique enables easy and accurate thickness control and perfect conformality of TiO_2 even on nanostructured surfaces.

However, TiO_2 has also some significant challenges. The band gap of TiO_2 varies approximately from 3.0 to 3.6 eV [20–22]. This corresponds to the UV region of the solar spectrum, which limits the amount of absorbed energy. The problem can be mitigated by band gap engineering, where new electronic states are generated inside the gap. This can be done, for example, by doping the material [23–26] or by generating defect states [27–30]. Another option is to use TiO_2 in combination with other smaller band gap semiconductors, such as Si or GaAs [10, 11, 16, 31, 32]. In this case TiO_2 can be used for collecting the UV region of the solar spectrum or as a protective top coating. Both of these options require firm chemical stability and efficient charge transfer between the ultra-thin TiO_2 film and the underlying semiconductor. An additional setback is that ALD grown amorphous TiO_2 is not chemically stable under alkaline conditions. Amorphous phase is otherwise more favorable in many water splitting applications compared to the crystalline polymorphs anatase or rutile. Thus amorphicity preserving post-treatments are required.

1.1 Research objectives and scope of the Thesis

The aim of this Thesis is to improve the prospects of ALD grown TiO_2 to be used as a photoelectrode material in water splitting devices of practical relevance. This photoelectrochemical method could provide a clean and cost-effective solution for storing solar energy into the chemical bonds of H_2 molecules. The specific objectives of the Thesis are

1. to improve the chemical stability of TiO_2 under alkaline conditions by post-treating the ALD-grown film in reductive or oxidative conditions.
2. to adjust the electronic structure and optical absorption properties of TiO_2 for optimizing the photocurrent for photoelectrochemical water splitting.
3. to study the conversion of amorphous TiO_2 into TiSi, which can be used as an intermediate layer in multilayered photoanode structures for optimizing the charge carrier separation and charge transfer across the heterojunction interface.

Aside from advancing the development of TiO_2 based photoelectrodes for water splitting, the second aim of this Thesis is to highlight the diversity and usefulness of spectromicroscopy for studying the localized elemental composition and electronic properties of the semiconductor photoelectrode surfaces. Photoemission electron microscopy, especially in energy-filtered mode, is a rather novel research method compared to many other electron spectroscopic and microscopic techniques. The facilities are not common, although some synchrotron radiation and laboratory photon source based facilities exist. Also careful and comprehensive image data analysis is scarce in literature. For this reason, the experimental chapter of the Thesis incorporates an extensive description of the physical principles of spectromicroscopy and also a detailed explanation of the applied image enhancement and analysis procedures.

1.2 Structure of the Thesis

The Thesis explains the basics of photoelectrochemical water splitting concentrating especially on the material properties of TiO_2 based semiconductor photoanodes. Also the sample preparation and novel research methods play a key role in this work. The Thesis is divided into the following chapters:

Chapter 2 introduces the reader to the basic concepts of photoelectrochemical water splitting and hydrogen production. The Chapter explains the chemical reactions and physical properties of solar illumination assisted water dissociation. Emphasis is put on TiO_2 based n-type photoanodes and their electronic properties. Also the structure of different photoelectrochemical cell configurations is discussed.

Chapter 3 provides a comprehensive description of the experimental methods used in this work. The first part concentrates on the atomic layer deposition, especially on the growth of TiO_2 from tetrakis(dimethylamido)-titanium(IV) precursor. The second part explains the physical principles of photoelectron spectroscopy and specifically the characteristics of photoemission electron microscopy. Also the data analysis of both conventional spectroscopic data and higher-dimensional spectromicroscopic data are discussed. The third part is a short overview of the photoelectrochemical methods.

Chapter 4 describes the key findings of this work. The first part of the results focuses on the post-treatments of atomic layer deposited TiO_2 film in reductive or oxidative conditions. The effect of these treatments on the chemical stability, conductivity, and solar absorption is discussed in the context of water splitting photoanodes. The second part shows the results of a more drastic treatment of TiO_2 film, where the oxide is converted into microstructured TiSi islands. TiSi is applied as an interlayer between a silicon substrate and TiO_2 overlayer, where it alters the band alignment and charge transfer properties of the heterojunction.

Chapter 5 concludes the Thesis with a summary of the key results. The Chapter also gives a brief outlook of the research that could advance the field in the future.

Original research Papers

A detailed description of the conducted research can be found in the four original research Papers at the end of this Thesis.

Paper **I** describes the reductive post-treatments of TiO_2 films. Two methods, vacuum annealing and atomic H exposure, are compared in the preparation of partially reduced photoanode surface coatings. In Paper **II** the thermal post-treatments are made in oxidative conditions. This leads to the crystallization of amorphous TiO_2 into rutile TiO_2, thus reshaping the chemical stability and optical absorption properties. Paper **III** focuses on how an atomic layer deposited TiO_2 can be converted into microstructured TiSi islands by thermal annealing in vacuum. Paper **IV** can be considered as an extension to Paper **III**. Different TiSi structures are fabricated by modifying the original TiO_2 film thickness. The effect of a TiSi interlayer in a TiO_2/TiSi/Si photoanode structure is studied for optimizing the charge carrier separation and photocurrent onset potential.

2 PHOTOELECTROCHEMICAL WATER SPLITTING

This chapter is an introduction to the photoelectrochemical (PEC) water splitting, where the oxidation of water molecules leads into the formation of O_2 and H_2 gases. The reaction takes place on photoactive electrode surfaces where solar illumination provides the energy required for breaking the chemical bonds. The chapter concentrates especially on TiO_2 based photoanode materials, and their advantages and challenges in collecting solar light and providing an electrode–electrolyte interface with suitable energetics and chemical stability.

2.1 Operation of a photoelectrochemical cell

The most crucial components in a PEC cell are the electrodes which absorb the incoming solar irradiation and convert its energy to electron–hole pairs. The electrodes must provide an electric field, which separates the electrons and holes to the opposing sides of the cell. Typically the holes are transported to a semiconducting photoanode for oxygen evolution and the electrons to a semiconducting or metallic photocathode for hydrogen evolution. For alkaline electrolyte the chemical reactions are the following:

$$\begin{aligned} 4\ H_2O + 4\ e^- &\rightleftharpoons 2\ H_2 + 4\ OH^- && E^0_{red} = -0.828\ \text{V} \\ 4\ OH^- + 4\ h^+ &\rightleftharpoons 2\ H_2O + O_2 && E^0_{ox} = -0.401\ \text{V} \\ \hline 2\ H_2O &\rightleftharpoons 2\ H_2 + O_2 && E^0_{cell} = -1.229\ \text{V}, \end{aligned} \tag{2.1}$$

where the reduction and oxidation potentials (E^0_{red} and E^0_{ox}, respectively) are measured against a normal hydrogen electrode (NHE).

The Gibbs free energy change for the total reaction can be calculated by

$$\Delta G = -nFE^0_{cell}, \tag{2.2}$$

where n is the number of electrons in moles transferred in the reaction, F is the Faraday constant ($F = 96485.33\,\mathrm{C\ mol^{-1}}$), and E^0_{cell} is the electrochemical voltage of the cell. At standard conditions this equates to $\Delta G = 237$ kJ/mol H_2. The positive Gibbs free energy change implies that the reaction proceeds thermodynamically uphill. In other words, external energy is required to drive the reaction. This is in contrast to photocatalytic reactions, such as photo-assisted degradation of pollutants, for which the Gibbs free energy is decreased. [4, 33]

The operation of a PEC cell requires that the energy of the photoexcited electrons surpasses the thermodynamic potential of the water splitting reaction, i.e. 1.229 eV as calculated from the cell voltage. The maximum wavelength λ of the incoming photons can be calculated by

$$\lambda = \frac{hc}{E^0_{cell}}, \tag{2.3}$$

where h is the Planck's constant ($h = 6.626 \cdot 10^{-34}$ J s) and c is the speed of light ($c = 299\ 792\ 458$ m $\mathrm{s^{-1}}$). For $E^0_{cell} = 1.229$ eV this equals to approximately 1000 nm, which corresponds to the whole UV–visible and even near-infrared range of the solar irradiance. At sea level the total solar irradiance is 1000 $\mathrm{W/m^2}$, of which 78 % has a suitable wavelength for driving the water splitting reaction (Figure 2.1).

However, the true available power is considerably less than the incoming 780 $\mathrm{W/m^2}$. Firstly, the amount of energy that exceeds the band gap of the photoelectrode is lost thermally. Secondly, the above-calculated theoretical 1.229 eV energy is not sufficient for real-life water splitting. The electron transfer processes at the semiconductor–electrolyte interface produce losses due to the concentration and kinetic overpotentials needed to drive the OER and HER [35, 36]. Thus the practical required photon energy is typically considered to be 1.6–2.4 eV [35, 37, 38]. This corresponds to wavelength limit of 775–515 nm.

Another limiting factor in the energy conversion efficiency is the absorption of the photoelectrode material. The absorbance A of a material can be defined as

$$A = -\log_{10}\frac{T}{1-R}, \tag{2.4}$$

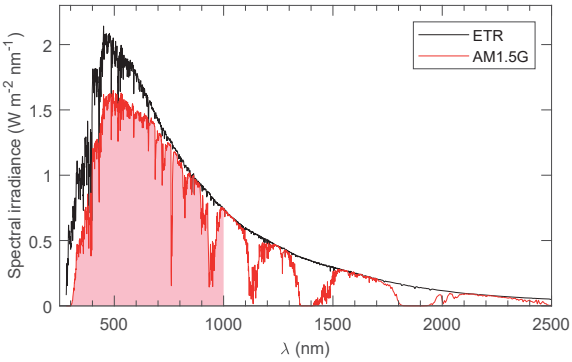

Figure 2.1: *Solar irradiance outside the atmosphere (extraterrestrial radiation, ETR) and through an air mass 1.5 global (AM1.5G) according to the ASTM G-173-03 [34]. The shaded area illustrates the irradiance that has theoretically sufficient energy for electrochemical water splitting.*

where T is the transmittance and R is the reflectance of the material. A thicker layer usually increases the absorption, but may impede the charge transfer properties.

The absorption coefficient of a material can be defined by converting the logarithm in Equation (2.4) from base 10 to the natural logarithm and dividing the absorbance by the thickness x of the absorbing layer:

$$\alpha = -\frac{\ln(10)}{x} \log_{10} \frac{T}{1-R}. \tag{2.5}$$

The inverse of the absorption coefficient (α^{-1}) corresponds to the distance that absorbs 63 % (i.e. $1-1/e$) of the incoming light. This is typically close to the semiconductor thickness where the total impact of charge carrier generation and charge transfer is optimized [9].

The absorption coefficient can be utilized in determining the optical band gap of a semiconductor by drawing a Tauc plot. Here the quantity $(\alpha h\nu)^n$ is plotted against the photon energy $h\nu$ and the intersection of the slope with the $h\nu$-axis corresponds to the band gap value. The exponent n can take on values of 3, 2, 3/2, or 1/2, corresponding to indirect forbidden, indirect allowed, direct forbidden, and direct allowed transitions, respectively. [9, 39]

2.2 Electronic structure and properties of TiO_2

Titanium dioxide has been one of the most studied metal oxide semiconductor materials for water splitting applications since the phenomenon was originally discovered by Fujishima and Honda in 1972 [6]. TiO_2 is an n-type semiconductor with a band gap varying from 3.0 to 3.6 eV (corresponding to wavelengths from 413 to 344 nm) depending on the crystal structure, and the conduction band minimum (CBM) located near the Fermi level (E_F) (Figure 2.2) [20–22]. The large band gap limits the photoactivity of TiO_2 and permits the solar absorption only at UV wavelengths. This can be mitigated by narrowing the band gap by, e.g., generating defects in the material [27–30] or by doping it with other elements [23–25]. On the other hand, the low absorption can be beneficial when TiO_2 is applied as a protective layer on top of other more photoactive semiconductor materials, such as Si or GaAs (Figure 2.2). Typically the chemical stability against photocorrosion increases with increasing band gap, which makes TiO_2 an excellent material for this application. [10, 11, 16, 31]

In general, TiO_2 has a suitable band alignment for water oxidation, as the valence band maximum (VBM) is located at a higher potential than the water oxidation potential. This enables hole transfer from the electrode to the water molecules. Also, the TiO_2 reduction potential (-0.75 V vs. RHE [40]) is below the required water oxidation potential (1.23 V vs. RHE), which prevents the reduction of the electrode itself under operating conditions. For several other photoelectrode materials, such as Si and GaAs in Figure 2.2, either the band alignment is not suitable for water

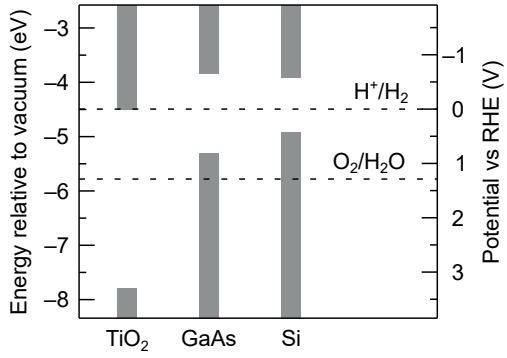

Figure 2.2: *The gray bars illustrate the conduction band (CB) and valence band (VB) positions of selected typical photoelectrode semiconductor materials at pH = 0. The dashed lines show the redox potentials for O_2/H_2O and H^+/H_2 pairs. [35, 40, 41].*

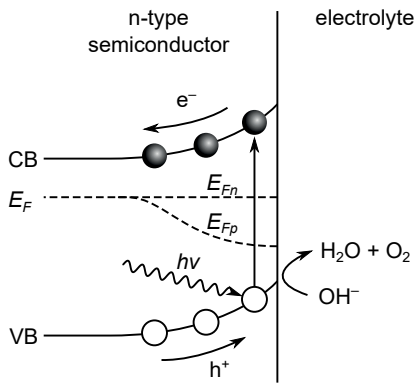

Figure 2.3: *Schematic illustration of an n-type semiconductor in contact with liquid electrolyte. Near the surface of the semiconductor the valence and conduction bands (VB and CB) bend upward due to the electric field. This ensures efficient charge carrier separation of the photoexcited electron–hole pairs. Holes are guided towards the semiconductor–electrolyte interface for water oxidation while electrons drift towards the bulk phase. The photoexcitation of electrons generates imbalance in charge carrier concentration, which separates the Fermi level into quasi Fermi levels for electrons (E_{Fn}) and holes (E_{Fp}).*

oxidation or the oxidation potential of the material itself is so low, that the required potential would lead to the oxidation and degradation of the electrode.

Natural TiO_2 can be found in three crystalline phases: rutile, anatase and brookite. Especially the first two structures have been studied extensively for decades. In recent years, however, the different amorphous phases of TiO_2 have started to attract more scientific interest [10, 21, 42, 43]. The more routine utilization of ALD has facilitated cost-effective and reproducible fabrication of stoichiometric or well-defined defective amorphous TiO_x with $x \leq 2$ [11]. One such material is the oxygen deficient or disordered black TiO_x, where the defects increase the charge carrier mobility and make the oxide electronically "leaky" [13, 21, 44]. Thus the TiO_x layer does not inhibit the charge transfer when used as a protective film between a small band gap semiconductor and electrolyte. Additionally, as the name 'black' implies, the material absorbs a larger portion of the visible light than conventional crystalline white TiO_2 thus making it more effective photocatalyst material.

Undoped TiO_2 is an n-type semiconductor [45], which exhibits upward band bending at the semiconductor–electrolyte interface (Figure 2.3). This makes TiO_2 photoelectrodes suitable for supporting the OER, as the internal electric field within the spacecharge region ensures rapid charge carrier separation by guiding the photogen-

erated holes towards the electrode–electrolyte interface while steering the excited electrons towards the bulk phase.

2.3 Structure of a photoelectrochemical cell

The most basic PEC cell can be constructed from a single p- or n-type semiconductor electrode (Figure 2.4(a)). However, in many cases a single large band gap photoelectrode is not sufficient for absorbing adequate amount of photons at energies high enough for water splitting (> 1.6 eV). This restriction can be overcome by adding two or more smaller band gap semiconductors in series (Figure 2.4(b)). These semiconductors can have complementary absorption properties for different wavelength ranges of the solar irradiation [35]. This tandem configuration enables the individual tailoring of valence and conduction band edge locations for both HER

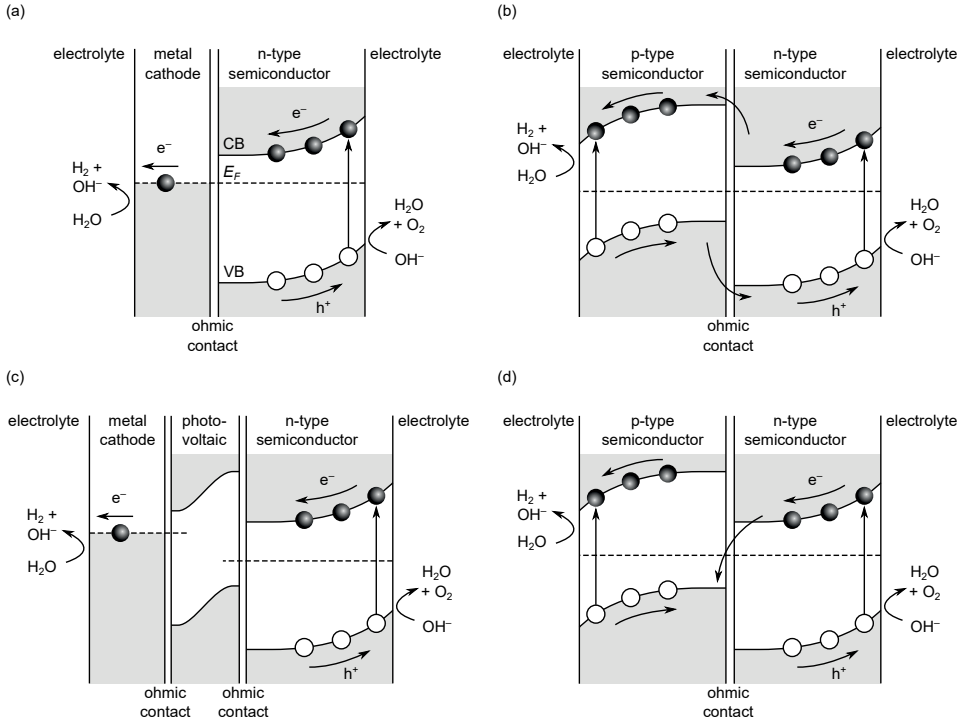

Figure 2.4: *Energy diagrams for different PEC configurations: (a) a single band gap cell with n-type anode and metal cathode, (b) a dual band gap cell with n-type anode and p-type cathode, (c) a single n-type photoelectrode integrated with a PV cell for additional bias voltage, (d) a dual band gap Z-scheme cell with metallic recombination interlayer. [33, 35]*

and OER as the reactions take place at separate semiconductor–liquid interfaces. An alternative method is to combine a single photoanode/cathode in series with a photovoltaic (PV) cell that provides the additional bias required for the water splitting reaction (Figure 2.4(c)).

From the research perspective an additional benefit of the tandem or separate PV configuration is that the cell performance can be studied in sections, such as in this Thesis where the attention is paid mostly to the OER reaction at the photoanode surface. The potential difference provided by the photocathode or an internal photovoltaic cell can be replaced by an external bias voltage.

A more novel PEC configuration is the so-called Z-scheme structure [33], which mimics the charge carrier path of the natural photosynthesis. The structure comprises of two semiconductors with a type II band alignment (Figure 2.4(d)). This allows the reduction of the semiconductor band gaps while still making the CB potential more negative and the VB potential more positive [33, 46, 47]. In an all-solid-state Z-scheme system the photogenerated electrons from the CB of the photosystem I (PS I) are recombined with the photogenerated holes at the VB of the PS II. Metal or metal-like particles, such as Au, Ag, or TiSi can be employed as recombination centers at the interface between the two semiconductors [48–50], [Paper **IV**].

In Z-scheme systems the charge transfer is more favorable compared to typical type II heterojunction used in a tandem PEC configuration. This can be explained by the electrostatic attraction between the electrons and holes across the interface [33]. The charge transfer path of a Z-scheme cell requires that energy of the CB in PS I is higher than the energy of the VB in PS II. TiO_2 is an excellent PS II material (anode) for Z-scheme because the CB located close to the Fermi level.

3 ATOMIC LAYER DEPOSITION AND ANALYSIS OF TiO_2 FILMS

This chapter describes the preparation and modification procedures that were utilized for the TiO_2/Si samples studied in this work. Atomic layer deposition (ALD) was used for growing the TiO_2 ultra-thin films. The films were modified by various oxidative and reductive treatments that affected their chemical composition, oxidation state, electronic structure, crystallinity and optical properties. The samples were mainly studied with photoelectron spectroscopy (PES) due to its surface sensitivity and ability to differentiate the chemical states of the elements. PES was employed in several different modes including traditional X-ray photoelectron spectroscopy (XPS, also known as electron spectroscopy for chemical analysis, ESCA), ultraviolet photoelectron spectroscopy (UPS), synchrotron radiation induced photoelectron spectroscopy (SR-PES), and photoemission electron microscopy (PEEM). Also photoelectrochemical (PEC) measurements played an important role for determining the in situ stability and photoactivity of the modified TiO_2 films.

3.1 Sample preparation

3.1.1 Cleaning of Si substrates in vacuum

Most of the TiO_2 films studied in this work were grown on P-doped n-type Si(100) single crystal wafers. Special attention was paid on cleaning the substrate surface prior to TiO_2 deposition. Traditionally Si surface cleaning has been performed by wet chemistry using a combination of hot alkaline and acidic hydrogen peroxide solutions and hydrofluoric acid. This proces known as RCA cleaning [51,52] is effective for removing organic contaminants and the native oxide film. However, it does not affect the bulk impurities, especially the detrimental Ni and Cu contamination [53]. It also requires an additional ex situ step in a process where other treatments can

be made in a well-controlled vacuum environment. To overcome these limitations, a thermal annealing and atomic hydrogen based cleaning procedure was developed to remove both the surface contamination, including the native oxide, and the metal impurities that segregate from the bulk.

The cleaning procedure was done in three stages: 1) The sample was annealed at 1000 °C for 10 min ($P < 1{\cdot}10^{-8}$ mbar) to remove the native oxide. 2) The temperature was decreased to 800 °C and an atomic hydrogen beam (EFM H Atomic hydrogen source, Omicron NanoTechnology GmbH, $HV = 1000$ V, $I_{emis} = 40$ mA, $I_{fil} = 1.99$ A, $P_{H_2,chamber} = 1.0{\cdot}10^{-7}$ mbar) was targeted to the sample surface for 10 min in order to remove the segregated Cu impurities. 3) The cracked hydrogen exposure was continued for another 10 min at 400 °C to remove the segregated Ni impurities. This treatment resulted in an oxide and metal free Si surface and preserved the crystalline structure.

3.1.2 Atomic layer deposition of TiO_2

All TiO_2 films studied in this work were grown by ALD. The method has been widely utilized in producing both protective and photoactive ultra-thin film coatings for electrodes used in artificial photosynthesis [10, 11, 13, 16, 21], [Papers **I**, **II**, **III**, and **IV**]. ALD is extremely suitable for this application, because the films are perfectly conformal without any shadowing effects. This is important since in many cases porous or highly topographically structured substrates are used for maximizing the active surface area [18, 19], [Papers **III**, **IV**]. The films are also relatively solid without pinhole defects, which enables the use of very thin protective or passivating layers [10, 11, 15, 54]. The thickness of the films can be modified easily and extremely precisely, and also the deposition area can be scaled up for production use. One more important aspect is the ability to control the chemical and optical properties of the film by modifying the deposition parameters, such as the deposition temperature [43, 55].

ALD is based on sequential dosing of the precursor and reactant chemicals onto the substrate. Usually this happens at an elevated temperature and with the pressure in mbar region. Unlike in many other deposition methods, such as chemical vapor deposition (CVD), the precursor and the reactant are not present simultaneously. This together with the self limiting growth of both chemicals ensures a well-controlled layer-by-layer growth mode. In this work the ALD depositions were carried out using

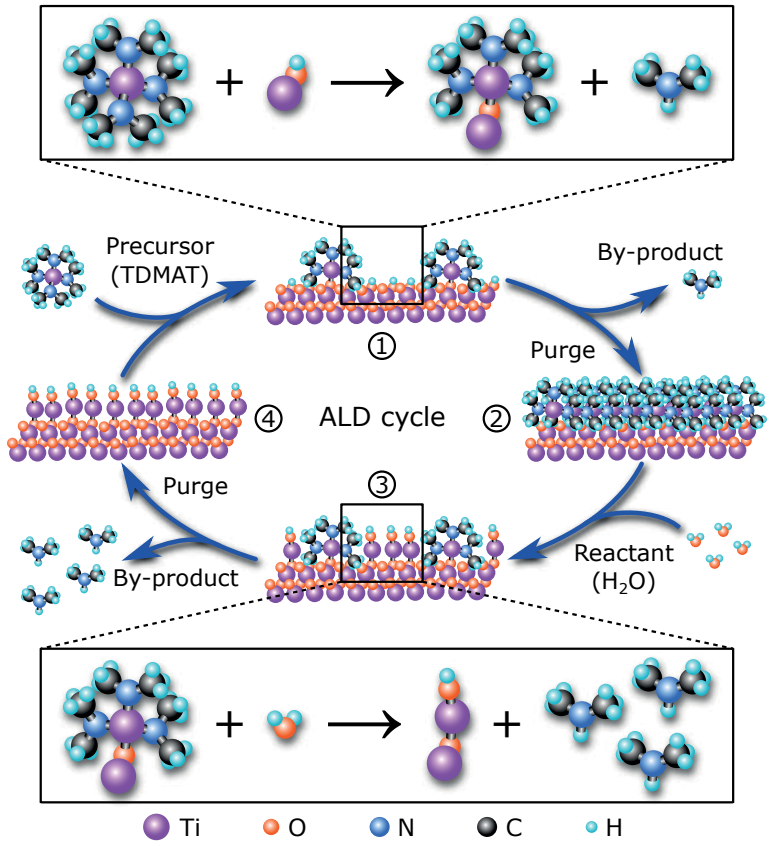

Figure 3.1: *Schematic illustration of an ALD cycle. In step 1 the TDMAT precursor reacts with the solid substrate surface. In step 2 the by-products are purged with N_2 or Ar gas and the surface is covered by a monolayer of $-\mathrm{Ti(N(CH_3)_2)_3}$ intermediate products. In step 3 the oxidizing reactant (deionized H_2O) is pulsed to surface where it dissociates the remaining dimethylamine groups. In step 4 these by-products are purged with N_2 or Ar gas and the surface is left with a new OH terminated titanium oxide layer. The boxes on the top and at the bottom show details of the chemical reaction taking place on the surface.*

Picosun Sunale ALD R200 Advanced reactor. Tetrakis(dimethylamido)titanium(IV) ($\mathrm{Ti(N(CH_3)_2)_4}$, TDMAT, 99 %, Strem Chemicals Inc., France) was used as a precursor and deionized water as reactant (oxidizer). The Si substrate temperature was kept at 200 °C during the depositions.

Figure 3.1 illustrates the propagation of an ALD cycle. In **step 1** a TDMAT pulse is introduced onto the hydroxyl group terminated surface. One of the four dimethylamine groups of the TDMAT molecule dissociates and the center Ti atom

bonds with the surface O atom according to the reaction

$$TiO_2 - OH^* + Ti(N(CH_3)_2)_4 \rightarrow TiO_2 - O - Ti(N(CH_3)_2)_3^* + NH(CH_3)_2, \quad (3.1)$$

where the asterisks denote the surface species [55]. In **step 2** the by-products (dimethylamine) and excess unreacted TDMAT are purged from the reaction chamber. Either N_2 or Ar (both 99.9999 %, Oy AGA Ab, Finland) was used as the purging gas. In **step 3** a pulse of reactant, in this case deionized water (DI-H_2O), is allowed to react with the surface. This leads to the replacement of the remaining dimethylamine groups with hydroxyl groups according to the reaction [55]

$$TiO_2 - O - Ti(N(CH_3)_2)_3^* + H_2O \rightarrow TiO_2 - TiO_2 - OH^* + 3(NH(CH_3)_2). \quad (3.2)$$

In **step 4** the by-products (dimethylamine) and excess DI-H_2O are again purged from the reaction chamber.

To obtain adequate amount of TDMAT in step 2, the vapor pressure of the TDMAT was increased to 3.6 mbar by heating the precursor bottle to 76 °C. The precursor gas delivery line was heated to 85 °C to prevent condensation. The DI-H_2O bottle was sustained at 18 °C by a Peltier element for stability control. The substrate temperature was stabilized for 30 min before starting the deposition. The following pulse timings and N_2 or Ar flow rates were used: step 1: carrier gas flow 100 sccm, 1.6 s pulse, step 2: 6.0 s purge, step 3: carrier gas flow 100 sccm, pulse: 0.1 s pulse, step 4: 6.0 s purge.

3.2 Surface analysis by photoelectron spectroscopy and spectromicroscopy

This section describes the physical principles of photoelectron spectroscopy and the general structure of the apparatus used for collecting the spectroscopic information. The spectroscopic methods have a long history dating back to the 1950's [56], and the basic principle of the measuring device has not changed drastically since then. However, the latter part of this section is dedicated to a much more novel method called photoemission electron microscopy (PEEM) or spectromicroscopy, which combines the spectral information retrieved in PES with nanometer scale lateral resolution. The PEEM part concentrates especially on a NanoESCA type instrument, which was introduced by Omicron GmbH in 2005 [57, 58].

3.2.1 Principles of photoelectron spectroscopy

Photoelectron spectroscopy relies on the photoelectric effect, where photoelectrons are emitted from a solid sample by irradiating it with UV light or X-rays [59, 60]. The kinetic energy (E_k) distribution of the emitted photoelectrons depends on the energy of the incident photons ($h\nu$) and the elemental and chemical composition of the sample. An additional amount of energy, called the work function (ϕ_s), is required to remove the photoelectron from the influence of the surface, i.e. to move it from the Fermi level to the vacuum level (E_{vac}). Thus the E_k of the photoelectrons follows the equation

$$E_k = h\nu - E_b - \phi_s, \tag{3.3}$$

where h is the Planck's constant, ν is the frequency of the electromagnetic radiation, and E_b is the binding energy of the electron. [61] In PES the E_k can be measured by the spectrometer. The Fermi levels of the sample ($E_{F,s}$) and the spectrometer ($E_{F,sp}$) are coupled electrically either to the same ground potential or through a known bias potential difference (V_{bias}). Figure 3.2 illustrates the energy levels of a photoelectron when it moves from the sample to the spectrometer.

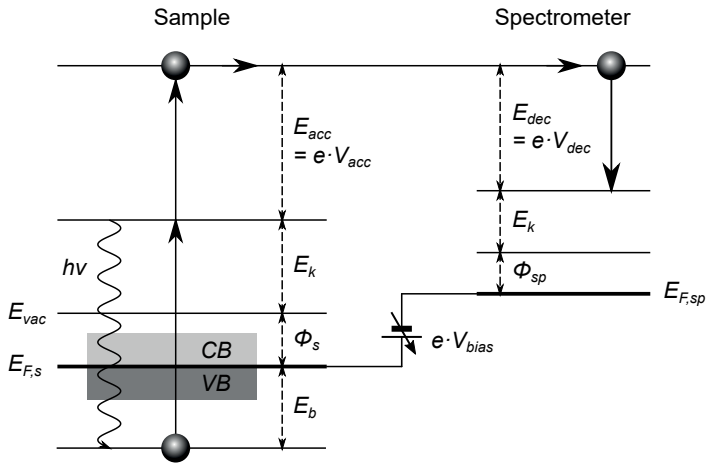

Figure 3.2: *An energy diagram of an electron when it moves from the sample to the spectrometer. Part of the photon energy ($h\nu$) is consumed for breaking the coulombic attraction (binding energy, E_b) and overcoming the sample work function (ϕ_s). The remaining energy is left as the kinetic energy of the electron (E_k). In NanoESCA system (section 3.2.4) the photoelectron is then accelerated and decelerated by electric fields (E_{acc} and E_{dec}) before entering the spectrometer energy analyzer, where the E_k inside the spectrometer can be measured.*

The accelerating and decelerating electric fields (E_{acc} and E_{dec}) are measurement specific parameters and the spectrometer work function (ϕ_{sp}) can be determined by calibration measurements. This enables the calculation of E_b without the knowledge of the sample work function just by measuring the kinetic energy of the emitted photoelectron.

Knowledge of the electron binding energies is the foundation for photoelectron spectroscopic methods, because each element has its own unique electron configuration and thus a characteristic distribution of electron binding energies. Additionally, the binding energy exhibits subtle variation as the chemical surroundings of the atom change. For example, electrons in Ti 2p core level have approximately 2 eV smaller binding energy if a Ti ion in titanium oxide is in 3+ oxidation state instead of 4+ oxidation state. Thus the elemental composition and chemical compounds of a sample can be identified by measuring the intensity (number of electrons per time unit) of the emitted electrons as a function of binding or kinetic energy. This makes electron spectroscopy extremely powerful technique for studying the chemical composition of solid surfaces, such as TiO_2 and TiSi films that are the main interest in this Thesis.

The photoemission process that generates the photoelectrons in a solid sample can be described with a three-step model that includes the photo-excitation of electrons, the transport of the electrons inside the bulk phase and the transmission of the electrons through the surface as illustrated in Figure 3.3. The three-step model is a purely phenomenological approach, but it helps to break up the photoemission process into more comprehensible subprocesses. [62] These subprocesses are described in more detail in the following sections.

3.2.1.1 Photoexcitation of electrons

The first step in the three-step model covers the penetration of the incoming photons through the surface and the interaction of the photons with the electrons. In photoelectron spectroscopic methods the photon source has to be monochromatic and have a well-defined photon energy because it is directly related to the accuracy of determining the E_b. In this Thesis the photons were produced either by a gas discharge lamp, a (monocromatized) X-ray source or a synchrotron (section 3.2.2 for details).

When the incoming beam of photons encounters the sample surface, it is refracted

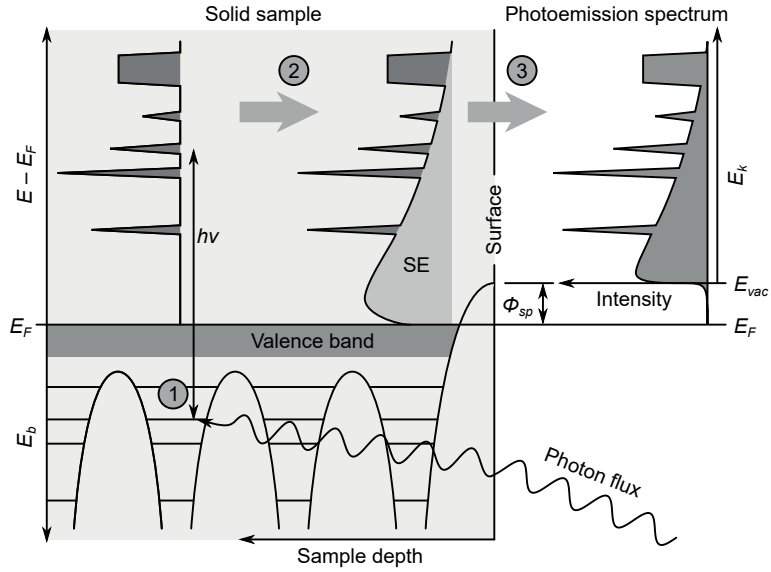

Figure 3.3: *A schematic illustration of the three-step model of photoemission process. In step one the incoming photon flux excites electrons from core levels or valence band to a higher energy state above the Fermi level. In the second step these electrons travel through the solid sample, and the interaction with other electrons generates a large quantity secondary electrons (SE) with relatively low kinetic energy. In the third step the electrons may transmit through the sample surface and form a photoemission spectrum that can be measured with electron spectroscopic methods.*

and starts to travel through the sample until the photons get absorbed, i.e. the energy is lost to electron excitations. The probability for photon absorption is described by the photoionization cross section (σ). It depends on the photon energy and the material through which the photons are propagating. [63] Figure 3.4 shows an example of photoionization cross section values for selected core levels of Ti. As can be seen, the absorption probability is highest when the photon energy is just above the electron binding energy. For this reason, the utilization of different photon sources for different measurements is vital for achieving high signal-to-noise ratio (SNR). For example, Ti 3d energy band has approximately four orders of magnitude higher photoionization cross section with He Iα radiation ($h\nu$ = 21.22 eV) compared to the cross section with Al Kα X-rays ($h\nu$ = 1486.6 eV).

In principle the photoexcitation shifts the electron to an energy level which is located the amount $h\nu$ higher in energy. However, the process may be disturbed by the formation of intrinsic satellite peaks. This means that due to the Coulombic

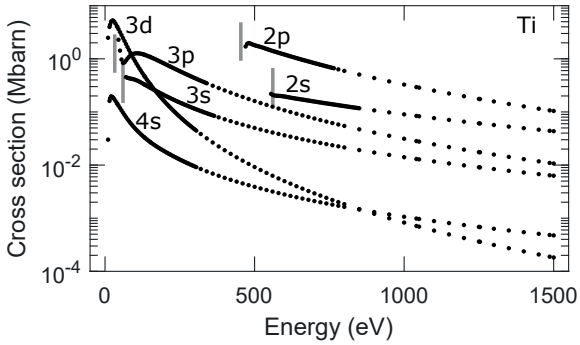

Figure 3.4: *Photoionization cross section of selected core levels of Ti as a function of photon energy. The vertical gray lines display the approximate binding energy of 2s, 2p, 3p, and 3s core levels. Data taken from [64–66].*

and exchange interactions between electrons, the emission of one electron can leave the remaining ion in an excited state. The required energy is supplied by the kinetic energy of the photoexcited electrons and therefore leads to the formation of photoelectrons that have slightly smaller kinetic energy (a few eV) than the electrons emitted from the ground state of the ion with one hole. [62] In electron spectroscopy the signal generated by these lower energy electrons is called a shake-up satellite and it forms a new peak next to the photoemission main line.

3.2.1.2 Electron transport in solids

The excited photoelectrons travel in all direction inside the solid sample and undergo interactions where they can be scattered elastically or inelastically. The most probable interaction is scattering from other electrons but also crystal defects and phonon generation cause inelastic scattering [62]. In inelastic scattering the electron loses part of its energy and does not any more contribute to the well-defined intensity at $h\nu$ eV above the original binding energy. The distribution of energy loss in a scattering process is random and non-discrete. This causes the inelastically scattered electrons to form a continuous secondary electron background which is superimposed with the sharp photoelectron peaks (Figure 3.3, step 2). The intensity of the secondary electron signal increases towards the low energy end of the spectrum because most electrons undergo several scattering processes when traveling through the solid. The mean path length that the electron travels between two inelastic scattering events is called the inelastic mean free path (IMFP).

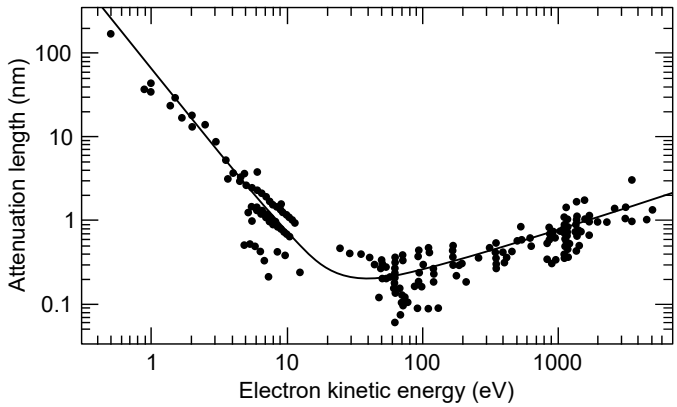

Figure 3.5: *Universal curve. Adapted from [69]*

In addition to inelastic scattering, the electrons may be scattered elastically. In this process the energy of the electron is conserved and only the direction changes. For this reason, the shortest distance between two inelastic scattering processes is typically 20–30 % shorter than the IMFP [67]. This discrepancy is taken into account in the attenuation length (AL, λ) [68].

In PES most of the useful information can be retrieved from electrons that have not scattered inelastically, i.e. they carry information about their original energy level. The number of these electrons decreases if the excitation takes place deep inside the bulk phase. The number of photoelectrons that reach the surface without inelastic scattering can be described with the Beer–Lambert equation [61, 68]:

$$I_z = I_0 e^{-z/\lambda \cos(\theta)}. \tag{3.4}$$

Here I_z is the intensity of the electron signal at the surface, I_0 is the original intensity at a depth z inside the material, λ is the attenuation length and θ is the angle at which the electrons are travelling with respect to the surface normal.

Figure 3.5 shows experimental λ values for several different elements [69]. In PES experiments the kinetic energies vary typically from 10 to 1000 eV. Thus the photoelectron signal attenuates to $1/e$ in less than 1 nm and practically all detectable signal originates from a less than ten nm thick layer. Usually the information depth is considered to be 3 λ which according to equation (3.4) covers 95 % of the total signal intensity [61, 68]. The short attenuation length of the photoelectrons inherently ensures the high surface sensitivity of the PES experiments. This makes PES

extremely suitable method for studying ultra-thin film structures, such as the TiO_2 and TiSi films studied in this Thesis.

3.2.1.3 Transmission of electrons through the surface

The final step in the three-step model for photoionization is the transmission of the photoelectrons through the sample surface. If the momentum of the electron along the surface normal is high enough, it can exit the more or less periodic potential of the bulk phase and overcome the potential barrier at the surface. Otherwise the electron will be reflected back to the sample. The cut-off energy below which the electrons can not exit the sample is defined by the sample work function. The measurement of the cut-off energy actually provides a convenient way of determining the sample work function, as will be explained in section 3.4.4. An important detail in the transmission of the electrons through the surface is that the momentum component perpendicular to the surface normal is conserved [62]. This enables the measurement reciprocal space band structure by using angle resolved photoelectron spectroscopy or NanoESCA in k-space mode. [58, 70].

3.2.2 Light sources for photoelectron spectroscopy

As mentioned in section 3.2.1.1, the energy of the incoming photon flux strongly affects the ionization probability and thus the signal intensity. The photon energy also defines the kinetic energy of the excited photoelectrons and thus determines the attenuation length. For these reasons, different measurement modes require different photon sources.

The PES measurements in Papers **I** and **IV** are conducted completely with the NanoESCA system, which affords three different photon sources: a monochromatized Al Kα X-ray source, a gas discharge ultraviolet (UV) source, and a Hg arc UV source. In Paper **III** part of the measurements are conducted in the MAX IV laboratory using a synchrotron radiation light source. In Paper **II** part of the XPS measurements were conducted in Multilab system utilizing a conventional dual anode X-ray tube based light source [71, 72].

3.2.2.1 Focused X-ray source

The NanoESCA system (section 3.2.4) includes a focused monochromatized Al Kα X-ray source (FXS) (Ulvac-Phi, Inc., model 36-100). The focusing improves the photon flux on the sample surface, which is extremely desirable for PEEM measurements with a small analysis area and a relatively weak photoelectron signal. Additionally, the monochromator enables much higher energy resolution compared to conventional X-ray tubes, which improves the identification of overlapping peaks from different chemical states. The focusing is realized by generating the primary electron beam with a focused LaB_6 based electron gun instead of using a more conventional filament with a large emission area. The well-defined electron beam is targeted to an Al anode and the characteristic Al Kα X-rays are diffracted to the sample via an ellipsoidal quartz(100) crystal monochromator. The electron beam size on the anode can be adjusted approximately from 5 to 100 µm, and the resulting X-ray spot size on the sample has roughly the same are due to the symmetric Rowland circle geometry. The monochromator filters the Bremsstrahlung and additional characteristic lines from the spectrum allowing only K$\alpha_{1,2}$ to pass to the sample. After monochromatization the X-ray energy is 1486.5 eV and X-ray line FWHM 0.26 eV. [73]

3.2.2.2 Gas discharge He Iα UV source

The VB measurements in Papers **I**, **II**, **III**, and **IV** were done by using He Iα radiation ($h\nu$ = 21.2188 eV) as the excitation source. The low energy improves the photoionization cross section of the valence electrons for several orders of magnitude compared to Al Kα induced measurements. The radiation was produced with a VUV Source HIS 13 (Omicron Nanotechnology) which is based on cold cathode capillary discharge. The source has a He gas filled insulating tube. When high potential difference (typically 500–700 V during the normal operation) is applied along the tube, the electric field results in a break through and continuous discharge. The characteristic UV light (in this case mostly He Iα) is generated when the ionized atoms relax to their ground state. The light is introduced to the sample through a two-stage differential pumping capillary and focused with a gold coated toroidal mirror. [74]

3.2.2.3 Hg arc UV source

The Hg arc UV source is mainly aimed for lens alignment during spectromicroscopic measurements. The device consists of a HBO 103W/2 type lamp, which produces a typical Hg discharge spectrum. The integrated heat filter separates most of the visible and infrared (IR) spectrum letting only the main UV line at 4.9 eV (wavelength 248 nm) to be transmitted to the sample. The combination of the low energy and high intensity produces a very strong (secondary) electron yield, which can be used for tuning the lens settings of the energy analyzer. However, the excitation energy is not adequate for actual measurements. [75]

3.2.2.4 Synchrotron radiation

Synchrotron radiation is the most versatile excitation source for several electron spectroscopic methods due to its extreme brightness (or brilliance) and adjustability. A synchrotron consists of a storage ring where electrons travel at high energies, typically several GeV and close to the speed of light. In modern synchrotron facilities the radiation is usually produced by insertion devices, such as undulators, where the periodic magnetic field compels the electrons to sine-wave-like trajectories. The radial acceleration of the electrons results in the emission of very intense electromagnetic radiation. Compared to traditional laboratory based X-ray sources the brightness (i.e. intensity) of the synchrotron radiation is several orders of magnitude greater [76]. An additional benefit of synchrotron radiation is that the wavelength can be tuned. This enables, for example, the optimization of the photoionization cross section and the variation of the information depth in electron spectroscopic measurements.

The synchrotron radiation generated by the undulator in the storage ring is utilized at the beamlines. These usually consist of a monochromator, mirrors, slits, and the experimental station(s). The structure of the I311 beamline [77] of the MAX II storage ring at the MAX IV Laboratory is illustrated in Figure 3.6. The spectroscopic low energy electron microscopy (SPELEEM, Elmitec Elektronenmikroskopie GmbH) endstation was used to obtain the PEEM results presented in Paper **III**.

In PEEM measurements the information volume corresponding to each image pixel is extremely small. With laboratory based PEEM systems, such as NanoESCA,

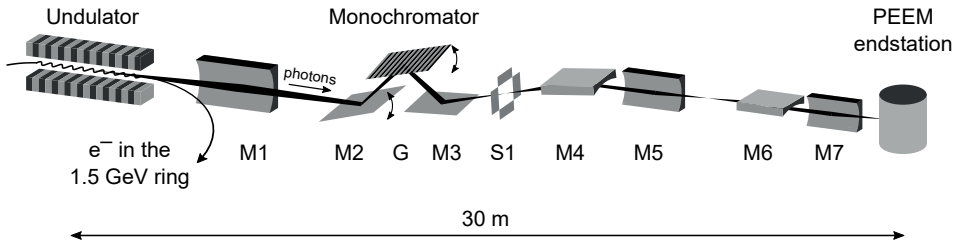

Figure 3.6: *Schematic layout of the I311 beamline. The beamline consists of an undulator, horizontally focusing pre-mirror (M1), rotating plane mirror (M2), plane grating (G), spherical focusing mirror (M3), exit slit (S1), spherical re-focusing mirrors (M4–M7) and PEEM endstation at the end of the beamline. An additional PES endstation is located between the mirrors M5 and M6, but it was not utilized in this work. [77]*

this requires larger acceptance angles and longer exposure times, which reduces the spatial resolution. The high brightness of synchrotron radiation enables more accurate electron detection setups in terms of both spatial and energy resolution without compromising the signal-to-noise ratio or the duration of the data collection. Additionally, the line width of the radiation itself can be adjusted to optimize the overall energy resolution. This facilitated, for example, to distinguish the TiSi and elemental Si compounds in the Si 2p core level images in Paper **III**.

The easily tunable photon energy enables synchrotron radiation to be used for X-ray absorption spectroscopy (XAS). In this technique, the electron emission current is measured as a function of photon energy. As the photon energy exceeds the absorption edge of an element in the sample, the core electrons can be excited to the unoccupied electronic states leading to a sharp increase in the X-ray absorption coefficient. Information about electronic structure, i.e. the elemental and chemical composition of the sample, can be deduced by analyzing the shape of the absorption curve in the vicinity the absorption edge. XAS can easily be combined with a PEEM lens system for electron yield measurement. This way XAS can be used for measuring localized electronic properties in the sample, as shown in Paper **III**. Also, the information depth of XAS can be tuned by measuring the photoelectron current in the total or partial yield mode. The first one leads to a larger information depth due to the long IMFP of the low energy secondary electrons, whereas the latter (usually measured from an Auger transition) has a shorter IMFP and thus smaller information depth.

3.2.3 Electron detection in photoelectron spectroscopy

In addition to a photon flux with high intensity and well-defined energy, PES requires a method for detecting the emitted photoelectrons. This is typically realized with an electron spectrometer that consists of an electrostatic lens system, a hemispherical electron energy analyzer (HSA) and an electron detector (Figure 3.7). The lens system collects the photoelectrons emitted from the sample within a predefined solid angle. The lens system also applies the necessary accelerating and decelerating electric fields as explained in Figure 3.2. After the lens system the electrons are injected to the energy analyzer where a radial electric field (E) generated between two hemispheres (radiuses R_1 and R_2) deviates the electrons to circular trajectories. Depending on the strength of the electric field only electrons with a certain kinetic energy called the pass energy (E_p) can travel through the gap between the hemispheres and escape the analyzer through the exit slit. Electrons with too low or too high kinetic energies will collide with the inner or outer hemispheres, respectively. Finally, an electron detector, typically a channeltron multiplier, calculates the number of electrons and converts it to a digital signal. The multiplication is based on a cascade effect, where the successive collisions with the channeltron walls produce a large measurable flux of secondary electrons. [78] The spectroscopic information can be collected by scanning the accelerating or decelerating electric fields inside

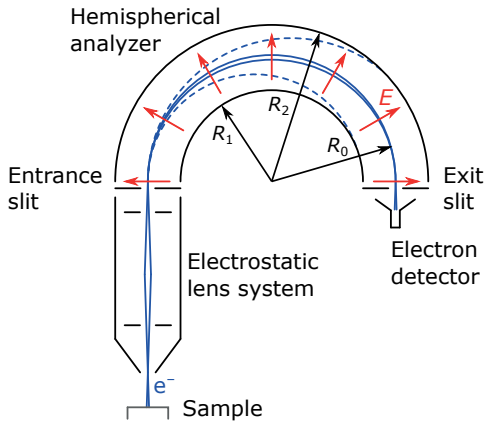

Figure 3.7: *Schematic structure of a typical electron energy analyzer. Electrons emitted from the sample travel through the electrostatic lens system and the entrance slit to the hemispherical analyzer, where the radial electric field E bends them to circular trajectories. If the kinetic energy of an electron equals the analyzer pass energy, the trajectory will have a radius R_0 and the electron can pass the exit slit and be collected by the electron detector. Electrons with lower or higher kinetic energy will be absorbed by the analyzer surfaces.*

the lens system and varying the electric potential of the hemispheres. This way the spectrometer can be used to record the number of photoelectrons as a function of kinetic energy.

In purely spectroscopic (as opposed to imaging) systems the electron detection area defined by the lens system is relatively large, usually tens or hundreds of micrometers. This improves the data collection efficiency and SNR but leads to a poor spatial resolution and averaging of data over a large area. This is not a problem for laterally homogeneous samples such as ALD grown TiO_2 films, but for spatially varying surfaces, such as the TiSi structures in Papers **III** and **IV**, more sophisticated spatially resolving spectromicroscopic methods are needed.

3.2.4 Photoemission electron microscopy

Photoemission electron microscopy or spectromicroscopy can be considered as an extension to the conventional photoemission electron spectroscopy. The main idea is to provide lateral resolution while preserving the high spectroscopic energy resolution. This requires the electron intensity data to be acquired in three dimensions: two lateral dimensions and the energy dimension. Traditionally the two lateral dimensions have been accomplished by scanning either the position of the photon source, the detection area of the electron energy analyzer or the sample position [57, 58, 79, 80]. All these methods require a two-dimensional point-by-point scanning procedure which makes the data collection process slow. Additionally, the method based on the movement of the photon source necessitates a tightly confined photon flux, which is difficult to implement with sub-micrometer resolution.

More developed spectromicroscopy designs utilize parallel imaging where scanning is executed only in one lateral dimension in conjunction with a line detector. Another advanced option is the so-called full field of view parallel imaging, where each spot within the analysis area is studied simultaneously. This method is utilized, e.g., in the NanoESCA spectromicroscopy system manufactured by Scienta Omicron GmbH [81], and the system has been used in all Papers included in this Thesis.

NanoESCA is a novel multitechnique surface analytic system, which combines a PEEM lens system with an aberration corrected imaging energy analyzer and several different excitation sources. In a typical configuration the excitation can be produced by a Hg arc UV source ($h\nu = 4.9$ eV), gas discharge He Iα UV source ($h\nu =$

21.22 eV) or monochromatized Al Kα X-ray source ($h\nu$ = 1486.5 eV). The most distinct feature in NanoESCA is, however, the variety of measuring modes. The same system can be utilized for non-energy-filtered PEEM, conventional XPS with various detection areas and energy-filtered PEEM (EF-PEEM), i.e. spectromicroscopy. This variety is made possible by the imaging double energy analyzer (IDEA), where two hemispherical analyzer are connected in a tandem arrangement (Figure 3.8) [57]. In the PEEM mode, the photoelectron signal is collected directly through the PEEM column without passing it through any energy filtering. The electron detection is carried out in parallel using a 2D micro channel plate (MCD) and a CCD camera.

The high lateral resolution (down to 30 nm) of the NanoESCA is based on a low energy electron microscopy (LEEM) lens system, originally developed by Ernst Bauer and Wolfgang Telieps [83–85]. Lens column has an an immersion objective lens, which means that the sample is part of the objective electrode configuration. Under normal operation the sample surface and the stationary part of the lens have a 12 kV potential difference across an approximately 1.8 mm wide vacuum gap. This generates a 6.7 MV/m electric field, which directs the emitted photoelectrons to parabolic trajectories towards the lens system. After the objective lens, the PEEM column has and exchangeable and adjustable contrast aperture in the dispersive plane for limiting spherical and chromatic aberration, an electrostatic octupole stigmator for correcting small misalignments in the optical axis.After the stigmator the electrons travel through two projection lenses which are used for selecting the detection mode, and a deflector which directs the electron beam through the entrance slit of the energy analyzer. [82] In PEEM mode the hemispherical energy analyzer is turned off and the projection lenses focus the electron flux directly to an MCP and a fluorescent screen. In this mode the image is formed mostly by secondary electrons, and due to the high intensity this mode can be used, for example, for locating the points of interest on the sample surface and also for aligning the lens system. [57]

For XPS mode the first hemisphere is switched on and the projection lenses are adjusted to adapt the electron flux to the pass energy of the analyzer. In this mode the analyzer operation closely resembles that of a conventional hemispherical energy analyzer explained in section 3.2.3, and the system can be used for recording typical XPS or UPS spectra. An advantage compared to normal XPS equipment is that the field of view (FoV) can be first located in PEEM mode and the size can be easily adjusted from micrometers up to several hundred micrometers.

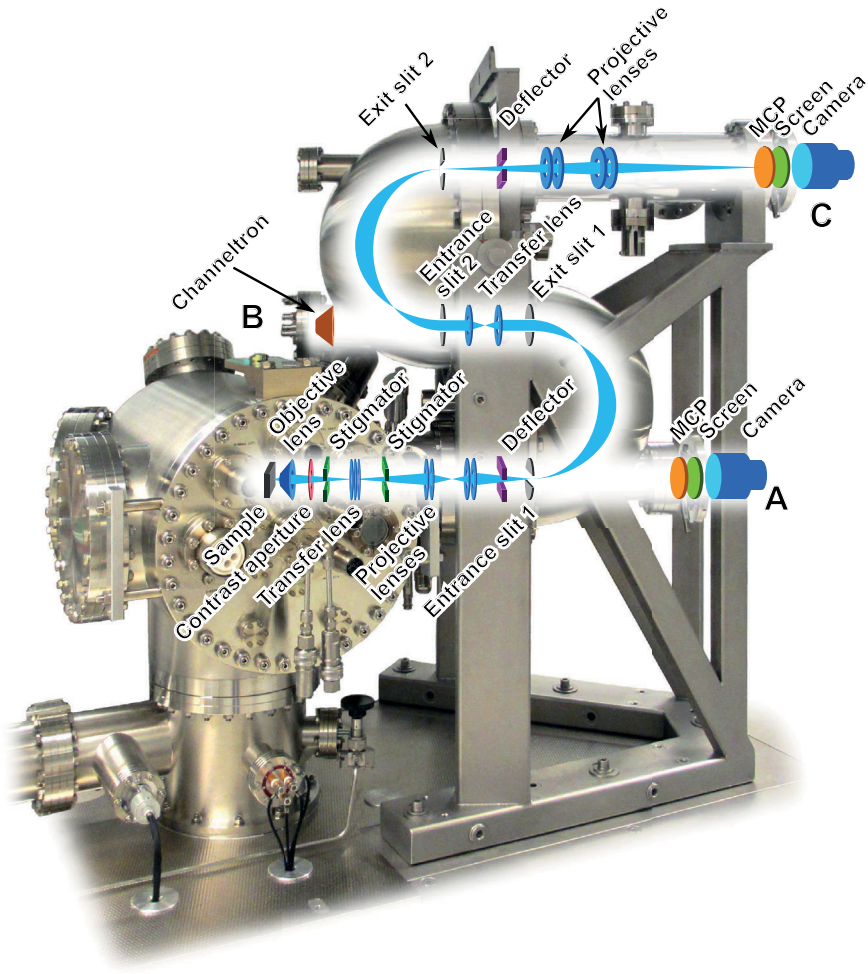

Figure 3.8: *NanoESCA electron optics. The photoelectron signal can be measured in three different operating modes: non-energy-filtered PEEM (detector A), conventional XPS (detector B) and EF-PEEM (detector C). [57, 82]*

The most significant advantage of the NanoESCA system is the parallel imaging EF-PEEM mode, where both hemispheres of the IDEA are utilized. In imaging systems with a single hemisphere the spatial resolution is often limited by the so called α^2 aberration (analyzer spherical aberration) [57, 58], where α is the entrance angle of electrons with respect to the optical axis at the analyzer entrance slit (Figure 3.9(a)). Due to this aberration electrons with the same energy but different entrance

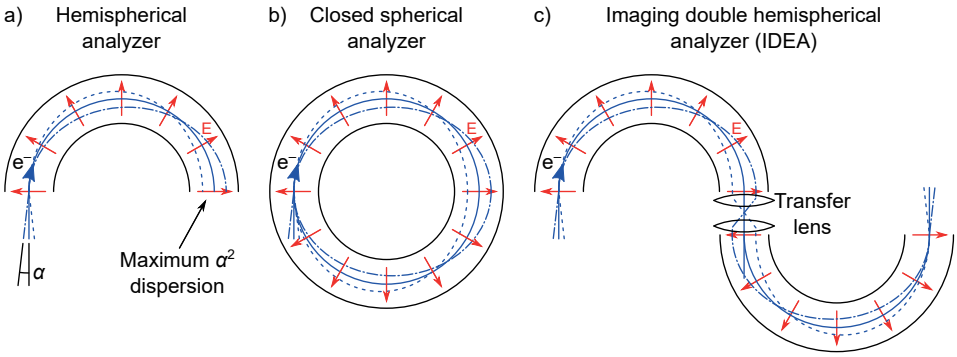

Figure 3.9: *Schematic illustration of hemispherical energy analyzer constructions. (a) A normal single HSA induces a strong α^2 aberration at the exit point, which blurs the image. (b) A closed spherical analyzer cancels out the aberration but is not feasible for electron transport in an out of the analyzer. (c) Mirroring the second hemisphere enables electron insertion and collection while maintaining the aberration free trajectories at the exit point. Modified from [57, 82]*

angles have trajectories with varying eccentricities. The aberration is strongest after π rad revolution (i.e. after passing one hemisphere) but completely cancels out after a full 2π rad revolution (Figure 3.9(b)). For a feasible realization of transporting the electrons in and out of a full revolution analyzer, the IDEA has one hemisphere mirrored to the opposite side and a transfer lens added between the hemispheres. This way the radial electric field in the second hemisphere cancels out the α^2 distortion caused by the first hemisphere (Figure 3.9(c)).

3.3 Analysis of spectroscopic data

A PES measurement is usually started by recording a wide energy range survey spectrum, e.g. covering binding energies from 0 to 1200 eV. All elements contribute at least one photoemission line within this energy range. The objective of the survey scan is to identify the elements present on the surface. For this reason, the intensity and SNR are optimized at the cost of energy resolution by using a large FoV, high E_p and a wide analyzer entrance slit. Figure 3.10 illustrates an example of a survey spectrum measured on a reduced TiO_2 surface, where Ti, O, and also C related spectral features are visible.

In addition to photoemission peaks the survey spectrum depicts Auger electron peaks, indicated with labels LMM and KLL in Figure 3.10. These spectral features

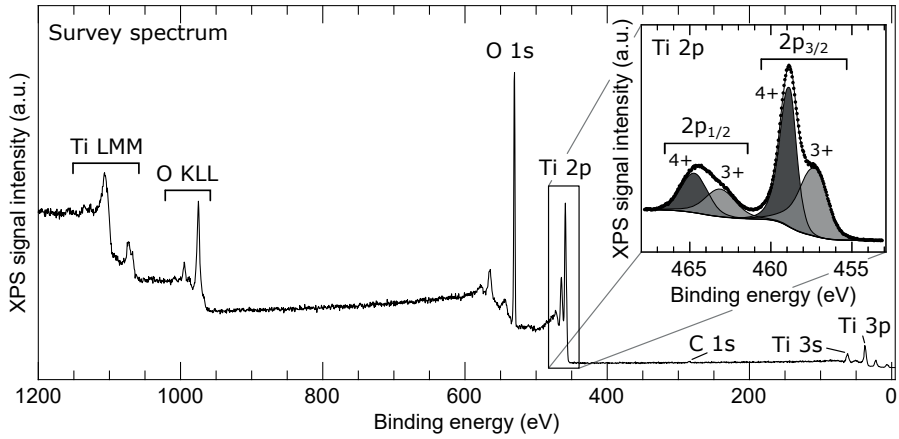

Figure 3.10: *An XPS survey spectrum of an ALD grown TiO_2 surface after a 400 °C annealing in ultra-high vacuum (UHV). The inset shows a detail spectrum of Ti 2p with synthetic components fitted for 4+ and 3+ oxidation states. The spectra are measured using NanoESCA in XPS mode.*

are formed when a photoelectron escapes from the material and another electron fills the hole in the core level. The energy released in this relaxation process may be transferred to a third electron, which is then emitted from the material. These electrons are called Auger electrons, and the labeling is based on the core levels in which the hole is located during the Auger process. [86, 87]

Typically the most intensive non-overlapping photoelectron peak for each element is selected for a detail spectrum measurement, e.g. Ti 2p transition in the inset in Figure 3.10. The detail spectrum is measured with energy resolution optimized settings (small E_p and narrow analyzer slit) for identifying the exact binding energy and line shape of the transition. The binding energy of the electrons in an atom exhibits small variation caused by the initial and final state effects, which take place before and after the photoexcitation process, respectively [62, 88].

The initial states describes the ground state energy of an atom just before the photoexcitation process. This initial state may be affected by changes in the chemical environment, such as oxidation, which introduces a core level shift (CLS) in the observed photoemission lines or binding energies. For example, in the case of TiO_2 the Ti atom has lower electronegativity than O. Thus the loss of valence electrons induces an effective positive charge to the Ti atom, which then increases the binding energies of the remaining electrons. For Ti this shift can be up to about 5.5 eV

(the difference between Ti^0 and Ti^{4+} oxidation states). Additionally, the chemical environment of the surface atoms differs from that of the bulk atoms, which induces an additional surface core level shift (SCLS). This effect is however much weaker than the CLS, and can usually be observed only with extremely surface sensitive synchrotron radiation based PES measurements [89].

Final state effects are phenomena that affect the photoelectron energy after the photoexcitation process. Most notably the remaining electrons of the ionized atom and also the electrons in the surrounding atoms undergo relaxation (atomic and extra-atomic relaxations), which reduces the total energy of the system. Thus the emitted but not yet completely decoupled photoelectron may acquire more kinetic energy than what could be assumed based on the original energy level configuration. [61, 88]. On the other hand, the escaping photoelectron may excite some of the remaining valence electrons into higher energy states. This leads to reduced kinetic energy, which is observed as shake-up satellite peaks located a few electron volts higher in binding energy than the main photoemission line [88]. Similarly, the photoelectron may excite oscillations in other electrons, which leads to plasmon loss peaks [61, 90].

The magnitude of the final state effects on the kinetic energy of the photoelectron depends on the studied system. The two extreme models for the effect are the sudden approximation and the adiabatic approximation. In the sudden approximation the photoelectron is assumed to exit the system so rapidly that the relaxation processes do not affect the kinetic energy. On the other hand, in the adiabatic approximation the system is expected to reach an equilibrium state before the electron exits the system. In reality the situation is somewhere between these two extremes. The sudden approximation is most accurate when the emitted photoelectron has a high kinetic energy and the studied material is a metal or other good conductor. In this case, the interaction time is short and the freely moving valence electrons can effectively screen the core hole. In insulators and other poor conductors, and especially with low kinetic energies, the relaxation processes are much more influential thus leading to strong satellite features. [88, 91, 92]

The measured photoelectron spectrum is a superposition of photoemission lines (affected by the initial and final state effects), Auger electron lines and the background formed by the inelastically scattered electrons. In order to isolate the significant information from the spectrum the data is usually deconvoluted into components

as shown in the inset in Figure 3.10. The inelastic background is subtracted by fitting a Shirley or linear type background and the remaining peak area is filled with synthetic components, often Gaussian or Lorentzian distribution functions, corresponding to different chemical states. The intensity, i.e. the area of the component, I, is proportional to the number of atoms in that specific chemical environment within the analysis volume. However, the probability of an electrons in a specific transition contributing to the measured spectrum depends on ionization cross section of the electron σ, the attenuation length λ, and the transmission function of the energy analyzer T_E. These factors can be combined in the relative sensitivity factor S, which can be determined either experimentally or from literature for each transition and element. Thus the relative concentration of an element x can be expressed as

$$c_x = \frac{n_x}{\sum n_i} = \frac{I_x/S_x}{\sum I_n/S_n}, \tag{3.5}$$

where n_x is the amount of substance x in the analysis volume [90].

3.4 Analysis of spectromicroscopic image data

The analysis method described above has typically been applied to large area (FoV from hundreds of micrometers to millimeters) photoelectron spectroscopy, but the same principles can be utilized for obtaining extremely localized (tens of nanometers) information from spectromicroscopic measurements. This section demonstrates the basic image analysis methods together with the data correction and filtering procedures used in this Thesis.

3.4.1 Deduction of spectroscopic data from image sequences

In NanoESCA the spectromicroscopic measurements are carried out in full field parallel imaging mode, i.e. the energy axis is scanned during the measurement. This produces a stack of individual images files, each corresponding to a specific electron binding energy. The result can be considered as a 3-dimensional intensity matrix $I(x, y, E)$, where each voxel represents the intensity of the photoelectron signal at a specific location (x_i, y_j) on the sample surface at binding energy E_b.

The spectroscopic data can be deduced from the image files by slicing the stacks along the energy axis. This results in a set of normal PES spectra, where each

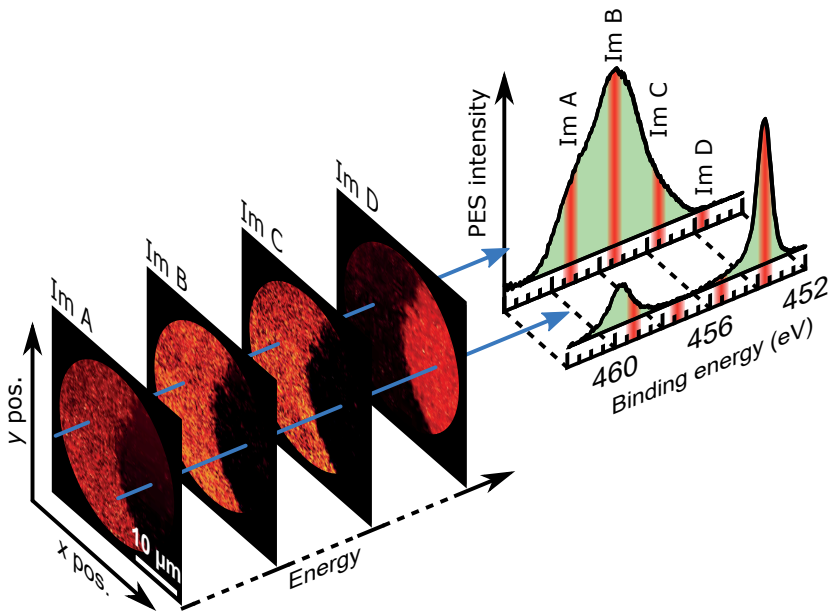

Figure 3.11: *Schematic illustration of how the spectral information is deduced from a raw spectromicroscopic image stack. The intensity of each pixel in each image corresponds to the PES signal intensity at that specific energy and position.*

spectrum represents a specific location on the sample surface, as illustrated in Figure 3.11. In NanoESCA the image size is fixed to 600 × 600 px^2, thus resulting in 360 000 individual spectra. The effective size of one pixel on the sample surface can be scaled by adjusting the FoV, although the electron optics of the system limit the ultimate lateral resolution to approximately 30 nm.

3.4.2 Image data corrections and filtering

The MCP and CCD camera based analogue image detector superimposes the measured image data with instrument dependent artifacts. Removal on these disturbances requires post-filtering of the acquired data. Below is a list of the most typical NanoESCA related artifacts that were corrected during the data analysis.

Camera dark field correction: Due to the weak photoelectron signal in core level EF-PEEM, the CCD camera exposure time has to be long, even several minutes. This significantly strengthens the small variations in the dark field current of the different CCD channels, and leads to the appearance of individual bright pixels that

do not correspond to the true photoelectron signal. The problem can be corrected by recording a dark field image (i.e. an image without any photoelectron signal) with the same exposure time and subtracting this data from each measured image.

Outlier filtering: In addition to the dark field current differences between the channels, the CCD camera also has varying noise. This superimposes the real data with randomly scattered very bright or dark pixels. To mitigate this artifact the images were run through an outlier filter. Values above or below preset threshold values were replaced by the average brightness value around that pixel.

Temporal CCD fluctuation filtering: The overall sensitivity of the CCD camera varies in the time scale of tens of seconds. For this reason, images in an energy scan have varying brightness levels which does not correspond to the true photoelectron signal intensity. As opposed to the two previous localized artifacts, this disturbance changes the whole image collectively. Thus the fluctuation can be filtered by setting the average brightness of the dark corners outside the screen area to zero for each image in the stack.

Flat field correction: The sensitivity of the detector is not constant across the field of view. This is caused by the hexagonal net structure in the MCP, dust particles between the screen and the camera, changes in the MCP multiplication efficiency etc. One way to correct these variations is to measure a flat field image from a homogeneous part of the sample and to divide all experimental data with this flat field signal [93]. In this work, however, all EF-PEEM intensity data is shown as relative atomic concentrations. This inherently corrects for the flat field fluctuations, because the concentration calculation includes a division operation as shown in equation (3.5).

Non-isochromaticity of the images

Despite the α^2 aberration correction the IDEA introduces significant non-isochromaticity in the image data [94]. This means that the data points in different parts of the image represents different energy values. The largest variation appears along the energy dispersive axis of the analyzer (y-axis in Figure 3.12). The variation depends on the microscope setting, such as the pass energy and the entrance slit width, and varies from tens of meV to more than one eV. In this work the error introduced by the non-isochromaticity has been corrected by measuring a work function map from a homogeneous flat reference surface using the same settings as for the actual

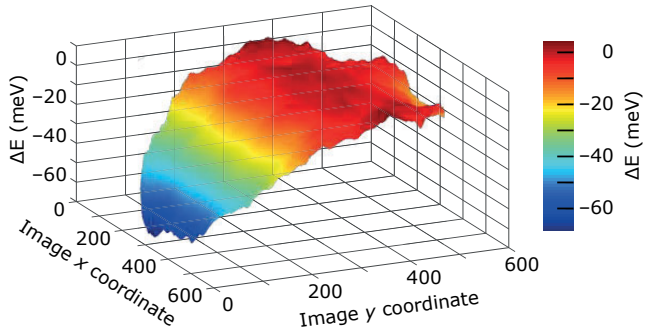

Figure 3.12: *Non-isochromaticity effect induced by the IDEA. The surface plot illustrates the microscope dependent artifact where the work function map of a homogeneous flat Si(100) surface shows large parabolic energy dispersion along the y axis.*

studied sample. An example of such flat reference is illustrated in figure 3.12. Each voxel line along the energy axis (constant x and y) in the image stack is then corrected by shifting the energy values based on the reference measurement. The non-isochromaticity error resembles a parabola in the dispersive y direction with the vertex having the "correct" non-dispersed energy value [93].

3.4.3 Principal component analysis of image data

Due to relatively weak excitation sources and low ionization probabilities the spectromicroscopy data often has low signal-to-noise ratio. In addition to increasing the data acquisition time, the SNR can be improved by applying statistical multivariate analysis techniques, such as principal component analysis (PCA), to the data sets. In this Thesis the method was utilized for the core-level image stacks, and the analysis was carried out using the built-in analysis functions in the CasaXPS software [95]. The original multidimensional data was decomposed into orthogonal abstract factors using singular value decomposition. Then the most significant abstract factors, i.e. those corresponding to the largest singular values and thus representing the most relevant data and least noise were used to generate a new set of data with improved SNR. [96, 97]

3.4.4 Determination of the local work function

The energy-filtered imaging energy analyzer combined with a He Iα UV source enables convenient measurement of local variations in the sample work function ϕ_s

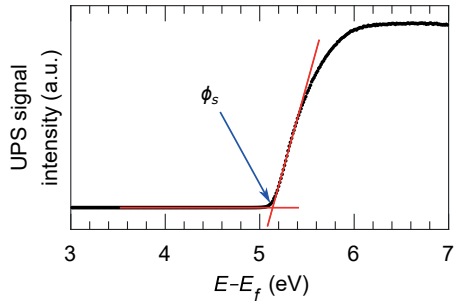

Figure 3.13: *The secondary electron cut-off edge of an annealed TiO_2 film. The red lines indicate the linear fits to the slope and the level background. The work function ϕ_s was interpreted as the intersection of these two lines.*

with a lateral resolution better than 200 nm [98, 99]. Additionally, in NanoESCA the energy scanning is performed by adjusting the sample bias voltage while the spectrometer is kept at a constant potential. This automatically distinguishes the sample and spectrometer secondary cut-off edges without the need for an external bias voltage [100, 101].

The work function determination was performed by making linear fits to the secondary electron cut-off edge and the background on the low kinetic energy side of the edge. The work function was interpreted as the intersection of these two linear fittings as illustrated in Figure 3.13. In spectromicroscopic measurements the fitting had to be performed for all (x,y) pairs in the image stack. A Matlab script was written to automate the fitting procedure.

In NanoESCA a high extraction voltage is applied between the sample and the PEEM entrance lens. This generates a Schottky effect, which lowers the work function according to the equation

$$\Delta\phi_s = -e\left(\frac{e\mathbf{E}}{4\pi\epsilon_0}\right)^{1/2}, \tag{3.6}$$

where ϵ_0 is the vacuum permittivity ($\epsilon_0 = 8.854188 \cdot 10^{-12}$ F m^{-1}). [102, 103] In NanoESCA the electric field is typically 12 kV across a 1.8 mm gap, which results in a ϕ_s lowering of 0.098 eV. This was taken into account in the reported ϕ_s values.

3.5 Photoelectrochemical measurements

The prospective applications of the studied materials are in optimizing the electronic structure and chemical stability and activity of photoanode surfaces in artificial photosynthesis. Thus the applicability tests included different electrochemical measurements, such as cyclic voltammetry (CV) and electrochemical impedance spectroscopy (EIS), combined with simulated solar irradiation.

The electrochemical measurements were performed in a custom-made three-electrode cell shown in Figure 3.14. The studied sample was connected as the working electrode (WE), while an Ag/AgCl electrode (Leak-Free LF-2, Warner Instruments, LLC) and a Pt wire were used as reference (RE) and counter electrodes (CE), respectively. The cell was controlled by a Autolab PGSTAT12 potentiostat/galvanostat (Metrohm AG) and the simulated solar irradiation was produced by a HAL-C100 solar simulator (Asahi Spectra Co., Ltd., JIS Class A at 400–1100 nm with an AM1.5G filter), and the intensity was adjusted to 1.00 Sun using a 1 sun checker (model CS-30, Asahi Spectra Co., Ltd.). An aqueous solution of 1 M NaOH was used as the electrolyte in all electrochemical measurements.

In Papers **I**, **II**, and **IV** the electrochemical experiments consisted mainly from linear scan voltammetry and chopped light constant potential amperometry measurements. In linear voltammetry the sample potential is scanned across a potential range, usually from the photocurrent onset potential up to approximately 2 V against the reversible hydrogen electrode (RHE), where the photoelectrochemical water oxidation is overrun by other oxidation phenomena. The measurements were carried out both in dark and under simulated solar light. Low dark currents are beneficial for

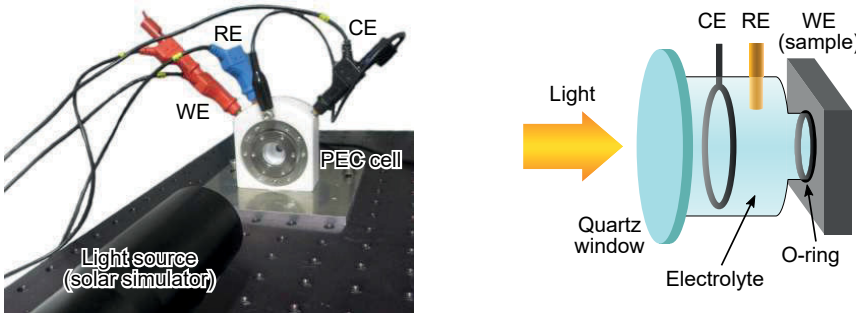

Figure 3.14: *The three-electrode cell used for the PEC measurements. The schematic illustration on the right shows the electrode locations.*

the electrode material because they are an indication of low recombination rates and thus low losses. On the other hand, the light current needs to be maximized for effective water splitting. Some of the samples were also tested for long term stability by biasing them to constant potential for several hours under simulated operating conditions.

In Paper **IV** the samples were subjected also to EIS measurements. EIS is a powerful tool for investigating the dielectric and transport properties of materials [104]. The EIS results were analyzed by fitting electrical equivalent circuits (EEC), where resistor-capacitor pairs connected in series presented the different layers of the $TiO_2/TiSi_2/Si$ layer structure. The method unveils knowledge about the electronic properties of the buried layers and interfaces inside the sample.

4 EFFECT OF POST-TREATMENT METHODS ON TiO_2/Si PHOTOANODES

This chapter presents the experimental results included in the four Papers that comprise the core of this Thesis. TiO_2 has been extensively studied for artificial photosynthesis applications since the 1970's [6], but modern research methods can still reveal new perspectives on this material. Especially the variety of growth methods, such as ALD and several liquid chemistry based techniques combined with post-treatment procedures, such as thermal treatments or reductive gas exposures, have brought renewed interest in the subject.

The first section of this chapter focuses on the thermal post-treatments of ALD grown TiO_2 and their implications on the chemical stability and charge transfer properties of the photoelectrodes. Special attention is paid to the versatility of the so-called black TiO_2, which can be grown by ALD and where the amorphicity and oxygen deficiency provide interesting post-modification prospects. The second section presents a more radical post-modification method, where TiO_2 is converted into TiSi under reductive high temperature conditions. The resulting microstructured TiSi surface can be utilized as an intermediate layer between two semiconductors for tailoring their band alignment and charge transfer properties.

4.1 Thermal post-treatments of black TiO_2

TiO_2 is generally considered to be a chemically stable material for both photoactive photoanodes and for protecting other unstable small band gap semiconductor anodes [10,11,105]. However, the results in Papers **I** and **II** indicate, that this is not true for ALD grown amorphous TiO_2 if water splitting is performed under alkaline conditions (1 M NaOH, pH = 13.6). As Figure 4.1 illustrates, the as-deposited 28.7 nm thick TiO_2 film becomes completely dissolved in less than 5 hours whereas a thermally post-treated sample shows prolonged stable operation.

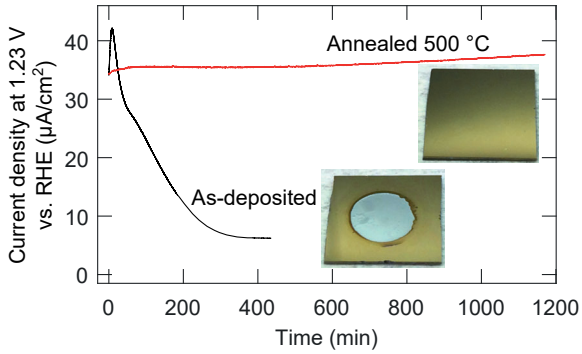

Figure 4.1: *The photocurrent density of two TiO_2/Si photoanodes during a long stability test under continuous simulated solar irradiation in 1 M NaOH. The black curve shows rapid degradation for the as-deposited ALD TiO_2 film while the red curve proves stable photocurrent for a film that has been post-annealed at 500 °C in vacuum. The images clearly indicate the dissolution of the as-deposited TiO_2 film. Adapted from Paper* ***I****.*

4.1.1 Reductive post-annealing for improved stability

In this work the effects of reductive post-treatment of ALD grown TiO_2 films were studied by comparing two different reduction methods: low pressure atomic H based chemical reduction and thermal annealing in ultra-high vacuum (UHV) [Paper **I**]. The studied 28.7 nm thick amorphous TiO_2 films were ALD grown on cleaned Si(100) substrates and the UHV annealings were performed at a temperature range from 400 to 900 °C. The thermal post-treatment led to the formation of TiO_x suboxide species with $x < 2$. Depending on the temperature, the concentration of the Ti^{2+} and Ti^{3+} species was up to 80 % of all titanium atoms. The amount of reduced titanium was unexpectedly high, as many studies have concentrated on only couple of percent of reduced Ti ions. The propensity for strong reduction was attributed to the amorphicity and intrinsic oxygen deficiency of the 200 °C deposited TiO_2. Stoichiometric crystalline TiO_2 is considerably less reducible, and even the ALD grown TiO_2 film with 100 °C deposition temperature showed less defects and thus less proficiency for reduction as illustrated in Figure 4.2.

The reference post-treatment method in Paper **I**, the atomic H exposure, was carried out by using the same H_2 cracker as described in section 3.1.1. This resulted in a very similar mixture of original Ti^{4+} and reduced Ti^{2+} and Ti^{3+} species as the thermal treatment, although the formation of Ti^{2+} was delayed with H treatment. The most interesting result was, however, that despite the similarities in Ti reduction, the concentration and chemical state of the O anions was completely different depending

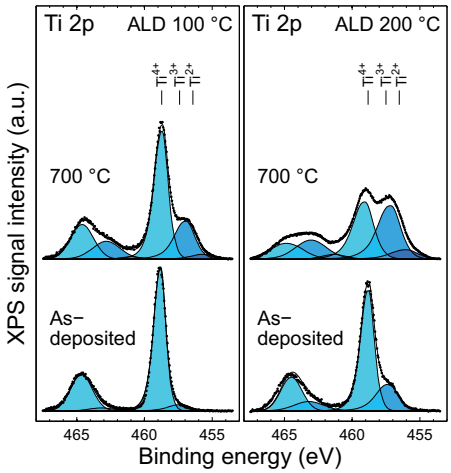

Figure 4.2: *Comparison of Ti 2p XPS spectra measured on TiO_2 films deposited at 100 °C (left) and 200 °C (right). The 100 °C film is close to stoichiometric TiO_2 composition (only Ti^{4+} oxidation state), whereas the 200 °C film shows approximately 20 % suboxide Ti concentration. This difference is reflected to the reduction behavior, as the 700 °C UHV annealing has much stronger effect on film with the higher deposition temperature and higher initial oxygen deficiency.*

on the post-treatment method, as illustrated in Figure 4.3. For example, 800 °C annealing and 10 min H exposure both reduce approximately 67 % of the Ti ions on the surface. However, in the H exposure the O atoms are removed from the structure and the oxygen concentration drops from the original 70 % to 55 %. On the other hand, the thermal reduction maintains the original oxygen concentration, and a new chemical state, labeled as O^-, is developed on the high binding energy side of the original O^{2-} peak. Photoelectrochemical stability tests under simulated solar irradiation showed that the thermally reduced (at 500 °C or above) TiO_2 is stable against photocorrosion, whereas the H treated and as-deposited films dissolved. X-ray diffraction (XRD) was employed to verify that both treatments preserved the amorphous structure. Thus the improved stability was attributed to the formation of undercoordinated O^- centers, which can act as charge transfer channels and thus stabilize the surrounding matrix. Similar results have been found for amorphous IrO_2, which structurally resembles TiO_2 and can also be used as a photocatalyst in water splitting reactions [106–108]. The thermally induced stability demonstrates that with a suitable post-treatment amorphous "leaky" TiO_2 can be successfully applied as a protective ultra-thin film on top of other semiconductor photoelectrodes or used as a photoactive anode material.

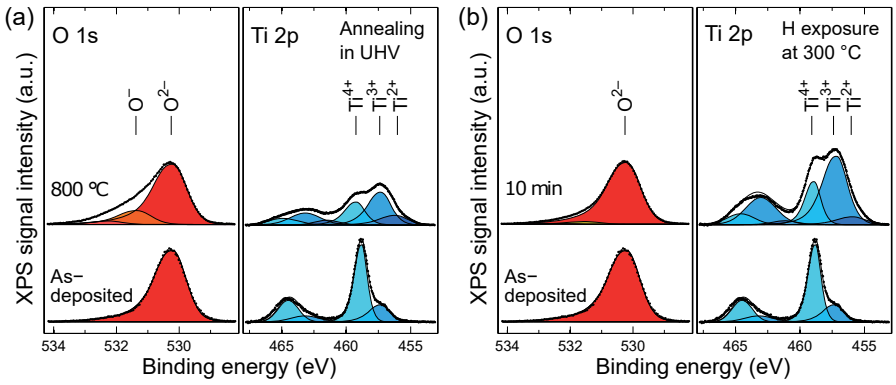

Figure 4.3: *Comparison of selected XP spectra from thermally and atomic H post-treated TiO_2 films. Adapted from Paper* ***I****.*

Additionally, both thermal and atomic H post-treatments generate new electronic states inside the band gap. The shallow states narrow the effective band gap thus increasing the solar absorption towards longer wavelengths. Similar results are typically achieved by doping the TiO_2 matrix with e.g. N, C, or S [24–26]. The reductive post-treatments offer a complementary method for band gap engineering without the need for introducing additional elements to the matrix.

4.1.2 Crystallization of amorphous black TiO_2

Contrary to the previous reducing thermal UHV and atomic H treatments, the stability of TiO_2 can be improved also by annealing it in oxidizing conditions. As shown in Paper **II**, annealing in air at 300 °C or above leads to photocorrosion resistant crystalline TiO_2. The studied samples were prepared with the same ALD parameters as the ones used for the reductive post-treatments. However, this time the annealing was carried out in a tube furnace in ambient atmosphere. As illustrated in Figure 4.4 the grazing incidence X-ray diffraction (GIXRD) patterns clearly show a transformation TiO_2 from amorphous phase into rutile at temperatures 300 °C and above. Based on the SEM images (Figure 3 in Paper **II**) the nucleation of crystals starts already at 250 °C. As a detail, at 350 °C annealing temperature the GIXRD shows a strong anatase peak, which then disappears at all higher annealing temperatures. The appearance of this additional phase coincides with the surface segregation of residual N, which is trapped in the film from the incompletely dissociated TDMAT precursor. This implies that N plays an important role in the phase stabilization of

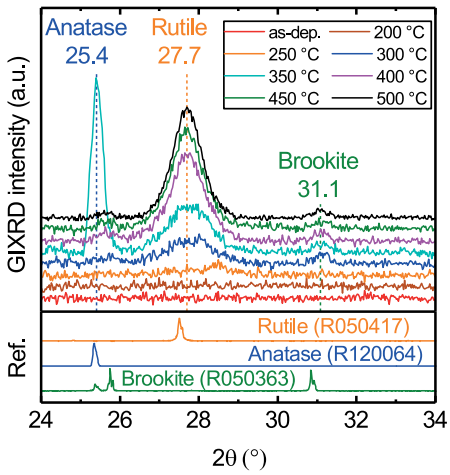

Figure 4.4: *GIXRD patterns of the oxidatively annealed TiO_2 surfaces with reference data. Annealing at 300 °C or above leads to formation of rutile phase. Interestingly, at 350 °C also a strong anatase peak is observed, but it disappears again at higher annealing temperatures. [Paper* ***II****]*

TiO_2. As the residual N desorbs from the surface at 400 °C, TiO_2 crystallization proceeds from the less stable anatase into the more stable rutile phase.

The oxidation and crystallization of the TiO_2 films leads to drastic decrease in conductance and optical absorption of visible light with a simultaneous redshift in the optical band gap, as illustrated in Figure 4.5. Photoelectrochemical results

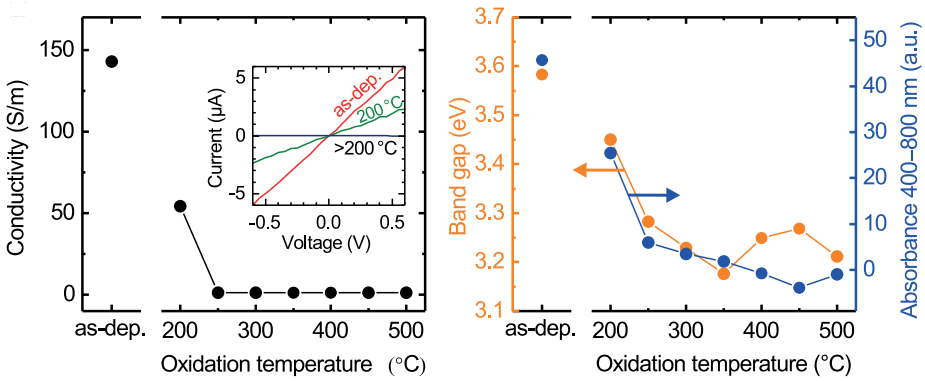

Figure 4.5: *Conductivity, optical band gap and absorbance at the 400–800 nm wavelength range for ALD grown TiO_2 films after the deposition at 200 °C and after annealing in ambient atmosphere at 200–500 °C. [Paper* ***II****]*

under simulated solar irradiation in Paper **II** show, that oxidative annealing induced crystallization also improves the photocurrent density. This can, at least partially, be explained by the red-shifted optical band gap, which increases the light absorption within the UV region. Together the chemical stability, decreased absorption of visible light and increased absorption of UV light make oxidatively annealed TiO_2 an excellent material to be used, for example, in tandem or Z-scheme water splitting cells (section 2.3) [35], where the absorption band needs to be well-defined and the outermost layer has to be stable when in contact with an electrolyte.

4.2 From TiO_2 to TiSi interlayers

In Paper **I** the reductive annealing of TiO_2 in UHV was studied at temperatures up to 900 °C. This led to a partial reduction and formation of different suboxide species (Ti oxidation number < 4). However, if the annealing temperature is increased to 950 °C or above, the oxide becomes thermodynamically unstable. This leads to a complete reduction followed by the formation of a new TiSi phase where the Ti is mixed with the Si of the underlying substrate.

4.2.1 Islanded growth of TiSi structures

TiSi structures have widely been used in nano- and microelectronics as ohmic contacts and also as interconnect materials for PEC devices. Thus, understanding the transformation of ALD deposited TiO_2 ultra-thin films into TiSi may provide cost-effective and realizable method for fabricating these structures as an integral part of sequential ALD growths.

The formation of TiSi was studied by ALD-growing a 28.7 nm thick TiO_2 film on top of an atomic H cleaned (section 3.1.1) Si(100) substrate. The sample was then annealed at 950 °C in UHV for 10 min. This led to the structure illustrated in Figure 4.6. The conversion of TiO_2 into TiSi is initiated by the formation of nucleation centers across the original TiO_2 film. The nucleation centers then expand to somewhat spherical regions of microstructured TiSi islands, as shown in Figure 4.6. Based on the AFM results in Paper **III**, the TiSi structure is highly corrugated: the conversion of a 28.7 nm thick TiO_2 film into TiSi leads to a topographical variation of over 300 nm. Thus the reduction of Ti and consequent intermixing with the Si substrate involves pronounced mass transfer.

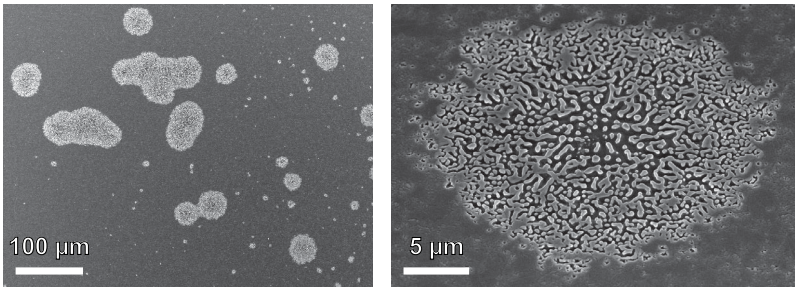

Figure 4.6: *SEM images of the microstructured TiSi regions. On the left the dark area represents the remaining TiO_x film and the brighter areas consists of the topographically microstructured TiSi islands. The image on the right shows a magnified view of one of the TiSi regions.*

The expansion mechanism of the TiSi regions was studied by collecting EF-PEEM data across the TiO_2/TiSi boundary (Figure 4.7). Based on the core level images of Ti 2p, Si 2p, O 1s, the TiSi region is completely oxygen free, whereas the regions far outside the islands consist of a mixture of TiO_x species with Ti atoms in different oxidation states. An interesting detail in the line profile in Figure 4.7(b) is that the TiSi region is surrounded by an approximately 4 µm wide rim of high Ti^{2+} concentration. This indicates that the expansion of the TiSi regions proceeds via a TiO intermediate. Another interesting detail is that no Si diffusion was observed through the remaining TiO_x film outside the TiSi regions. This is in contrast to studies performed on metallic Ti/Si surface, where the Si diffusion is observed already at 400–800 °C [109–111].

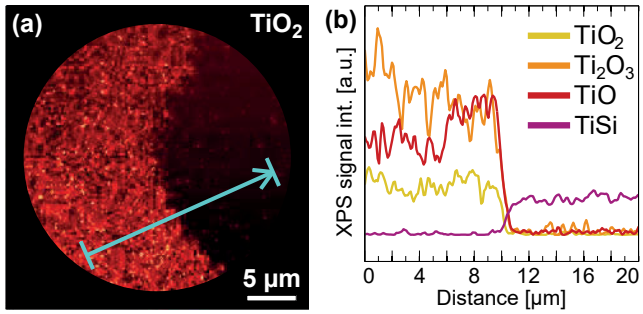

Figure 4.7: *EF-PEEM data of a TiSi/TiO_x boundary. (a) An EF-PEEM image of Ti^{4+} $2p_{3/2}$ core level. The bright red "crescent" on the left side corresponds to high concentration of oxidized Ti whereas the area on the right has very low intensity due to completely reduced Ti. (b) line profiles of different Ti oxidation states taken from the position indicated by the blue arrow in (a). Adapted from Paper **III**.*

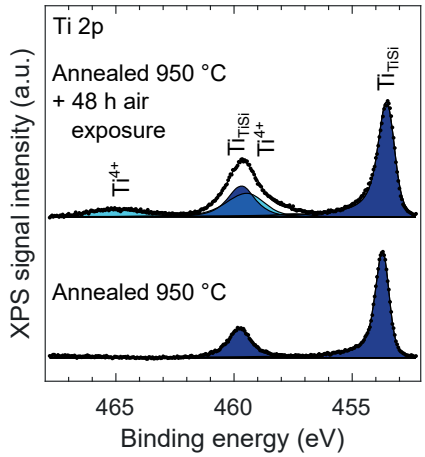

Figure 4.8: *Ti 2p XP spectra of a TiSi surface immediately after annealing at 950 °C in UHV and after 48 h air exposure. Most of the Ti is preserved in reduced TiSi form.*

Inside the reduced regions, Si was detected in two different chemical states which were identified as pure elemental Si and Ti bonded Si in silicide (denoted as Si^0 and Si_{TiSi}, respectively). The lateral resolution of the laboratory X-ray source based NanoESCA is limited to approximately 500 nm for core level images. For this reason, the more detailed structure of the TiSi regions was studied by synchrotron radiation induced PEEM (SR-PEEM). The results (see Figure 4 in Paper **III**) illustrate, that the Ti and Si_{TiSi} are almost entirely detected inside the high-lying ridges (brighter areas in Figure 4.6), whereas the valleys between the ridges contain mostly pure Si and only a small amount of Ti.

The stability of TiSi against oxidation was tested by exposing the reduced surface to ambient air for 48 hours. Pure Ti is extremely reactive against air, but in silicide form only a small fraction of Ti was oxidized back to Ti^{4+} species (Figure 4.8). This is beneficial when TiSi is used as a photoelectrode interface material that should retain its metal-like conductivity during the fabrication process.

4.2.2 Band alignment and charge transfer in TiO_2/TiSi/Si photoanodes

The feasibility of TiSi as a photoanode intermediate layer was studied in Paper **IV** by measuring the energy band alignment and charge transfer properties of different TiO_2/TiSi/Si structures. Efficient solar irradiation induced water splitting

requires that the electrode energy bands straddle the water reduction and oxidation potentials. Additionally, adequate band bending is required for effective electron–hole pair separation and all layers must have sufficient conductivity for supporting the required charge transfer. In Paper **IV** a TiSi interlayer was applied between a Si(100) substrate and approximately 30 nm thick TiO_2 overlayer. The microstructured TiSi film was fabricated by the same process as described above. The effect of such interlayer has previously been studied by e.g. Perego et al. [112] who have conducted comparable experiments for TiO_2/X/Si systems, where the interlayer X has been either Si_3N_4, Ti rich SiO_x, or Al_2O_3. They found that proper selection of interlayer material can affect the band alignment across the TiO_2–Si interface. In this work research was conducted on three different TiSi interlayers. Although the material was the same in all cases, the microstructure of the film was modified by altering the thickness of the original TiO_2 film which was then converted into TiSi by UHV annealing. The studied film thicknesses were 3 nm, 10 nm, and 30 nm.

As illustrated in Figure 4.9, the thickness of the TiO_2 greatly affects the TiSi microstructure. The 3 nm and 10 nm TiO_2 films lead to unconnected islands, where the size distribution correlates with the film thickness. The 3 nm film produces islands with diameter variation approximately from 10 to 100 nm, whereas the 10 nm thick film leads to much bigger islands with a diameter from 50 to 500 nm. An interesting change happens between the 10 and 30 nm TiO_2 film thicknesses, as the thicker film results in the coalescence of the TiSi islands and thus in the formation of a continuous conductive TiSi network.

The effect of the TiSi micro-structure on the photoelectrochemical properties was studied by measuring linear sweep voltammetry under simulated solar illumination and electrochemical impedance spectroscopy (EIS). Based on the voltammetry results, the samples with TiSi films generated from the 3 and 10 nm TiO_2 films expressed approximately 0.1 V more negative photocurrent onset potential compared to the samples without TiSi or with a TiSi interlayer fabricated from the 30 nm TiO_2 film. Additionally, the EIS results proved, that the TiSi interlayer decreases the resistance across the heterojunction thus improving the charge transfer properties of the TiO_2/TiSi/Si photoanode.

In order to understand why the TiSi interlayer affects the onset potential and charge transfer properties of the three-layer photoanode system, a complete band energy diagram was reconstructed. Figure 4.10 shows the band positions of VBM, CBM,

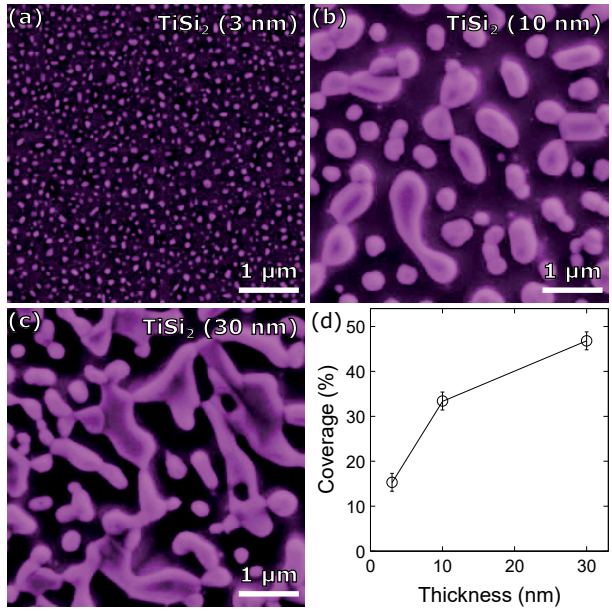

Figure 4.9: *SEM images of TiSi/Si surfaces. The TiSi films have been fabricated from 3, 10 and 30 nm thick TiO_2 ALD films (images (a), (b), and (c), respectively. Figure (d) illustrates the TiSi island coverage in all three situation. [Paper **IV**]*

E_{vac} and selected core levels for each intermediate deposition step and all three different TiSi film thicknesses. Most notably, the 3 nm and 10 nm TiSi structures increase the band bending of the underlying Si substrate by about 0.1 eV leading to a total upward bending of 0.34 eV. On the other hand, the 30 nm TiSi interlayer leads to a band bending close to that of pure Si surface. Similar differences in band bending were preserved even after the deposition of a 3 nm thick TiO_2 overlayer.

Based on the band alignment reconstruction and the electrochemical measurements, Z-scheme model for charge carrier transport was proposed. Here the TiSi islands at the heterojunction interface act as recombination centers and high conductivity charge transfer channels. Increased band bending leads to more effective charge carrier separation, where the photogenerated holes from the Si and the photogenerated electrons from the TiO_2 overlayer are transferred effectively towards the TiSi interface.

Figure 4.10 shows also the WF values of the samples based on an average value over the whole analysis area (95 µm). However, the imaging capabilities of NanoESCA

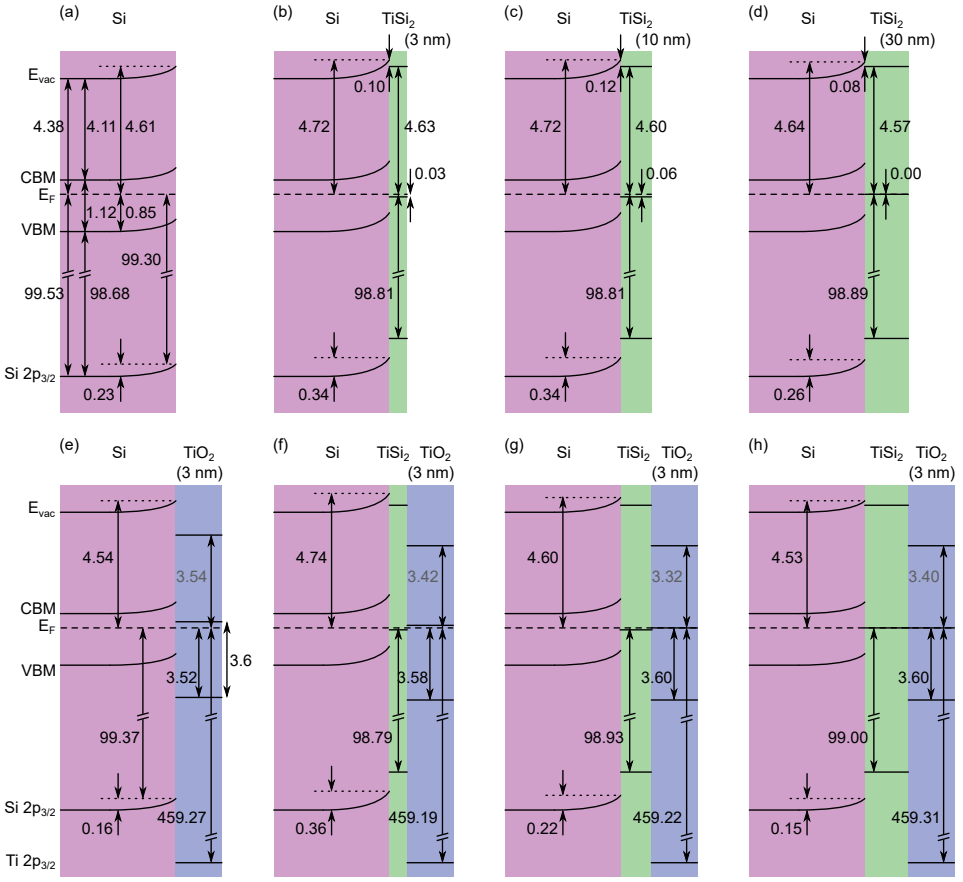

Figure 4.10: *Band energy diagram of clean Si (a), titanium silicide coated Si with different TiSi interlayers (3, 10, and 30 nm) (b–d), and TiO_2/TiSi/Si heterojunction systems where 3 nm of TiO_2 has been deposited on top of the structure (e–h). [Paper **IV**]*

enabled the collection of WF data also with a lateral resolution of approximately 100 nm. These WF maps are shown in Figure 4.11. For pure Si and 3 nm and 10 nm TiSi surfaces the WF values are homogeneous across the surface. However, the TiSi film fabricated from the 30 nm thick TiO_2 layer shows considerable dispersion between the TiSi regions (highest WF) and the intervening Si areas (lowest WF). The homogeneity of WF values for the small TiSi islands can be explained by the "pinch-off" effect [113] where the barrier variation of sufficiently small island features becomes pinched off by the surrounding semiconductor regions. Similar results have been observed on Ni island/n-Si systems [114, 115]. With small Ni islands the effective barrier height drifts closer to that of the surrounding semiconductor surface.

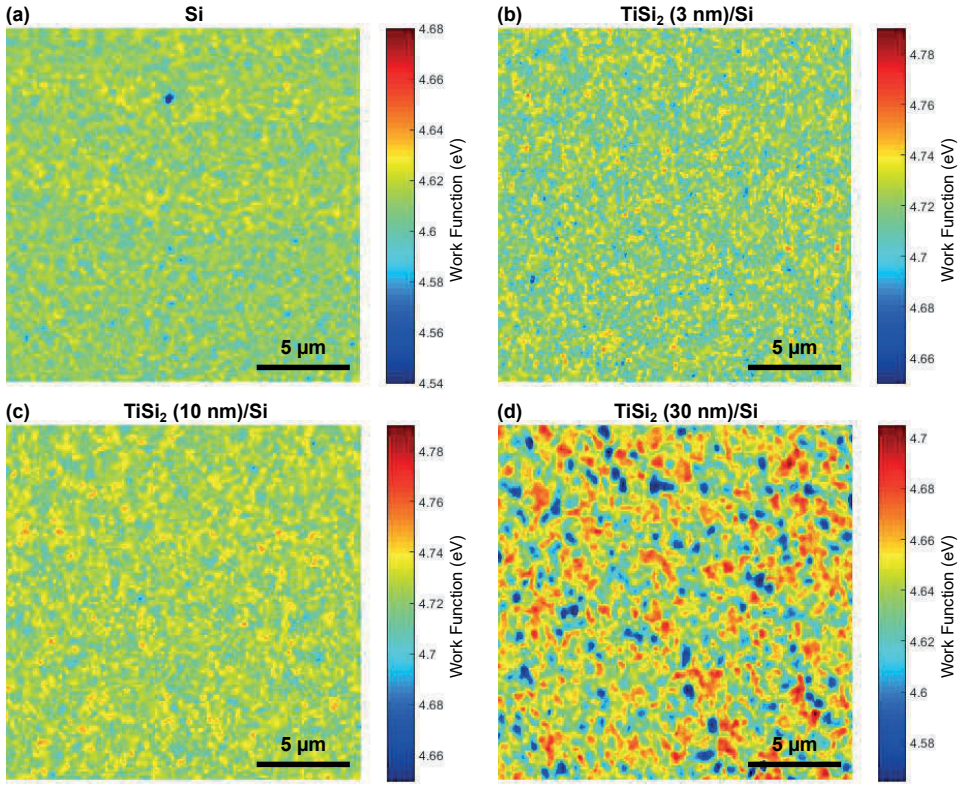

Figure 4.11: *Work function (WF) maps of TiSi coated Si with different TiSi interlayers (3, 10, and 30 nm). [Paper **IV** Supplementary information]*

However, as the islands become larger, the band bending inside the islands behaves more independently and the barrier height moves closer to the barrier height of a continuous metallized surface.

As a summary, thermally fabricated TiSi microstructure can be used as an interfacial layer between an ALD grown TiO_2 film and Si substrate for improving the efficiency of photoanodes used in water splitting. The primary material, TiO_2, for TiSi fabrication can conveniently be produced as an integral part of the ALD deposition chain, and the properties of the thermally fabricated TiSi microstructure can be modified by varying the original TiO_2 film thickness. With suitable island size the TiSi interlayer leads to increased band bending in the Si substrate, and thus improved charge carrier separation and more negative photocurrent onset potential.

5 CONCLUSIONS AND OUTLOOK

Atomic layer deposited TiO_2 is a promising material for electrodes used in photoelectrochemical water splitting due to its abundancy, cost-effectiveness, conformality and easily controllable film thickness. However, the chemical stability under alkaline conditions, large band gap corresponding to the UV region of the solar spectrum and charge carrier separation and charge transfer properties require further optimization. In this Thesis a combination of electron spectroscopic and spectromicroscopic techniques together with photoelectrochemical and optical measurements was used to study how different post-treatments and interface layers affect the properties of an ALD TiO_2 coated photoanode.

The results of this Thesis clearly indicate that suitable reductive and oxidative post-treatments can improve the chemical stability of the TiO_2 ultra-thin films in alkaline electrolytes. In order to understand the effect of the reductive treatments on the TiO_2 film in detail two different reduction methods were utilized: thermal reduction in UHV at 400–900 °C and chemically active reduction using atomic hydrogen. Both methods resulted in seemingly similar Ti suboxide formation and preserved the amorphous structure. However, only the vacuum annealed surface was chemically stable in 1 M NaOH under simulated solar illumination. Additionally, the O/Ti ratio was kept practically constant in the annealed samples despite the strong reduction of Ti. Based on the XPS results, oxygen was shifted to a more oxidized O^- state. In the H treated samples the O concentration was significantly decreased and all remaining O was preserved in the O^{2-} state. The increased chemical stability of the annealed films was thus attributed to the O^- ions, which are essentially defects in the anionic network. Similar formation of O^- ions has been detected by Pfeifer et al. in amorphous IrO_2 based photoelectrode coatings [106–108]. Also in their study these reactive defect centers improved the water splitting capabilities.

The other method for improving the chemical stability of the TiO_2 films was annealing in oxidative conditions. Post-annealing in ambient air at 300–500 °C transformed

the film into crystalline rutile structure, or at 350 °C to a mixture of rutile and anatase. The original as-deposited film consisted of so-called black TiO_2, which has attracted a lot of research interest [20, 116–118] since its discovery by Chen et al. in 2011 [119]. As the name suggests, the film appears visually black, and the material has noticeable absorption at the visible range of the solar spectrum. During crystallization the film became white and the absorption above 400 nm (3.1 eV) dropped to practically zero. The crystallization also induced a redshift in the optical band gap from 3.6 eV to 3.1–3.2 eV. As a result of crystallization, the resistivity was increased and the electronically "leaky" [10, 13] amorphous TiO_2 was transformed into an insulator. However, the crystalline structure significantly improved the chemical stability and also the photocatalytic efficiency, thus making the oxidatively annealed ultra-thin TiO_2 film a viable option for coating other small band gap semiconductor photoelectrodes.

The interface between the outer TiO_2 film and the inner semiconducting electrode material always produces losses in charge transfer. The effect of a TiSi interlayer was studied as a possible solution for mitigating this problem. The TiSi layers were prepared by increasing the UHV annealing temperature above the oxide decomposition temperature of approximately 950 °C. Based on the results, O is removed from the structure and Ti mixes with the underlying Si substrate generating highly topographically microstructured TiSi islands. The phenomenon has been previously studied with metallic Ti/Si systems by, e.g., Nemanich et al. [120–123]. In these studies, the Ti layer thickness was typically varied from submonolayers to couple of nanometers, which led to the formation of much smaller islands and much less pronounced mass transfer. The intermixing was observed also by Arranz and Palacio, but without any thermal processing the TiSi formation was limited to a few monolayers thick uniform TiSi film at the Ti/Si [124] or Si/Ti [125] interface. Based on the SR-PEEM results in this Thesis, the high-lying micro-islands are composed of a mixture of Ti and Si, whereas the low-lying valleys mostly consist of Si. SR-PEEM in XAS mode however revealed that there is some Ti left in the valleys, which is a divergent result from those published by Nemanich et al. [120].

The effect of the TiSi interfacial layer on the charge transfer and PEC properties was studied in detail by fabricating TiO_2/TiSi/Si photoanodes with varying TiSi structures. The thicknesses of the original TiO_2 films used for TiSi formation were 3, 10 and 30 nm. The study revealed that the TiSi island size correlates with the thickness of the TiO_2 layer. In addition, the PEC properties were affected, and the 3

and 10 nm films led to most negative photocurrent onset potentials thus improving the photoanode efficiency. The improvement was attributed to the increased band bending the TiSi structure induced in the Si(100) substrate. The reconstruction of the band energy diagram indicated that the charge transfer across the TiO_2/TiSi/Si heterojunction follows a Z-scheme model, where the TiSi islands act as recombination centers. The TiSi islands may also provide a low resistance charge transfer channel between the insulating SiO_x regions, as TiSi was found to be resilient against oxidation.

All PEC measurements in this Thesis were carried out on photoanodes where the ALD grown TiO_2 film formed a contact with the aqueous electrolyte. TiO_2 is known to have some degree of photocatalytic activity [126], and for example the oxidative post-treatment clearly improved the catalytic properties. However, commercially feasible energy conversion necessitates current densities of the order of several mA/cm^2. Driving the OER or HER reactions at such rate is probably not possible on pure TiO_2 surface, but requires additional catalyst materials at the photoelectrode–electrolyte interface. Typical catalyst materials are, for example, RuO_x [17, 32, 127], IrO_x [11, 17, 106, 107], CoO_x [54, 128, 129], and NiO_x [16, 21, 130–132]. Many of these can be grown by ALD, and could thus be easily incorporated in the TiO_2 based photoelectrodes in the forthcoming studies. Another common photocurrent improvement method aside the catalysts is to increase the reactive surface area by generating nanostructures, such as nanorods or nanonets, on the surface [19, 127, 133–135]. Due to the extreme conformality of ALD grown films, these nanostructures would form an interesting template for depositing additional TiO_2 or catalyst films for improving the photoelectrochemical efficiency.

An additional direction for the upcoming research would be to integrate the results of this Thesis into complete artificial photosynthesis, where the water splitting reaction is combined with CO_2 reduction. The overall process leads to the generation of oxygen gas and hydrocarbons using only solar light as an external energy source. Current fossil fuel based power plants could be attractive point sources for CO_2 [4]. Converting these emissions into solar fuel would help to solve both the solar energy storage challenges and the problem of the rapidly increasing CO_2 concentration in the atmosphere.

REFERENCES

[1] International Energy Agency, *World Energy Balances 2018*. IEA Publications, 2018, available: https://www.oecd-ilibrary.org/energy/world-energy-balances_25186442, cited 3.9.2019.

[2] "BP Statistical Review of World Energy 2019," 2019, 68th edition, data compilation: Centre for Energy Economics Research and Policy, Heriot-Watt University, available: https://www.bp.com/en/global/corporate/energy-economics/statistical-review-of-world-energy.html, cited 3.9.2019.

[3] R. Lindsey, "Climate change: atmospheric carbon dioxide," *National Oceanographic and Atmospheric Administration, News & Features*, 2018.

[4] R. Van de Krol and M. Grätzel, *Photoelectrochemical hydrogen production*. Springer, 2012, vol. 90.

[5] M. R. Allen, O. P. Dube, W. Solecki, F. Aragón-Durand, W. Cramer, S. Humphreys, M. Kainuma, J. Kala, N. Mahowald, Y. Mulugetta, R. Perez, M. Wairiu, and K. Zickfeld, "Framing and context," in *Global Warming of 1.5 °C. An IPCC Special Report on the impacts of global warming of 1.5 °C above pre-industrial levels and related global greenhouse gas emission pathways, in the context of strengthening the global response to the threat of climate change, sustainable development, and efforts to eradicate poverty*, P. Z. V. Masson-Delmotte, H.-O. Pörtner, D. Roberts, J. Skea, P. R. Shukla, A. Pirani, W. Moufouma-Okia, C. Péan, R. Pidcock, S. Connors, J. B. R. Matthews, Y. Chen, X. Zhou, M. I. Gomis, E. Lonnoy, T. Maycock, M. Tignor, and T. Waterfield, Eds., 2018, in Press.

[6] A. Fujishima and K. Honda, "Electrochemical photolysis of water at a semiconductor electrode," *Nature*, vol. 238, p. 37, 1972.

[7] R. Sathre, C. D. Scown, W. R. Morrow, J. C. Stevens, I. D. Sharp, J. W. Ager, K. Walczak, F. A. Houle, and J. B. Greenblatt, "Life-cycle net energy assessment of large-scale hydrogen production via photoelectrochemical water splitting," *Energy & Environmental Science*, vol. 7, p. 3264–3278, 2014.

[8] M. R. Shaner, H. A. Atwater, N. S. Lewis, and E. W. McFarland, "A comparative technoeconomic analysis of renewable hydrogen production using solar energy," *Energy & Environmental Science*, vol. 9, p. 2354–2371, 2016.

[9] Z. Chen, H. N. Dinh, and E. Miller, *Photoelectrochemical water splitting*. Springer, 2013.

[10] S. Hu, M. R. Shaner, J. A. Beardslee, M. Lichterman, B. S. Brunschwig, and N. S. Lewis, "Amorphous TiO_2 coatings stabilize Si, GaAs, and GaP photoanodes for efficient water oxidation," *Science*, vol. 344, p. 1005–1009, 2014.

[11] Y. W. Chen, J. D. Prange, S. Dühnen, Y. Park, M. Gunji, C. E. D. Chidsey, and P. C. McIntyre, "Atomic layer-deposited tunnel oxide stabilizes silicon photoanodes for water oxidation," *Nature Materials*, vol. 10, p. 539–544, 2011.

[12] M. S. Ahmad, A. K. Pandey, and N. A. Rahim, "Advancements in the development of TiO_2 photoanodes and its fabrication methods for dye sensitized solar cell (DSSC) applications. A review," *Renewable and Sustainable Energy Reviews*, vol. 77, p. 89–108, 2017.

[13] K. Sivula, "Defects give new life to an old material: electronically leaky titania as a photoanode protection layer," *ChemCatChem*, vol. 6, p. 2796–2797, 2014.

[14] W. Niu, X. Li, S. K. Karuturi, D. W. Fam, H. Fan, S. Shrestha, L. H. Wong, and A. I. Y. Tok, "Applications of atomic layer deposition in solar cells," *Nanotechnology*, vol. 26, p. 064001, 2015.

[15] X. Yang, R. Liu, C. Du, P. Dai, Z. Zheng, and D. Wang, "Improving hematite-based photoelectrochemical water splitting with ultrathin TiO_2 by atomic layer deposition," *ACS Applied Materials & Interfaces*, vol. 6, p. 12 005–12 011, 2014.

[16] M. T. McDowell, M. F. Lichterman, A. I. Carim, R. Liu, S. Hu, B. S. Brunschwig, and N. S. Lewis, "The influence of structure and processing on the behavior of TiO_2 protective layers for stabilization of n-Si/TiO_2/Ni photoanodes for water oxidation," *ACS Applied Materials & Interfaces*, vol. 7, p. 15 189–15 199, 2015.

[17] A. G. Scheuermann, J. D. Prange, M. Gunji, C. E. D. Chidsey, and P. C. McIntyre, "Effects of catalyst material and atomic layer deposited TiO_2 oxide thickness on the water oxidation performance of metal–insulator–silicon anodes," *Energy & Environmental Science*, vol. 6, p. 2487–2496, 2013.

[18] H. Sopha, M. Krbal, S. Ng, J. Prikryl, R. Zazpe, F. K. Yam, and J. M. Macak, "Highly efficient photoelectrochemical and photocatalytic anodic TiO_2 nanotube layers with additional TiO_2 coating," *Applied Materials Today*, vol. 9, p. 104–110, 2017.

[19] Z. Li, C. Yao, F. Wang, Z. Cai, and X. Wang, "Cellulose nanofiber-templated three-dimension TiO_2 hierarchical nanowire network for photoelectrochemical photoanode," *Nanotechnology*, vol. 25, p. 504005, 2014.

[20] X. Chen, L. Liu, and F. Huang, "Black titanium dioxide (TiO_2) nanomaterials," *Chemical Society Reviews*, vol. 44, p. 1861–1885, 2015.

[21] S. Hu, M. H. Richter, M. F. Lichterman, J. Beardslee, T. Mayer, B. S. Brunschwig, and N. S. Lewis, "Electrical, photoelectrochemical, and photoelectron spectroscopic investigation of the interfacial transport and energetics of amorphous TiO_2/Si heterojunctions," *The Journal of Physical Chemistry C*, vol. 120, p. 3117–3129, 2016.

[22] P. Chrysicopoulou, D. Davazoglou, C. Trapalis, and G. Kordas, "Optical properties of very thin (< 100 nm) sol–gel TiO_2 films," *Thin Solid Films*, vol. 323, p. 188–193, 1998.

[23] X. Chen and C. Burda, "The electronic origin of the visible-light absorption properties of C-, N- and S-doped TiO_2 nanomaterials," *Journal of the American Chemical Society*, vol. 130, p. 5018–5019, 2008.

[24] R. Asahi, T. Morikawa, T. Ohwaki, K. Aoki, and Y. Taga, "Visible-light photocatalysis in nitrogen-doped titanium oxides," *Science*, vol. 293, p. 269–271, 2001.

[25] R. Pandiyan, N. Delegan, A. Dirany, P. Drogui, and M. A. El Khakani, "Probing the electronic surface properties and bandgap narrowing of in situ N, W, and (W, N) doped magnetron-sputtered TiO_2 films intended for electrophotocatalytic applications," *The Journal of Physical Chemistry C*, vol. 120, p. 631–638, 2015.

[26] T. Morikawa, R. Asahi, T. Ohwaki, K. Aoki, and Y. Taga, "Band-gap narrowing of titanium dioxide by nitrogen doping," *Japanese Journal of Applied Physics*, vol. 40, p. L561, 2001.

[27] J. Tao, T. Luttrell, and M. Batzill, "A two-dimensional phase of TiO_2 with a reduced bandgap," *Nature Chemistry*, vol. 3, p. 296, 2011.

[28] S. Wendt, P. T. Sprunger, E. Lira, G. K. H. Madsen, Z. Li, J. Ø. Hansen, J. Matthiesen, A. Blekinge-Rasmussen, E. Lægsgaard, B. Hammer, and F. Besenbacher, "The role of interstitial sites in the Ti3d defect state in the band gap of titania," *Science*, vol. 320, p. 1755–1759, 2008.

[29] C. Di Valentin, G. Pacchioni, and A. Selloni, "Reduced and n-type doped TiO_2: nature of Ti^{3+} species," *The Journal of Physical Chemistry C*, vol. 113, p. 20 543–20 552, 2009.

[30] H. Yaghoubi, Z. Li, Y. Chen, H. T. Ngo, V. R. Bhethanabotla, B. Joseph, S. Ma, R. Schlaf, and A. Takshi, "Toward a visible light-driven photocatalyst: the effect of midgap-states-induced energy gap of undoped TiO_2 nanoparticles," *ACS Catalysis*, vol. 5, p. 327–335, 2014.

[31] B. Seger, D. S. Tilley, T. Pedersen, P. C. K. Vesborg, O. Hansen, M. Grätzel, and I. Chorkendorff, "Silicon protected with atomic layer deposited TiO_2: durability studies of photocathodic H_2 evolution," *RSC Advances*, vol. 3, p. 25 902–25 907, 2013.

[32] W.-H. Cheng, M. H. Richter, M. M. May, J. Ohlmann, D. Lackner, F. Dimroth, T. Hannappel, H. A. Atwater, and H.-J. Lewerenz, "Monolithic photoelectrochemical device for direct water splitting with 19% efficiency," *ACS Energy Letters*, vol. 3, p. 1795–1800, 2018.

[33] K. Qi, B. Cheng, J. Yu, and W. Ho, "A review on TiO_2-based Z-scheme photocatalysts," *Chinese Journal of Catalysis*, vol. 38, p. 1936–1955, 2017.

[34] "ASTM G173-03(2012), standard tables for reference solar spectral irradiances: Direct normal and hemispherical on 37° tilted surface, ASTM International, West Conshohocken, PA," 2012, www.astm.org, cited 1.8.2019.

[35] M. G. Walter, E. L. Warren, J. R. McKone, S. W. Boettcher, Q. Mi, E. A. Santori, and N. S. Lewis, "Solar water splitting cells," *Chemical Reviews*, vol. 110, p. 6446–6473, 2010.

[36] M. F. Weber and M. J. Dignam, "Efficiency of splitting water with semiconducting photoelectrodes," *Journal of the Electrochemical Society*, vol. 131, p. 1258–1265, 1984.

[37] J. A. Turner, "A realizable renewable energy future," *Science*, vol. 285, p. 1493–1493, 1999.

[38] J. R. Bolton, S. J. Strickler, and J. S. Connolly, "Limiting and realizable efficiencies of solar photolysis of water," *Nature*, vol. 316, p. 495, 1985.

[39] S. M. Sze and K. K. Ng, *Physics of semiconductor devices*. John wiley & sons, 2006.

[40] S. Chen and L.-W. Wang, "Thermodynamic oxidation and reduction potentials of photocatalytic semiconductors in aqueous solution," *Chemistry of Materials*, vol. 24, p. 3659–3666, 2012.

[41] Y. Xu and M. A. A. Schoonen, "The absolute energy positions of conduction and valence bands of selected semiconducting minerals," *American Mineralogist*, vol. 85, p. 543–556, 2000.

[42] K. K. Ghuman and C. V. Singh, "Effect of doping on electronic structure and photocatalytic behavior of amorphous TiO_2," *Journal of Physics: Condensed Matter*, vol. 25, p. 475501, 2013.

[43] C. Jin, B. Liu, Z. Lei, and J. Sun, "Structure and photoluminescence of the TiO_2 films grown by atomic layer deposition using tetrakis-dimethylamino titanium and ozone," *Nanoscale Research Letters*, vol. 10, p. 1–9, 2015.

[44] X. Chen, L. Liu, Z. Liu, M. A. Marcus, W.-C. Wang, N. A. Oyler, M. E. Grass, B. Mao, P.-A. Glans, Y. Y. Peter, J. Guo, and S. S. Mao, "Properties of disorder-engineered black titanium dioxide nanoparticles through hydrogenation," *Scientific Reports*, vol. 3, p. 1510, 2013.

[45] B. Mei, T. Pedersen, P. Malacrida, D. Bae, R. Frydendal, O. Hansen, P. C. K. Vesborg, B. Seger, and I. Chorkendorff, "Crystalline TiO_2: a generic and effective electron-conducting protection layer for photoanodes and -cathodes," *The Journal of Physical Chemistry C*, vol. 119, p. 15 019–15 027, 2015.

[46] H. Kato, M. Hori, R. Konta, Y. Shimodaira, and A. Kudo, "Construction of Z-scheme type heterogeneous photocatalysis systems for water splitting into H_2 and O_2 under visible light irradiation," *Chemistry Letters*, vol. 33, p. 1348–1349, 2004.

[47] E. N. K. Glover, S. G. Ellington, G. Sankar, and R. Palgrave, "The nature and effects of rhodium and antimony dopants on the electronic structure of TiO_2: towards design of Z-scheme photocatalysts," *Journal of Materials Chemistry A*, vol. 4, p. 6946–6954, 2016.

[48] H. Tada, T. Mitsui, T. Kiyonaga, T. Akita, and K. Tanaka, "All-solid-state Z-scheme in CdS–Au–TiO_2 three-component nanojunction system," *Nature Materials*, vol. 5, p. 782, 2006.

[49] F. Wu, X. Li, W. Liu, and S. Zhang, "Highly enhanced photocatalytic degradation of methylene blue over the indirect all-solid-state Z-scheme g-C3N4-RGO-TiO_2 nanoheterojunctions," *Applied Surface Science*, vol. 405, p. 60–70, 2017.

[50] J. Li, S. K. Cushing, P. Zheng, T. Senty, F. Meng, A. D. Bristow, A. Manivannan, and N. Wu, "Solar hydrogen generation by a CdS-Au-TiO_2 sandwich nanorod array enhanced with Au nanoparticle as electron relay and plasmonic photosensitizer," *Journal of the American Chemical Society*, vol. 136, p. 8438–8449, 2014.

[51] W. Kern, "The evolution of silicon wafer cleaning technology," *Journal Electrochemical Society*, vol. 137, p. 1887–1892, 1990.

[52] W. Kern and D. A. Puotion, "Cleaning solutions based on hydrogen peroxide for use in silicon semiconductor technology," *RCA Review 31*, vol. 31, p. 187–205, 1970.

[53] G. Coletti, P. C. P. Bronsveld, G. Hahn, W. Warta, D. Macdonald, B. Ceccaroli, K. Wambach, N. L. Quang, and J. M. Fernandez, "Impact of metal contamination in silicon solar cells," *Advanced Functional Materials*, vol. 21, p. 879–890, 2011.

[54] J. Gu, Y. Yan, J. L. Young, K. X. Steirer, N. R. Neale, and J. A. Turner, "Water reduction by a p-$GaInP_2$ photoelectrode stabilized by an amorphous TiO_2 coating and a molecular cobalt catalyst," *Nature materials*, vol. 15, p. 456, 2016.

[55] Q. Xie, Y.-L. Jiang, C. Detavernier, D. Deduytsche, R. L. Van Meirhaeghe, G.-P. Ru, B.-Z. Li, and X.-P. Qu, "Atomic layer deposition of TiO_2 from tetrakis-dimethyl-amido titanium or Ti isopropoxide precursors and H_2O," *Journal of Applied Physics*, vol. 102, p. 083521, 2007.

[56] C. Nordling, E. Sokolowski, and K. Siegbahn, "Precision method for obtaining absolute values of atomic binding energies," *Physical Review*, vol. 105, p. 1676–1677, 1957.

[57] M. Escher, N. Weber, M. Merkel, C. Ziethen, P. Bernhard, G. Schönhense, S. Schmidt, F. Forster, F. Reinert, B. Krömker, and D. Funnemann, "NanoESCA: a novel energy filter for imaging X-ray photoemission spectroscopy," *Journal of Physics: Condensed Matter*, vol. 17, p. S1329, 2005.

[58] M. Escher, K. Winkler, O. Renault, and N. Barrett, "Applications of high lateral and energy resolution imaging XPS with a double hemispherical analyser based spectromicroscope," *Journal of Electron Spectroscopy and Related Phenomena*, vol. 178–179, p. 303–316, May 2010.

[59] H. Hertz, "Ueber einen Einfluss des ultravioletten Lichtes auf die electrische Entladung," *Annalen der Physik*, vol. 267, p. 983–1000, 1887.

[60] A. Einstein, "Über einen die Erzeugung und Verwandlung des Lichtes betreffenden heuristischen Gesichtspunkt," *Annalen der Physik*, vol. 322, p. 132–148, 1905.

[61] D. Briggs, "XPS: Basic principles, spectral features and qualitative analysis," in *Surface Analysis by Auger and X-ray Photoelectron Spectroscopy*, D. Briggs and J. Grant, Eds. SurfaceSpectra, 2003, ch. 2.

[62] S. Hüfner, *Photoelectron spectroscopy: principles and applications.* Berlin; Heidelberg: Springer, 2010.

[63] S. M. Goldberg, C. S. Fadley, and S. Kono, "Photoionization cross-sections for atomic orbitals with random and fixed spatial orientation," *Journal of Electron Spectroscopy and Related Phenomena*, vol. 21, p. 285–363, 1981.

[64] R. Pugliese and G. Paolucci, "Atomic calculation of photoionization cross-sections and asymmetry parameters," https://vuo.elettra.eu/services/elements/WebElements.html, cited 24.2.2019.

[65] J. J. Yeh and I. Lindau, "Atomic subshell photoionization cross sections and asymmetry parameters: $1 \leq Z \leq 103$," *Atomic Data and Nuclear Data Tables*, vol. 32, p. 1–155, 1985.

[66] "NIST X-ray Photoelectron Spectroscopy Database, NIST Standard Reference Database Number 20, National Institute of Standards and Technology, Gaithersburg MD, 20899," 2000.

[67] W. Werner, "Electron transport in solids," in *Surface Analysis by Auger and X-ray Photoelectron Spectroscopy*, D. Briggs and J. Grant, Eds. SurfaceSpectra, 2003, ch. 10.

[68] S. Tanuma, "Electron attenuation lengths," in *Surface Analysis by Auger and X-ray Photoelectron Spectroscopy*, D. Briggs and J. Grant, Eds. SurfaceSpectra, 2003, ch. 11.

[69] M. P. Seah and W. A. Dench, "Quantitative electron spectroscopy of surfaces: A standard data base for electron inelastic mean free paths in solids," *Surface and Interface Analysis*, vol. 1, p. 2–11, 1979.

[70] B. Krömker, M. Escher, D. Funnemann, D. Hartung, H. Engelhard, and J. Kirschner, "Development of a momentum microscope for time resolved band structure imaging," *Review of Scientific Instruments*, vol. 79, p. 053702, 2008.

[71] K. Lahtonen, "Oxygen adsorption-induced nanostructures on copper and silver-copper alloys surfaces investigated by scanning tunneling microscopy and electron spectroscopy," Ph.D. dissertation, Tampere University of Technology, 2008.

[72] K. Lahtonen, M. Lampimäki, P. Jussila, M. Hirsimäki, and M. Valden, "Instrumentation and analytical methods of an X-ray photoelectron spectroscopy–scanning tunneling microscopy surface analysis system for studying nanostructured materials," *Review of Scientific Instruments*, vol. 77, p. 083901, 2006.

[73] "NanoESCA operating manual part 6 of 6 X-ray source, technician's model 36-100 focused X-ray source component manual, version 1.0," 2006, Omicron NanoTechnology.

[74] "Instruction manual VUV source HIS13, version 2.3," Omicron NanoTechnology.

[75] "Instruction manual mercury UV source, version 2.1," Omicron NanoTechnology.

[76] W. Eberhardt, "Synchrotron radiation: A continuing revolution in X-ray science – diffraction limited storage rings and beyond," *Journal of Electron Spectroscopy and Related Phenomena*, vol. 200, p. 31–39, 2015, special Anniversary Issue: Volume 200.

[77] R. Nyholm, J. N. Andersen, U. Johansson, B. N. Jensen, and I. Lindau, "Beamline I311 at MAX-LAB: a VUV/soft X-ray undulator beamline for high resolution electron spectroscopy," *Nuclear Instruments and Methods in Physics Research Section A: Accelerators, Spectrometers, Detectors and Associated Equipment*, vol. 467–468, p. 520–524, 2001, 7th Int.Conf. on Synchrotron Radiation Instrumentation.

[78] I. W. Drummond, "XPS: Instrumentation and performance," in *Surface Analysis by Auger and X-ray Photoelectron Spectroscopy*, D. Briggs and J. Grant, Eds. SurfaceSpectra, 2003, ch. 2.

[79] K. Artyushkova and J. E. Fulghum, "XPS imaging," in *Surface Analysis by Auger and X-ray Photoelectron Spectroscopy*, D. Briggs and J. Grant, Eds. SurfaceSpectra, 2003, ch. 24.

[80] C. J. Blomfield, "Spatially resolved X-ray photoelectron spectroscopy," *Journal of Electron Spectroscopy and Related Phenomena*, vol. 143, p. 241–249, 2005, electron Energy Loss Spectroscopy in the Electron Microscope.

[81] "NanoESCA, ultimate ESCA & k-space imaging," Scienta Omicron GmbH, https://www.scientaomicron.com/en/products/nanoesca-/instrument-concept, cited 14.9.2019.

[82] "NanoESCA tachnical reference manual instrument, version 1.1," 2012, Omicron NanoTechnology.

[83] W. Telieps and E. Bauer, "An analytical reflection and emission UHV surface electron microscope," *Ultramicroscopy*, vol. 17, p. 57–65, 1985.

[84] E. Bauer, M. Mundschau, W. Swiech, and W. Telieps, "Surface studies by low-energy electron microscopy (LEEM) and conventional UV photoemission electron microscopy (PEEM)," *Ultramicroscopy*, vol. 31, p. 49–57, 1989.

[85] E. Bauer, "Low energy electron microscopy," *Reports on Progress in Physics*, vol. 57, p. 895–938, sep 1994.

[86] D. Briggs and J. T. Grant, "Perspectives on XPS and AES," in *Surface Analysis by Auger and X-ray Photoelectron Spectroscopy*, D. Briggs and J. Grant, Eds. SurfaceSpectra, 2003, ch. 1.

[87] H. J. Mathieu, "Auger electron spectroscopy," in *Surface Analysis – The Principal Techniques*, 2nd ed., J. C. Vickerman and I. S. Gilmore, Eds. John Wiley & Sons, Ltd, 2009, ch. 2.

[88] B. D. Ratner and D. G. Castner, "Electron spectroscopy for chemical analysis," in *Surface Analysis – The Principal Techniques*, 2nd ed., J. C. Vickerman and I. S. Gilmore, Eds. John Wiley & Sons, Ltd, 2009, ch. 3.

[89] G. Margaritondo, "X-ray photoelectron spectroscopy and imaging at synchrotrons," in *Surface Analysis by Auger and X-ray Photoelectron Spectroscopy*, D. Briggs and J. Grant, Eds. SurfaceSpectra, 2003, ch. 26.

[90] J. F. Moulder and J. Chastain, *Handbook of X-ray Photoelectron Spectroscopy: A Reference Book of Standard Spectra for Identification and Interpretation of XPS Data.* Physical Electronics Division, Perkin-Elmer Corporation, 1992.

[91] J. D. Lee, O. Gunnarsson, and L. Hedin, "Transition from the adiabatic to the sudden limit in core-level photoemission: A model study of a localized system," *Physical Review B*, vol. 60, p. 8034, 1999.

[92] L. Hedin and J. D. Lee, "Sudden approximation in photoemission and beyond," *Journal of electron spectroscopy and related phenomena*, vol. 124, p. 289–315, 2002.

[93] M. Patt, "Bulk and surface sensitive energy-filtered photoemission microscopy using synchrotron radiation for the study of resistive switching memories," Ph.D. dissertation, Forschungszentrums Jülich, 2016.

[94] F. de la Peña, N. Barrett, L. F. Zagonel, M. Walls, and O. Renault, "Full field chemical imaging of buried native sub-oxide layers on doped silicon patterns," *Surface Science*, vol. 604, p. 1628–1636, 2010.

[95] CasaXPS: Processing Software for XPS, AES, SIMS and More. Available (accessed on 7.5.2019): http://www.casaxps.com/.

[96] J. Walton and N. Fairley, "Noise reduction in X-ray photoelectron spectromicroscopy by a singular value decomposition sorting procedure," *Journal of Electron Spectroscopy and Related Phenomena*, vol. 148, p. 29–40, 2005.

[97] J. Walton and N. Fairley, *The Casa Cookbook, Part 2: XPS Image Processing*, A. Carrick, Ed. Acolyte Science, Cheshire, 2011.

[98] O. Renault, R. Brochier, A. Roule, P.-H. Haumesser, B. Krömker, and D. Funnemann, "Work-function imaging of oriented copper grains by photoemission," *Surface and Interface Analysis: An International Journal devoted to the development and application of techniques for the analysis of surfaces, interfaces and thin films*, vol. 38, p. 375–377, 2006.

[99] L. F. Zagonel, M. Bäurer, A. Bailly, O. Renault, M. Hoffmann, S. J. Shih, D. Cockayne, and N. Barrett, "Orientation-dependent work function of in situ annealed strontium titanate," *Journal of Physics: Condensed Matter*, vol. 21, p. 314013, 2009.

[100] L. Diederich, O. Küttel, P. Aebi, and L. Schlapbach, "Electron affinity and work function of differently oriented and doped diamond surfaces determined by photoelectron spectroscopy," *Surface Science*, vol. 418, p. 219–239, 1998.

[101] R. Schlaf, "Calibration of photoemission spectra and work function determination," University of South Florida, http://rsl.eng.usf.edu/Documents/Tutorials/PEScalibration.pdf, cited 20.10.2019.

[102] O. Renault, R. Brochier, P.-H. Haumesser, N. Barrett, B. Krömker, and D. Funnemann, "Energy-filtered PEEM imaging of polycrystalline Cu surfaces with work function contrast and high lateral resolution," *e-Journal of Surface Science and Nanotechnology*, vol. 4, p. 431–434, 2006.

[103] E. Guth and C. J. Mullin, "Electron emission of metals in electric fields II. Field dependence of the surface photo-effect," *Physical Review*, vol. 59, p. 867, 1941.

[104] D. D. Macdonald, "Reflections on the history of electrochemical impedance spectroscopy," *Electrochimica Acta*, vol. 51, p. 1376–1388, 2006.

[105] S. Takabayashi, R. Nakamura, and Y. Nakato, "A nano-modified Si/TiO_2 composite electrode for efficient solar water splitting," *Journal of Photochemistry and Photobiology A: Chemistry*, vol. 166, p. 107–113, 2004.

[106] V. Pfeifer, T. E. Jones, S. Wrabetz, C. Massué, J. J. Velasco Vélez, R. Arrigo, M. Scherzer, S. Piccinin, M. Hävecker, A. Knop-Gericke, and R. Schlögl, "Reactive oxygen species in iridium-based OER catalysts," *Chemical Science*, vol. 7, p. 6791–6795, 2016.

[107] V. Pfeifer, T. Jones, J. Velasco Vélez, M. Greiner, C. Massué, R. Arrigo, D. Teschner, F. Girgsdies, M. Scherzer, J. Allan, M. Hashagen, G. Weinberg, S. Piccinin, M. Hävecker, A. Knop-Gericke, and R. Schlögl, "The electronic structure of iridium oxide electrodes active in water splitting," *Physical Chemistry Chemical Physics*, vol. 18, p. 2292–2296, 12 2015.

[108] V. Pfeifer, T. E. Jones, J. J. Velasco Vélez, C. Massué, R. Arrigo, D. Teschner, F. Girgsdies, M. Scherzer, M. T. Greiner, J. Allan, M. Hashagen, G. Weinberg, S. Piccinin, M. Hävecker, A. Knop-Gericke, and R. Schlögl, "The electronic structure of iridium and its oxides," *Surface and Interface Analysis*, vol. 48, p. 261–273, 2016.

[109] S.-i. Ogawa, T. Kouzaki, T. Yoshida, and R. Sinclair, "Interface microstructure of titanium thin-film/silicon single-crystal substrate correlated with electrical barrier heights," *Journal of Applied Physics*, vol. 70, p. 827–832, 1991.

[110] C. Y. Kim, S.-W. Kim, C.-H. Hong, D.-W. Kim, H.-K. Baik, and C. N. Whang, "Effects of titanium silicide on AuSiTi/n-GaN ohmic contact systems," *Journal of Crystal Growth*, vol. 189, p. 720–724, 1998.

[111] H. Jeon and R. J. Nemanich, "Surface morphology of $TiSi_2$ on silicon," *Thin Solid Films*, vol. 184, p. 357–363, 1990.

[112] M. Perego, G. Seguini, G. Scarel, M. Fanciulli, and F. Wallrapp, "Energy band alignment at TiO_2/Si interface with various interlayers," *Journal of Applied Physics*, vol. 103, p. 043509, 2008.

[113] J. L. Freeouf, T. N. Jackson, S. E. Laux, and J. M. Woodall, "Effective barrier heights of mixed phase contacts: Size effects," *Applied Physics Letters*, vol. 40, p. 634–636, 1982.

[114] R. C. Rossi, M. X. Tan, and N. S. Lewis, "Size-dependent electrical behavior of spatially inhomogeneous barrier height regions on silicon," *Applied Physics Letters*, vol. 77, p. 2698–2700, 2000.

[115] R. C. Rossi and N. S. Lewis, "Investigation of the size-scaling behavior of spatially nonuniform barrier height contacts to semiconductor surfaces using ordered nanometer-scale nickel arrays on silicon electrodes," *The Journal of Physical Chemistry B*, vol. 105, p. 12 303–12 318, 2001.

[116] X. Liu, G. Zhu, X. Wang, X. Yuan, T. Lin, and F. Huang, "Progress in black titania: a new material for advanced photocatalysis," *Advanced Energy Materials*, vol. 6, p. 1600452, 2016.

[117] G. Wang, H. Wang, Y. Ling, Y. Tang, X. Yang, R. C. Fitzmorris, C. Wang, J. Z. Zhang, and Y. Li, "Hydrogen-treated TiO_2 nanowire arrays for photoelectrochemical water splitting," *Nano Letters*, vol. 11, p. 3026–3033, 2011.

[118] A. Lepcha, C. Maccato, A. Mettenbörger, T. Andreu, L. Mayrhofer, M. Walter, S. Olthof, T.-P. Ruoko, A. Klein, M. Moseler *et al.*, "Electrospun black titania nanofibers: influence of hydrogen plasma-induced disorder on the electronic structure and photoelectrochemical performance," *The Journal of Physical Chemistry C*, vol. 119, p. 18 835–18 842, 2015.

[119] X. Chen, L. Liu, Y. Y. Peter, and S. S. Mao, "Increasing solar absorption for photocatalysis with black hydrogenated titanium dioxide nanocrystals," *Science*, vol. 331, p. 746–750, 2011.

[120] H. Jeon, C. A. Sukow, J. W. Honeycutt, G. A. Rozgonyi, and R. J. Nemanich, "Morphology and phase stability of $TiSi_2$ on Si," *Journal of Applied Physics*, vol. 71, p. 4269–4276, 1992.

[121] W.-C. Yang, H. Ade, and R. J. Nemanich, "Shape stability of $TiSi_2$ islands on Si(111)," *Journal of Applied Physics*, vol. 95, p. 1572–1576, 2004.

[122] J. L. Tedesco, J. E. Rowe, and R. J. Nemanich, "Titanium silicide islands on atomically clean Si(100): Identifying single electron tunneling effects," *Journal of Applied Physics*, vol. 107, p. 123715, 2010.

[123] A. Sunda-Meya, D. J. Smith, and R. J. Nemanich, "Shape transition and migration of $TiSi_2$ nanostructures embedded in a Si matrix," *Journal of Applied Physics*, vol. 110, p. 094304, 2011.

[124] A. Arranz and C. Palacio, "The room temperature growth of Ti on sputter-cleaned Si(100): Composition and nanostructure of the interface," *Surface Science*, vol. 588, p. 92–100, 2005.

[125] C. Palacio and A. Arranz, "Formation of the Si/Ti interface," *Applied Surface Science*, vol. 253, p. 4283–4288, 2007.

[126] U. Diebold, "The surface science of titanium dioxide," *Surface Science Reports*, vol. 48, p. 53–229, 2003.

[127] T.-D. Nguyen-Phan, S. Luo, D. Vovchok, J. Llorca, J. Graciani, J. F. Sanz, S. Sallis, W. Xu, J. Bai, L. F. J. Piper, D. E. Polyansky, E. Fujita, S. D. Senanayake, D. J. Stacchiola, and J. A. Rodriguez, "Visible light-driven H_2 production over highly dispersed ruthenia on rutile TiO_2 nanorods," *ACS Catalysis*, vol. 6, p. 407–417, 2015.

[128] J. C. Hill, A. T. Landers, and J. A. Switzer, "An electrodeposited inhomogeneous metal–insulator–semiconductor junction for efficient photoelectrochemical water oxidation," *Nature Materials*, vol. 14, p. 1150, 2015.

[129] S. Li, Q. Zhao, D. Meng, D. Wang, and T. Xie, "Fabrication of metallic charge transfer channel between photoanode Ti/Fe_2O_3 and cocatalyst CoO_x: an effective strategy for promoting photoelectrochemical water oxidation," *Journal of Materials Chemistry A*, vol. 4, p. 16 661–16 669, 2016.

[130] J. A. Turner, "A nickel finish protects silicon photoanodes for water splitting," *Science*, vol. 342, p. 811–812, 2013.

[131] M. J. Kenney, M. Gong, Y. Li, J. Z. Wu, J. Feng, M. Lanza, and H. Dai, "High-performance silicon photoanodes passivated with ultrathin nickel films for water oxidation," *Science*, vol. 342, p. 836–840, 2013.

[132] K. Sun, F. H. Saadi, M. F. Lichterman, W. G. Hale, H.-P. Wang, X. Zhou, N. T. Plymale, S. T. Omelchenko, J.-H. He, K. M. Papadantonakis, B. S. Brunschwig, and N. S. Lewis, "Stable solar-driven oxidation of water by semiconducting photoanodes protected by transparent catalytic nickel oxide films," *Proceedings of the National Academy of Sciences*, vol. 112, p. 3612–3617, 2015.

[133] D. Barreca, G. Carraro, A. Gasparotto, C. Maccato, M. E. A. Warwick, K. Kaunisto, C. Sada, S. Turner, Y. Gönüllü, T.-P. Ruoko, L. Borgese, E. Bontempi, G. Van Tendeloo, H. Lemmetyinen, and S. Mathur, "Fe_2O_3–TiO_2 nanoheterostructure photoanodes for highly efficient solar water oxidation," *Advanced Materials Interfaces*, vol. 2, p. 1500313, 2015.

[134] J. Dong, J. Han, W. Qiu, S. Huang, and W. Gao, "TiO_2 with hybrid nanostructures via anodization: fabrication and its mechanism," *Scripta Materialia*, vol. 69, p. 374–376, 2013.

[135] Y. Lin, S. Zhou, S. W. Sheehan, and D. Wang, "Nanonet-based hematite heteronanostructures for efficient solar water splitting," *Journal of the American Chemical Society*, vol. 133, p. 2398–2401, 2011.

ORIGINAL RESEARCH PAPERS

Paper I

Improved stability of atomic layer deposited amorphous TiO_2 photoelectrode coatings by thermally induced oxygen defects

Markku Hannula, Harri Ali-Löytty, Kimmo Lahtonen, Essi Sarlin, Jesse Saari, and Mika Valden

Chemistry of Materials, 30, p. 1199–1208, 2018
DOI: 10.1021/acs.chemmater.7b02938.

CHEMISTRY OF MATERIALS
Cite This: *Chem. Mater.* 2018, 30, 1199−1208
Article
pubs.acs.org/cm

Improved Stability of Atomic Layer Deposited Amorphous TiO_2 Photoelectrode Coatings by Thermally Induced Oxygen Defects

Markku Hannula,[†] Harri Ali-Löytty,[†] Kimmo Lahtonen,[†] Essi Sarlin,[‡] Jesse Saari,[†] and Mika Valden*[,†]

[†]Surface Science Group, Laboratory of Photonics, Tampere University of Technology, P.O. Box 692, FI-33101 Tampere, Finland
[‡]Materials Science, Tampere University of Technology, P.O. Box 589, FI-33101 Tampere, Finland

Supporting Information

ABSTRACT: Amorphous titanium dioxide (a-TiO_2) combined with an electrocatalyst has shown to be a promising coating for stabilizing traditional semiconductor materials used in artificial photosynthesis for efficient photoelectrochemical solar-to-fuel energy conversion. In this study we report a detailed analysis of two methods of modifying an undoped thin film of atomic layer deposited (ALD) a-TiO_2 without an electrocatalyst to affect its performance in water splitting reaction as a protective photoelectrode coating. The methods are high-temperature annealing in ultrahigh vacuum and atomic hydrogen exposure. A key feature in both methods is that they preserve the amorphous structure of the film. Special attention is paid to the changes in the molecular and electronic structure of a-TiO_2 induced by these treatments. On the basis of the photoelectrochemical results, the a-TiO_2 is susceptible to photocorrosion but significant improvement in stability is achieved after heat treatment in vacuum at temperatures above 500 °C. On the other hand, the hydrogen treatment does not increase the stability despite the ostensibly similar reduction of a-TiO_2. The surface analysis allows us to interpret the improved stability to the thermally induced formation of O^- species within a-TiO_2 that are essentially electronic defects in the anionic framework.

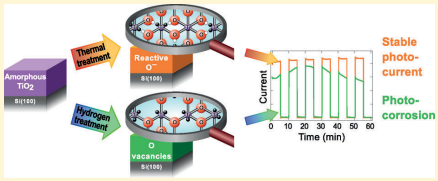

INTRODUCTION

The ever-growing demand for energy and increasing concern for sustainable development are forcing humankind to seek for new technologies for harnessing energy from renewable sources. One promising alternative is the production of hydrogen by a solar energy-driven process called artificial photosynthesis. In this process, the energy of the incoming photons is converted into chemical energy of the molecular bonds by dissociating water molecules into hydrogen and oxygen.[1] The dissociation reaction requires semiconducting electrodes that are stable in electrochemical conditions, can efficiently absorb solar energy, can support the redox reaction of water molecules on their surfaces, and are cost-efficient. Several traditional semiconductor materials such as silicon, gallium arsenide, and gallium phosphide have electronic structures with suitable band potentials to enable the water oxidation half reaction. However, these materials are unstable under oxidizing conditions. Thus, the oxidation of the electrode material itself competes with the water oxidation leading to either photocorrosion or passivation of the electrode surface.[1−3] For this reason the electrode surface must be coated with a suitable protective layer. One promising material for this application is titanium dioxide (TiO_2), which has attracted tremendous research interest during the last decades.

Traditionally the TiO_2 research has concentrated on its crystalline anatase, rutile, and brookite polymorphs, but in recent years several studies have revealed that the amorphous counterpart might actually be more advantageous due to its electric "leakiness".[2,4−6] In other words, the electronically defective nature of the amorphous TiO_2 makes it more conductive. Good conductivity is important in avoiding tunneling barriers that reduce the photocurrent or increase the required overpotential.[7] In insulating, tunneling based protection layers these losses would constitute a significant disadvantage because the film has to be at least several nanometers thick to avoid pinhole defects.[8,9] In the chemical sense, the increased conductivity can be attributed to the reduction of Ti^{4+} cations to the Ti^{3+} state. This can be achieved, for example, by n-type doping, where tetravalent Ti is substituted by pentavalent cation such as Nb or Sn or by substituting O with F.[10] Another option is to modify the bond structure by creating O vacancies or Ti^{3+} interstitials.[10] The advantage of the latter method is that no new elements have to be introduced to the structure.

In the present study we report a detailed analysis of two approaches for modifying ALD grown a-TiO_2 ultrathin films to address the question of intrinsic stability of a-TiO_2 in photoelectrochemical (PEC) energy conversion: thermal treatment and atomic hydrogen treatment. The PEC properties and the electrochemical stability of the post-treated a-TiO_2 ultrathin films are investigated with standard electrochemical measurements in conjunction with simulated solar irradiation and

Received: July 13, 2017
Revised: December 24, 2017
Published: February 2, 2018

DOI: 10.1021/acs.chemmater.7b02938
Chem. Mater. 2018, 30, 1199−1208

correlated with the molecular and electronic structure obtained by photoelectron spectroscopy analysis. In both thermal and atomic hydrogen treatment, a 28.7 nm thick a-TiO_2 film deposited on a Si single crystal is used as a substrate. The first modification method is based on high-temperature annealing (up to 900 °C) in ultrahigh vacuum (UHV). Interestingly, X-ray photoelectron spectroscopy (XPS) and X-ray diffraction (XRD) results reveal that the amorphous structure is preserved despite the high annealing temperature. In the thermal method the improved "leakiness" is shown to be induced by charge transfer within the ionic framework of a-TiO_2. Moreover, the elemental composition of the a-TiO_2 film is not altered by the treatment. On the other hand, in atomic H treatment, the H atoms react with O leading to the desorption of water molecules and creation of O vacancies. Ultraviolet photoelectron spectroscopy (UPS) is used to show that in both methods the valence band structure of a-TiO_2 is severely modified by occupied Ti 3d derived states above the valence band maximum (VBM) of a stoichiometric TiO_2.[10,11] Furthermore, our PEC results reveal that a-TiO_2 is susceptible to severe photocorrosion under photoelectrochemical water splitting conditions. Achieving the PEC stability for a bare a-TiO_2 coating without an electrocatalyst requires the thermally induced formation of oxide defects in the ionic framework. These findings regarding the intrinsic stability of thermally treated a-TiO_2 are likely to promote the use of a-TiO_2 thin films in photoelectrochemical and other functional applications. Moreover, the a-TiO_2 combined with an active electrocatalyst exhibits advantageous approach stabilizing traditional semiconductor materials used for water splitting reaction.

MATERIALS AND METHODS

The P-doped (resistivity 1−20 Ω cm) n-type Si(100) wafers were purchased from Wafer World, Inc. (Florida). The 400 μm thick, 3-in. diameter prepolished wafers had been cut in (100) orientation with ±1° accuracy. For the experiments 10 × 10 mm^2 squares were cleaved. The Si substrates were first cleaned by sonicating them for 45 min in 99.5% EtOH followed by a combination of annealing and atomic hydrogen treatments in UHV. The details of the UHV cleaning procedure are described in ref 12. In short, the samples were first annealed to 1000 °C to remove native oxide. After this they were exposed to atomic hydrogen at 800 °C (10 min) and 400 °C (10 min) at p_H = 1.0 × 10^{-7} mbar, which removed the segregated Cu and Ni impurities, respectively. In all stages, the sample temperature was monitored with a pyrometer (Land Cyclops 160B) using an emissivity value of ε = 0.60. The pyrometer reading was calibrated against type K thermocouple measurements in a separate system. After annealing, the surface cleanness and structure were verified by X-ray photoelectron spectroscopy and low energy electron diffraction (LEED) (Figure S1 in the Supporting Information and ref 12). After the UHV cleaning, the samples were cooled down in vacuum and transferred to the ALD system through the atmosphere. The exposure to air was kept less than 5 min.

ALD deposition of a-TiO_2 was carried out using a Picosun Sunale ALD R200 Advanced reactor. Tetrakis(dimethylamido)titanium(IV) ($Ti(N(CH_3)_2)_4$, TDMAT, 99%, Strem Chemicals Inc., France), deionized water, and N_2 (99.9999%, Oy AGA Ab, Finland) were used as the Ti precursor, O precursor, and carrier/purge/venting gas, respectively. a-TiO_2 films were prepared with two different thicknesses: 28.7 nm for PEC and XPS/UPS measurements and 200 nm for XRD measurements because the thinner film did not give sufficient XRD signal intensity. The number of ALD pulses for the films were 804 and 5600, respectively. The film thickness was verified by ellipsometry (Rudolph Auto EL III Ellipsometer, Rudolph Research Analytical).

During the ALD, the Si substrate temperature was kept at 200 °C. The vapor pressure of the TDMAT was increased to 3.6 mbar by heating the precursor bubbler to 76 °C, and the precursor gas delivery line was heated to 85 °C to prevent condensation. The water bubbler was sustained at 18 °C by a Peltier element for stability control. The substrate temperature was stabilized for 30 min before starting the deposition. The 200 °C ALD growth temperature was selected because it results in amorphous growth whereas higher ALD temperatures produce strongly crystallized anatase TiO_2.[13,14] On the other hand, much lower temperatures would result in incomplete precursor dissociation leading to higher remnant impurity concentrations, especially nitrogen from TDMAT. Low temperatures also produce more stoichiometric TiO_2 which, based on our preliminary experiments, cannot be modified by the post-treatments as effectively as the films grown at 200 °C (Figure S2).

After the ALD deposition, the samples were cooled down in nitrogen gas before transferring them back to UHV for post-treatments and photoelectron spectroscopy (PES) measurements. The exposure to ambient atmosphere during the transfer was approximately 5 min.

The post-treatments were performed in the preparation chamber of the NanoESCA spectromicroscopy system (Omicron NanoTechnology GmbH)[15] and they were divided into two sets: (1) thermal treatment and (2) atomic hydrogen treatment. Thermal treatments were conducted cumulatively in 100 °C steps from 400 to 900 °C in UHV keeping the chamber pressure in the 10^{-9} mbar range during the annealings. The upper limit for the annealing series was selected based on our previous studies where a-TiO_2 became completely reduced above 950 °C.[12] The heating setup consisted of a resistive PBN-heating element mounted to a manipulator close to the backside of the sample and the sample held in a Mo sample plate. The temperature was increased to the target value in approximately 3 min and then kept constant for 10 min after which the sample was let to cool down to <100 °C. The temperature was monitored with a pyrometer. After each annealing step, the sample was transferred to the analysis chamber under UHV conditions for PES measurements or alternatively removed from the UHV system for PEC studies.

The atomic hydrogen treatments were performed in the same preparation chamber as the thermal treatment series. The sample temperature was kept at 300 °C during the atomic hydrogen exposure. The hydrogen treatment series was made cumulatively so that the total exposure times of 1, 5, 10, and 50 min were achieved. The hydrogen flux was produced by using EFM H Atomic Hydrogen Source (Omicron NanoTechnology GmbH). The source is based on leaking hydrogen gas through a heated tungsten capillary which causes thermal dissociation of hydrogen molecules with a dissociation efficiency close to 100%.[16] The following parameters were used: e-beam acceleration voltage = 1000 V, e-beam emission current = 40 mA, filament current = 2.00 A. Hydrogen gas pressure in the preparation chamber was adjusted to 1.0 × 10^{-6} mbar, and the sample was set in line with the capillary tube. After each hydrogen exposure step the sample was transferred to the analysis chamber for PES.

The PES measurements were conducted in the analysis chamber of the NanoESCA system with a base pressure below 1 × 10^{-10} mbar. Focused monochromatized Al Kα radiation ($h\nu$ = 1486.5 eV) was utilized for core level XPS whereas valence band UPS spectra were measured with a focused nonmonochromatized He Iα radiation ($h\nu$ = 21.22 eV) using HIS 13 VUV Source (Focus GmbH). The spectra were collected with a photoemission electron microscope (PEEM) paired with a single hemispherical energy analyzer. The energy resolution of the analyzer was set to 400 meV (pass energy 100 eV, slit 1 μm) and 100 meV (pass energy 50 eV, slit 0.5 μm) for XPS and UPS, respectively. The analysis area was set to 230 μm in diameter for XPS and 95 μm for UPS, corresponding to the maximum spot sizes of the radiation sources. Large analysis areas ensured that the results represent the average surface composition. Previous small area XPS results have shown that both the ALD grown and post-treated surfaces are homogeneous.

The chemical states of the elements were determined from the core level XP spectra by least-squares fitting of asymmetric Gaussian−

DOI: 10.1021/acs.chemmater.7b02938
Chem. Mater. 2018, 30, 1199−1208

Lorentzian line shapes after subtracting a Shirley type background (Table S1). The determination of the electron band structure near the Fermi edge was made by analyzing the UPS valence band spectra. Because of large inelastic secondary electron background a Tougaard background was subtracted and the remaining intensity was fitted with Finite Lorentzian Asymmetric peaks (Table S2). The analysis was made in CasaXPS software version 2.3.17PR1.1[17] using the Scofield photoionization cross sections as relative sensitivity factors. The binding energy (E_b) scale was calibrated by setting the O 1s main peak (O in a-TiO_2) to 530.20 eV.

The influence depth of the hydrogen treatment was estimated by comparing the measured Ti 2p photoelectron spectroscopy results with a simulation. For this comparison the Ti 2p attenuation length was calculated by using the TPP-2M[18] formula in the QUASES-Tougaard software package.[19] For the 1028 eV kinetic energy (corresponding to Ti $2p_{3/2}$), the formula gave an attenuation length of λ = 2.2 nm.

Thermal treatment of ALD grown a-TiO_2 is known to induce crystallinity in some cases.[13,20,21] For this reason, structural characterization of the 200 nm thick samples both in as-deposited (after ALD growth) and thermally treated conditions was carried out by using XRD (Panalytical Empyrean multipurpose diffractometer) with Cu Kα radiation (λ = 1.5405 Å) and 45 kV and 40 mA cathode voltage and current, respectively. The samples were scanned in 2θ between 20 and 40°. The XRD data was postprocessed by subtracting the background and removing the Cu Kα_2 X-ray satellite peaks.

Photoelectrochemical performance was studied in a homemade PEC cell (PTFE body, volume 3.3 cm^3), using a three-electrode system controlled by Autolab PGSTAT12 potentiostat (Metrohm AG). The studied samples were inserted between a rubber O-ring and a stainless steel plate. The steel plate on the back side provided the electrical contact and the O ring ensured a well-defined 0.28 cm^2 planar projected electrode surface area. An Ag/AgCl electrode (Leak-Free LF-2, Warner Instruments, LLC) and Pt wire (surface area 0.82 cm^2) were used as reference and counter electrodes, respectively, in an aqueous solution of 1 M NaOH (pH = 13.6). The potential values were converted to the reversible hydrogen electrode (RHE) scale by the equation $V_{RHE} = V_{Ag/AgCl} + 0.197\ V + pH \times 0.059\ V$. A simulated solar spectrum was produced with a HAL-C100 solar simulator (Asahi Spectra Co., Ltd., JIS Class A at 400−1100 nm with an AM1.5G filter), and the intensity was adjusted to 1.00 Sun using a 1 sun checker (model CS-30, Asahi Spectra Co., Ltd.). The photon flux was directed to the sample front surface through a 5 mm thick quartz glass window and 18 mm thick electrolyte layer. The PEC testing was started by studying the current−voltage characteristics in dark and under simulated sunlight (Figure S3). After this linear sweep voltammetry, the sample was subjected to an electrochemical stability test by biasing the sample to water redox potential of +1.23 V vs RHE under simulated solar light. Both light and dark currents were measured by chopping the light off and on every 5 min. The data collection was continued for 60 min corresponding to a total of six light/dark cycles. The as-deposited and 500 °C UHV annealed samples were also subjected for a longer stability test under continuous illumination.

RESULTS AND DISCUSSION

Photoelectrochemical Activity and Stability. The PEC behavior of the thermally and hydrogen treated a-TiO_2 samples was tested by studying their PEC responses at +1.23 V vs RHE. Figure 1 illustrates the photocurrent density as a function of time for four samples. The highest current was actually reached with the untreated as-deposited sample. However, after about 10 min illumination, the photocurrent started to decrease sharply. This indicates that the current is not due to the oxygen evolution reaction but instead caused by the dissolution of the a-TiO_2 layer and therefore an indication of a-TiO_2 photocorrosion. The result was confirmed with a long exposure in 1 M NaOH which dissolved the 30 nm film completely in 5 h as shown by the current density drop and the photograph in the inset of the Figure 1. Similar results were obtained for the hydrogen treated and the 400 °C thermally treated surfaces. On the other hand, all samples annealed at 500 °C or higher showed stable photocurrents for at least 20 h and close to zero dark current. It was also found that as the thermal treatment temperature approached 900 °C, the photocurrent declined. This is likely due to the insulating Si oxide layer that is formed at the Si−a-TiO_2 interface, as will be discussed later.

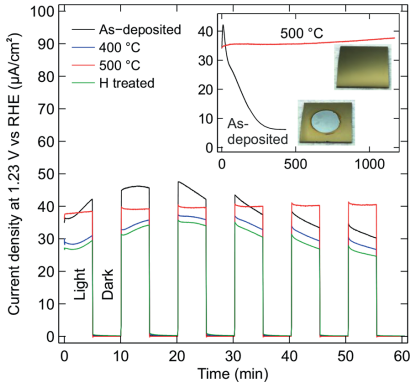

Figure 1. Chronoamperometric testing of four a-TiO_2/Si electrodes in 1 M NaOH (aq.) under the illumination intensity of 1.00 Sun. Black: as-deposited film without post-treatment, blue: annealed at 400 °C, red: annealed at 500 °C, green: hydrogen treated for 10 min at 300 °C. The inset shows the photocurrent density of the as-deposited and 500 °C annealed samples during a long stability test under continuous irradiation. The photographs illustrate the surface at the end of the stability test. Photoanodes were kept at constant +1.23 V vs reversible hydrogen electrode (RHE).

The instability of the as-deposited, hydrogen treated, and below 500 °C annealed samples was somewhat surprising, because there are reports of apparently similar ALD grown amorphous TiO_2 films used as PEC electrodes.[4,22] In many cases, the TiO_2 film has been even much thinner than 30 nm.[7] It should also be noted that in most studies, Ni, IrO_2, or some other electrocatalyst material has been evaporated or sputtered on top of the TiO_2 layer.[4,7,8,22,23] On the basis of our results, the protective properties of the a-TiO_2 film may not originate from the native film itself, but they may be attributed to the combination of TiO_2 and the electrocatalyst. However, with a thermal treatment the as-deposited a-TiO_2 film can also be made stable for PEC applications.

Molecular Structure of Amorphous TiO_2. To achieve molecular level understanding of the reasons why thermally and hydrogen treated a-TiO_2 films exhibit such different photoelectrochemical behaviors, we analyzed the samples by XPS. Special attention was paid to the formation of the different Ti 2p oxidation states in both treatment series. The measured O 1s and Ti 2p XP spectra are shown in Figure 2.

Ti was identified in three different oxidation states, which correspond to Ti^{4+} (stoichiometric a-TiO_2) at 459.00 ± 0.20 eV, Ti^{3+} at 457.20 ± 0.20 eV, and Ti^{2+} at 455.95 ± 0.20 eV. All subsequent analysis is based only on the 3/2 spin−orbit coupled state but both 1/2 and 3/2 states had to be fitted because the splitting is only about 5.7 eV thus causing overlap between $Ti^{4+}_{3/2}$ and $Ti^{2+}_{1/2}$ components. The 1/2 states were fitted

DOI: 10.1021/acs.chemmater.7b02938
Chem. Mater. 2018, 30, 1199−1208

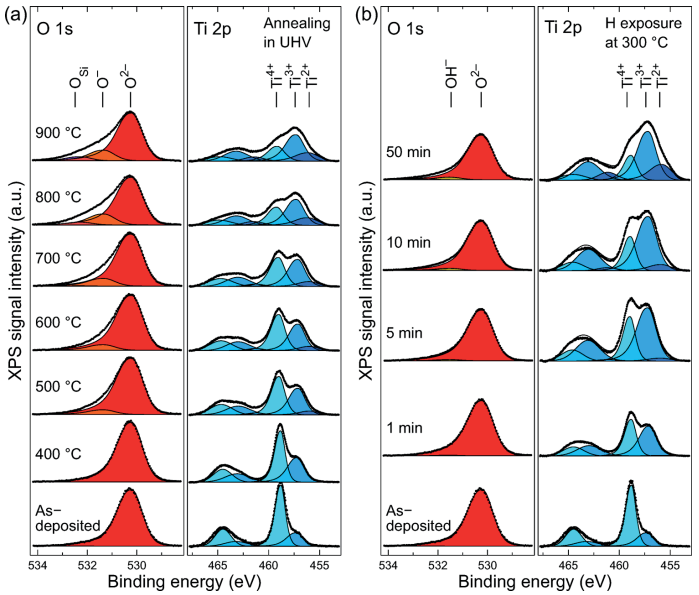

Figure 2. Ti 2p and O 1s XP spectra for (a) thermal treatment and (b) hydrogen treatment series. The Ti 2p spectra are fitted for both 3/2 and 1/2 doublets with three synthetic oxide components in each spin−orbit coupled state.

with an area ratio of 0.43 ± 0.03 compared to the corresponding 3/2 state. It is noteworthy that no metallic Ti was observed at any stage of the post-treatments. In O 1s spectra, four different chemical states were identified. In all cases the main peak (set to 530.20 eV in calibration) corresponded to O^{2-} anions in a-TiO_2. In the thermal treatment series another state was identified at 531.33 eV, which is denoted as O^-. In the literature, this binding energy region is usually associated with hydroxyl groups,[24,25] carbonate-like species or other carbon related impurities,[26] or oxygen-deficient titanium oxide (such as TiO_x, where $1.35 < x < 1.65$).[27] The first two explanations would be plausible on the as-deposited surface, because it may have hydroxyl groups or carbon impurities that have adsorbed from air or remained in the structure as residues from the incompletely reacted ALD precursors. However, the peak at 531.33 eV is visible only after 500 °C and higher thermal treatments when the hydroxyl groups and carbon impurities have desorbed from the surface (Figure S4). Above all, our results clearly show that the O 1s peak at 531.33 eV is not associated with the decrease of oxygen content, because the O/Ti ratio remains constant throughout the thermal treatment series (see Figure 3). Thus, the buildup of O^- peak is assumed to result from localized charge transfer between anionic and cationic frameworks during thermally induced reduction, as will be discussed later. Second minor component (E_b = 532.25 ± 0.10 eV) in O 1s spectra appeared during high temperature annealings at 800 and 900 °C. This peak, denoted as O_{Si}, is associated with Si oxide impurities. At these temperatures small amount (<1.8 at %) of oxidized Si was observed in Si 2p spectra (Figure S5). Importantly, both O^- and O_{Si} were observed only in the thermal treatment series. On

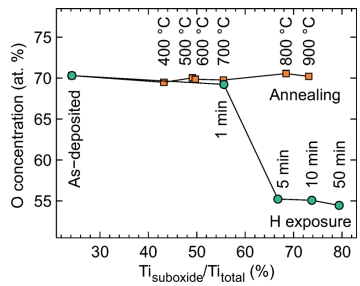

Figure 3. O concentration as a function of the relative $Ti^{3+/2+}$ concentration. For the annealing series, the O content remains constant despite the strong reduction observed in Ti 2p transition. In the hydrogen treatment series, the O concentration approached the 50% limit which implies a TiO stoichiometry.

the other hand, the spectra measured from the hydrogen exposed samples started to show a slowly growing component at 531.50 eV as the hydrogen exposure time was increased. This component was associated with a process where a chemisorbed hydrogen atom does not desorb from the surface but forms Ti−O−H compounds. The concentration of the OH^- component is in all cases less than 6% of all O atoms, which indicates that most of the reactions between a-TiO_2 and H lead to the desorption of O as water molecules.

The bottom spectrum in Figure 2 noted as as-deposited represents the situation directly after ALD growth without any post-treatment. In this case the O 1s spectrum can be fitted

DOI: 10.1021/acs.chemmater.7b02938
Chem. Mater. 2018, 30, 1199−1208

with one asymmetric Gaussian−Lorentzian component. In addition to O and Ti, the as-deposited surface had approximately 1.5 at % of carbon and <0.3 at % of nitrogen impurities (Figure S4). These are however completely removed after the first thermal or hydrogen treatment and do not contribute to our results. Otherwise the surfaces were clean with the exception of the previously mentioned Si oxide after 800 and 900 °C annealing steps. The origin of the Si was traced back to the TDMAT precursor material by continuing the annealing at 900 °C for a total of 30 min. After this prolonged treatment, the Si had disappeared from the surface. This implies that there is a limited source of segregating Si trapped inside the ALD film instead of Si from the substrate diffusing through the film. From the photoelectrochemical point of view this small Si impurity concentration may actually be beneficial because Si doping has been shown to improve photocatalytic activity of TiO_2 nanotubes.[28]

It is noteworthy that the ALD grown surface is not stoichiometric TiO_2 but has approximately 26% of Ti in Ti^{3+} oxidation state, which can be accounted for interstitial Ti ions or O vacancies.[10,29] As the postprocessing advances to higher temperatures or longer hydrogen exposure times the amount of Ti suboxides (Ti^{3+} and Ti^{2+}) starts to increase. This increases the number of excess electrons in the structure that occupy the electronic states near the Fermi edge, which in turn improves the conductivity.[10] For PEC applications this is an important aspect as the photocurrent must be transferred through the a-TiO_2 film. Despite the somewhat similar reduction behavior of Ti in both the thermal and hydrogen treatment series, the chemical compositions of the surfaces are strongly distinct when comparing the different reduction methods. This is illustrated in Figure 3 which shows the relative O concentration on the surface. The calculation is based on the total area of the components shown in Figure 2.

For stoichiometric TiO_2, the theoretical O concentration is 67 at %. In our case, the value should be slightly lower because 26% of Ti is in the Ti^{3+} oxidation state already in the as-deposited film. The discrepancy between the theoretical value and the observed 70 at % value originates mainly from a small error in the relative sensitivity factor of Ti 2p, which does not account for the TiO_2 satellite features outside the analyzed energy region. The most pronounced feature in Figure 3 is, however, the difference between thermally and H treated samples. In the H treatment series, the O content decreases with increasing H exposure time. This is as expected because, as shown in Figure 2b, the Ti becomes strongly reduced but almost all of the remaining O stays in the original O^{2-} oxidation state. This implies that O reacting with H atoms is removed from the material, most probably as water, and only a small concentration of Ti−OH compounds is formed. The removal of a neutral O atom from the structure leaves two excess electrons on the empty states of Ti cations. The electrons can be either localized or distributed among the 5-fold coordinated Ti^{3+} ions surrounding the O vacancy. According to the simulations conducted by Di Valentin et al.,[10] the energetically most favorable situations are when the electrons are localized to the Ti^{3+} ion next to the vacancy and the next nearest neighboring Ti cation or alternatively one electron is localized to 5-fold coordinated Ti^{3+} and the other electron is completely delocalized.

Contrary to the hydrogen treatment, the thermal treatment leaves the O concentration practically constant at 70 at % in all studied annealing temperatures. This result is unexpected because Ti is strongly reduced and one could assume that this leads to a decreasing O content. The explanations for this anomalous behavior are scarce in the literature because most of the Ti oxide research has traditionally concentrated on crystalline anatase or rutile forms instead of the amorphous phase. In crystalline TiO_2, the thermal treatment usually leads to a reduction of only a couple of percent of Ti cations.[30] In that case, the question of what the O/Ti ratio represents is not valid nor easy to study. For example, Ti^{3+} cations are known to readily diffuse toward the bulk,[11,31] which may alter the results with small concentrations.

One possible explanation for the high O content can be trapped molecular O_2. This is however unlikely, because in crystalline TiO_2 molecular O_2 is known to desorb at about 110 °C,[32] and the desorption energy should not differ too much for amorphous TiO_2. Thus, the desorption is expected to occur at much lower temperature than what is used in the thermal treatment series. More plausible explanation is localized charge transfer from anions to cations. For example, Pfeifer et al. have studied charge transfer in amorphous IrO_2, which has a structure very similar to amorphous TiO_2. They have introduced an IrO_2 reduction model, where the creation of an Ir vacancy results in two Ir^{3+} ions and six localized reactive O^- species.[33−35] Interestingly, we also observe the O^- formation in a-TiO_2, even without the Ti vacancy formation. If sufficient amount of thermal energy is introduced to a Ti−O bond, the electron transfer from anionic to cationic framework can result in stable 5-fold-coordinated Ti^{3+} and 2-fold-coordinated O^- states in the matrix. This model is supported by the observed binding energy changes in the Ti 2p transition. In the as-deposited film, the Ti^{4+} peak is located at 458.80 eV but starts to shift linearly toward higher binding energies (up to 459.20 eV) as the temperature of the thermal treatment is increased. This can be explained by the increased number of O^- species, which attract electrons from the neighboring, still 6-fold-coordinated Ti^{4+} species, thus increasing their effective nuclear charge.

More detailed analysis of the Ti reduction can be obtained by analyzing the relative concentrations of different Ti oxidation states in Figure 2. Figure 4 illustrates the evolution of these states as the total Ti suboxide (Ti^{3+} and Ti^{2+}) concentration increases. In the thermally treated samples, the reduction starts with only Ti^{3+} being formed at temperatures below 400 °C. At higher temperatures, however, the formation rate of both Ti^{3+} and Ti^{2+} suboxide species is somewhat similar and follows the total suboxide concentration linearly. In contrast, at the hydrogen treated surfaces the initial reduction is strongly focused on the formation of the Ti^{3+} states, and the amount of Ti^{2+} species starts to increase significantly only after the total suboxide concentration has reached about 70%.

To better understand the difference between these reduction mechanisms, we conducted Monte Carlo simulations with two different reduction mechanisms (see the Supporting Information for details). The reason for these simulations was to qualitatively validate the reduction mechanisms that were deduced based on the XPS data of the Ti oxidation states.

For thermally treated samples, the best agreement between the simulation (solid blue lines in Figure 4a) and experimental data was obtained with a mechanism where the original Ti^{4+} state can be reduced directly to Ti^{3+} or Ti^{2+}. The reduction from Ti^{4+} to Ti^{2+} state is a possible alternative for the reduction from Ti^{4+} to Ti^{3+} oxidation state because the process does not involve external atoms, such as hydrogen, to be introduced into

DOI: 10.1021/acs.chemmater.7b02938
Chem. Mater. 2018, 30, 1199−1208

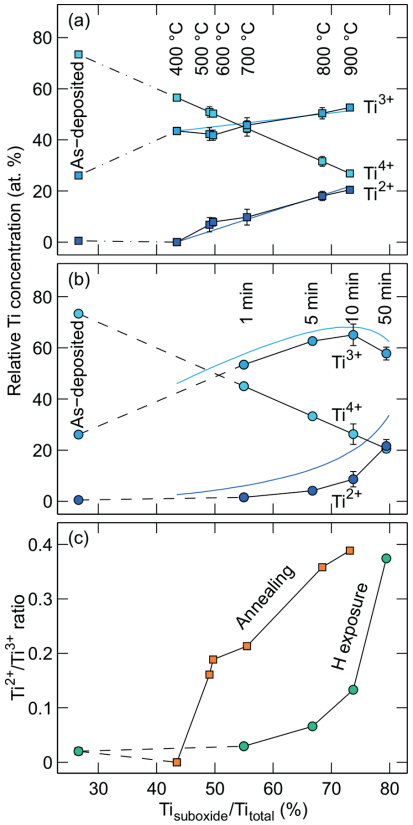

Figure 4. Relative concentration of Ti oxidation states in (a) thermal and (b) hydrogen treatment series and (c) the Ti^{2+}/Ti^{3+} ratio as a function of the total suboxide concentration. All experimental values (squares and circles) are determined from the Ti 2p transition shown in Figure 2a. The error bars represent the range of variation from repeated measurements. The solid blue lines represent the Monte Carlo simulation results.

the matrix. On the other hand, for hydrogen treatment a double reduction from Ti^{4+} to Ti^{2+} state is not likely because a reduction event can be considered as a process where one hydrogen atom at a time encounters the titanium oxide surface and removes one O atom. This process can take place if the Ti atom is either a part of the original TiO_2 structure or it can already be in a partially reduced Ti_2O_3 form. Thus, the removal of one O atom as OH compound leads to Ti_2O_3 or TiO configuration, respectively. The simulation results (blue lines in Figure 4b) support this type of "one step reduction" mechanism. The exclusive reduction options either from Ti^{4+} to Ti^{3+} or from Ti^{3+} to Ti^{2+} lead to a behavior, where the formation of Ti^{3+} cations is pronounced at the beginning. However, as the amount of Ti^{4+} cations decreases and Ti^{3+} cations increases, the probability for Ti^{3+} to Ti^{2+} reduction increases and the relative Ti^{2+} concentration starts to increase sharply as shown by the Ti^{2+}/Ti^{3+} ratio in the Figure 4c.

In addition to the different reduction mechanisms in thermal and hydrogen treatment simulations, the latter required a modification in the *x*-axis scaling. The simulated curves had to be scaled down by 17% to match with the measured data points. This can be interpreted so that 17% of the Ti atoms inside the XPS information depth are deeper than the influence depth of the hydrogen exposure. Thus, these atoms can never be reduced which leads to a sharp decrease in the Ti^{3+} concentration earlier than what the unscaled simulation predicts. On the basis of the Beer–Lambert law and the attenuation length of the Ti 2p photoelectrons (λ = 2.2 nm), the hydrogen exposure influence depth is calculated to be 4.0 nm.

The above-discussed reduction mechanisms are summarized in eqs 1 and 2 for thermal treatment and hydrogen treatment, respectively. The ↑ sign in eq 2 depicts the desorption of water molecules from the surface.

$$TiO_2 \xrightarrow[T > 400\ °C]{T \le 400\ °C} \begin{matrix} Ti^{3+}O^{2-}O^{-} \\ \text{or} \\ Ti^{3+}O^{2-}O^{-} \text{ or } Ti^{2+}O_2^{-} \end{matrix} \quad (1)$$

$$2TiO_2 \xrightarrow{+2H} Ti_2O_3 + H_2O_{\uparrow} \xrightarrow{+2H} 2TiO + H_2O_{\uparrow} \quad (2)$$

In thermal treatment at above 400 °C, the reduction process may lead directly to either Ti^{3+} or Ti^{2+} formation whereas in hydrogen treated samples the Ti^{3+} is the preferred reduction product as long as there is a significant amount of stoichiometric TiO_2 available.

In addition to the oxidation states, the thermal and hydrogen treatments may affect the molecular ordering of the a-TiO_2 films. Qualitative information about these structural changes can be obtained by analyzing the XPS peak shapes. Accurate curve fitting of the Ti 2p spectra in Figure 2 required that the full width at half-maximum (fwhm) of the peaks was allowed to vary. Blue squares and circles in Figure 5 illustrate the variation of the Ti^{4+} component fwhm. Other oxidation states gave

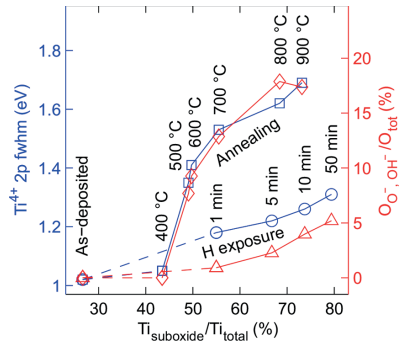

Figure 5. Structural disorder of thermally and hydrogen treated surfaces. For Ti, the disorder increase is interpreted from the fwhm widening of the Ti^{4+} 2p state (blue squares and circles). For O, a qualitatively similar behavior can be seen in the increase of the area of the shoulder peaks (peaks O^- and OH^- in Figure 2) (red diamonds and triangles).

DOI: 10.1021/acs.chemmater.7b02938
Chem. Mater. 2018, 30, 1199–1208

qualitatively similar results. In the hydrogen exposure series, the fwhm growth is only 24% whereas in thermally treated samples the peak width increases 66% as the suboxide concentration is increased from the original 26 to 73% (900 °C and 10 min treatments). The increase in peak width is a sign of increasing structural disorder.[34] This can be interpreted as a relaxation of internal stress among the chains of the octahedral TiO_2 units. Thus, it can be concluded that the thermal breaking of Ti−O bonds and the formation of Ti^{3+} and O^- species introduce structural changes in the amorphous material. Figure 5 also shows the relative concentration of O^- (in thermal treatment) and OH^- (in hydrogen treatment) states compared to the total O content. For hydrogen treated samples, the OH^- increase is relatively weak, because most of the O ions participating in the structural changes desorb from the material as water molecules. For the thermally treated samples, the increase in O^- states correlates excellently with the Ti 2p fwhm changes thus consolidating the model that the peak widening is caused by changes in molecular bonding and subsequent deformation of the amorphous structure. Interestingly, the onset temperature for the O^- species formation coincides with the temperature where photoelectrochemical stability was obtained. Thus, we may conclude that the O^- species stabilizes the a-TiO_2 from photocorrosion.

Phase Stability of the Amorphous TiO_2. Thermal treatment of a-TiO_2 at high temperature is known to induce partial crystallization, especially if the annealing is made in atmospheric pressure.[2,13] Our analysis of the Ti 2p spectral features clearly indicated that the annealing in UHV increases the structural disorder. This was further supported by XRD measurements of similarly heat treated 200 nm thick a-TiO_2 films as shown in Figure 6 along with the spectra measured from rutile and anatase reference samples.

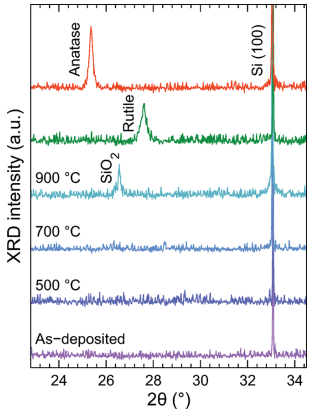

Figure 6. XRD patterns from the thermally treated a-TiO_2 films in addition to the spectra measured from the rutile and anatase reference samples. The films do not show any crystalline TiO_2 features at temperatures from 200 °C (as-deposited) to 900 °C. The SiO_2 peak in the 900 °C diffractogram is due to thin SiO_2 film at the Si−a-TiO_2 interface. The anatase and rutile references were obtained from TiO_2 films grown at 100 and 200 °C followed by annealing in air at 700 °C for 45 min, respectively.

The XRD results were consistent with the XPS results showing no indication of crystalline phases of TiO_2 in the thermally treated films. This is most advantageous in terms of using the films for PEC applications, because amorphous films are known to protect the underlying semiconductor better than crystalline films and also exhibit higher photocurrent conductivity.[2] The only emerging diffraction feature as a result of annealing was the SiO_2 related peak which appeared during the 900 °C thermal treatment. TiO_2 is known to donate O to Si at high temperatures, which produces a thin SiO_2 film at the Si−TiO_2 interface.[36] Importantly, the insulating SiO_2 film at the interface limits the current transfer required for efficient photoelectrochemical water splitting. This explains the observed PEC response where higher annealing temperatures produced smaller photocurrent densities.

Modification of the Valence Band Structure. Figure 7a,b shows the UP spectra of the thermal and hydrogen treated a-TiO_2/Si samples. The valence band (VB) ($E_b \approx 3.3-12$ eV) is fitted with three states corresponding to TiO_2 orbitals.[37,38] The highest energy band is associated with the nonbonding O 2p orbitals (π-type). Below that are the π- and σ-type molecular orbitals of TiO_2. In the spectrum of the as-deposited sample there is an additional peak at 10.2 eV (denoted as γ) which is produced by the impurities such as OH or CO groups on the surface.[11,39] This state disappears immediately during the first thermal or hydrogen treatment, which together with the core level XP spectra verifies the purity of the studied films. Additionally, a new peak with the same binding energy appears after 800 and 900 °C thermal treatments. This is caused by Si oxide formed when the residual Si impurity from the film segregates to the surface.[40] The UPS spectral feature observed at the 2−3 eV range is a combination of the valence band structure and He Iβ satellite line. The latter accounts for approximately 30% of the total intensity at this energy range.

For pure stoichiometric TiO_2, the band gap is about 3.0−3.4 eV depending on the crystal structure[38,41,42] and the conduction band minimum is located close to the Fermi energy. This is in good agreement with our as-deposited sample where the valence band maximum (VBM) is located at a binding energy of 3.3 eV as determined by extrapolating the linear region of the lower energy side of the VB to the zero intensity baseline. During the treatments, the VBM shows minor gradual shift to 3.5 or 3.6 eV for thermally and hydrogen treated samples, respectively. In hydrogen treatment series the density of the nonbonding O 2p states decreases with increasing exposure time which is in concordance with the aforementioned removal of O atoms from the structure. On the other hand, in thermally treated samples the density of the O $2p_{n/b}$ states remains rather constant from 400 to 700 °C. After this, there is a sudden decrease in the density which can be associated with some of the O atoms reacting with the surface segregated Si atoms resulting in the formation of the γ state.

The Ti 3d state just below the Fermi edge is playing a major role in determining the photoactivity of the a-TiO_2/Si surface. These in-gap states provide a pathway for electron transfer between the bulk electrode material and the electrolyte[9,41] and also effectively narrow the band gap thus improving the absorption of longer wavelengths.[43] The in-gap states divide the band gap in two smaller sub gaps thus providing an intermediate stepping stone for photoexcitation at lower energies.[44] The in-gap states of TiO_2 have often been ascribed to dopants or impurities (e.g., C, S, N, W, Mn),[10,38,43−45] $Ti^{3+/2+}$ interstitials,[10,11] or bridging O vacancies.[10,37] In our

DOI: 10.1021/acs.chemmater.7b02938
Chem. Mater. 2018, 30, 1199−1208

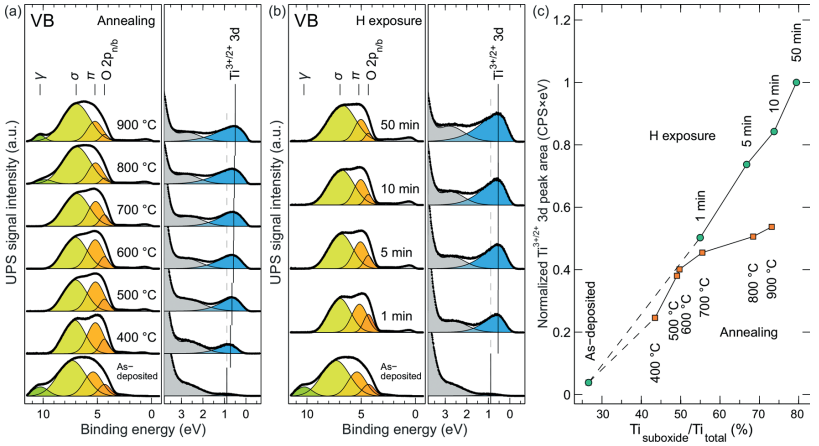

Figure 7. Ultraviolet photoemission valence band (VB) spectra after (a) thermal and (b) hydrogen treatments of a-TiO_2. The main components originating from the a-TiO_2 film are the σ and π molecular orbitals together with the O 2p nonbonding orbitals. In addition to these components, the reduced a-TiO_2 has a significant Ti 3d component as shown in blue in the magnified views. In the case of the as-deposited surface the γ component can be associated with the σ states of hydroxyl groups adsorbed from the atmosphere.[11] For 800 and 900 °C annealed samples, the same component position corresponds to the electronic states in SiO_2 which is formed by the surface segregated Si.[40] Part c illustrates the area of the $Ti^{3+/2+}$ oxidation state related Ti 3d peak. For hydrogen treatment series the area of Ti 3d suboxide states increases linearly whereas in thermal treatment the area starts to saturate after 700 °C annealing.

case, the impurity contribution can be excluded because the as-deposited surface has the highest C and N concentration accumulated from the air exposure and ALD precursor residues but still shows no in-gap density of states. Instead, when the surface is exposed to elevated temperatures or hydrogen atoms, the area of the $Ti^{3+/2+}$ 3d component starts to increase rapidly. For hydrogen treated samples, the density of the in-gap state shows rather linear increase as a function of the total hydrogen exposure induced suboxide concentration, as illustrated in Figure 7c. The position of the peak remains constant at E_b = 0.54 eV, which suggests that the peak is related to only one type of chemical state. The observed binding energy is in good agreement with the theoretically calculated value for $Ti^{3+/2+}$ 3d states caused by O vacancies,[10] thus supporting the model that the peak is produced solely by the removal of O atoms.

In the thermal treatment series, the growth of the $Ti^{3+/2+}$ 3d component is more subtle, especially above 60% suboxide concentration, and the peak position shifts toward the Fermi edge with the increasing treatment temperature. The shift from E_b = 0.72 to 0.50 eV can be interpreted such that the peak is a convolution of two different chemical states: the Ti^{3+} cation where Ti has only one localized excess electron or Ti^{2+} with two localized excess electrons as discussed previously in the reduction mechanism section. Thus, the increasing Ti^{2+}/Ti^{3+} ratio pushes the total in-gap density of states to smaller binding energy.

■ CONCLUSIONS

The presented results show two methods for modifying the molecular structure and electronic states of the ALD grown a-TiO_2 thin film on a semiconductor electrode surface. Both the thermal treatment in UHV and the atomic hydrogen treatment lead to a partially restructured amorphous phase, where the appearance of the in-gap $Ti^{3+/2+}$ 3d electronic states narrows the effective band gap. Importantly, both methods preserve the amorphous phase of the a-TiO_2 film. This is advantageous for photoelectrochemical applications as several recent studies have shown that the underlying semiconductor electrodes can be protected more efficiently with a conformal a-TiO_2 film rather than with its crystalline counterparts.

The studied post-treatment methods lead to considerably distinct chemical compositions as summarized in Figure 8. In the thermal treatment series, the relative concentration of O and Ti atoms remains constant but some electrons are transferred from anionic to cationic network. This leads to the formation of localized Ti^{3+} and Ti^{2+} species and O^- species. Importantly, the annealing procedure in UHV does not introduce any crystallization, but on the contrary decreases the structural order by relieving the strain in the amorphous lattice. By comparison, the atomic hydrogen treatment removes O atoms creating O vacancies surrounded by Ti cations in Ti^{3+} or Ti^{2+} valence state.

From the photoelectrochemical point of view, the as-deposited a-TiO_2 is susceptible to severe photocorrosion under photoelectrochemical water oxidation conditions. The stability of a-TiO_2 can be obtained after heat treatment at >500 °C in vacuum. This was attributed to the formation of O^- species that are essentially electronic defects in the anionic framework. At elevated temperatures above 500 °C, the a-TiO_2 thin film starts to react with the underlying Si substrate which produces an insulating SiO_2 interface layer thus lowering the photocurrent. On the other hand, the hydrogen treated samples were found to be unstable in alkaline electrochemical conditions. On the basis of the photocurrent measurements, the photocorrosion of the hydrogen treated samples was comparable to that of the as-deposited samples.

DOI: 10.1021/acs.chemmater.7b02938
Chem. Mater. 2018, 30, 1199−1208

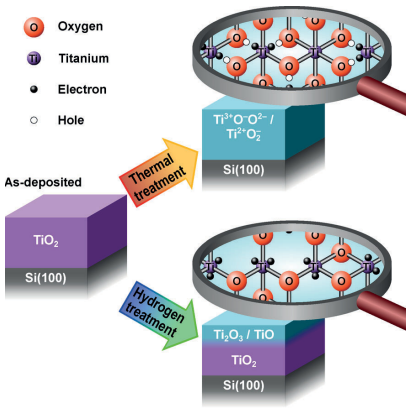

Figure 8. Schematic representation of the chemical and electronic changes in the a-TiO_2 ultrathin films as a result of the thermal and hydrogen post-treatments. The thermal treatment breaks bonds between Ti and O atoms leaving the elemental composition intact. The electron transfer from O to Ti results in excess electrons that occupy the Ti 3d state, which improves charge transfer properties. Additionally, the thermal treatment enhances the photoelectrochemical stability of the film via formation of O^- species that are essentially electronic defects in the anionic framework. In contrast, atomic hydrogen treatment creates an electronically "leaky" film via formation of O vacancies resulting in a photoelectrochemically unstable film.

In addition to optimizing the surface chemical and electronic structure, large scale manufacturing of cost-efficient water splitting devices would require optimization of the morphological structure, such as utilization of porous nanomaterials or nanowires.[46,47] This would increase the reactive surface area thus increasing the achievable photocurrent. However, the planar model systems used in this study provide valuable information about the possible a-TiO_2 post-treatment routes. Combining the knowledge obtained here with the nanostructured substrates and highly active electrocatalyst materials[2,4,8] can lead to a significant improvement in photoelectrodes utilizing a-TiO_2 ultrathin film coatings.

■ ASSOCIATED CONTENT

Supporting Information

The Supporting Information is available free of charge on the ACS Publications website at DOI: 10.1021/acs.chemmater.7b02938.

Additional XPS spectra, photoelectrochemical current−voltage curves, XPS/UPS fitting parameters, and details of the Monte Carlo simulations (PDF)

■ AUTHOR INFORMATION

Corresponding Author

*E-mail: mika.valden@tut.fi.

ORCID

Markku Hannula: 0000-0003-1110-7439

Notes

The authors declare no competing financial interest.

■ ACKNOWLEDGMENTS

This work was supported by the Academy of Finland (Decision Numbers 141481, 286713, and 309920). M.H. was supported by the Tampere University of Technology Graduate School. H.A.-L. was supported by the Jenny and Antti Wihuri Foundation.

■ REFERENCES

(1) Walter, M. G.; Warren, E. L.; McKone, J. R.; Boettcher, S. W.; Mi, Q.; Santori, E. A.; Lewis, N. S. Solar Water Splitting Cells. *Chem. Rev.* **2010**, *110*, 6446−6473.

(2) Hu, S.; Shaner, M. R.; Beardslee, J. A.; Lichterman, M.; Brunschwig, B. S.; Lewis, N. S. Amorphous TiO_2 Coatings Stabilize Si, GaAs, and GaP Photoanodes for Efficient Water Oxidation. *Science* **2014**, *344*, 1005−1009.

(3) Chen, S.; Wang, L.-W. Thermodynamic Oxidation and Reduction Potentials of Photocatalytic Semiconductors in Aqueous Solution. *Chem. Mater.* **2012**, *24*, 3659−3666.

(4) Hu, S.; Richter, M. H.; Lichterman, M. F.; Beardslee, J.; Mayer, T.; Brunschwig, B. S.; Lewis, N. S. Electrical, Photoelectrochemical, and Photoelectron Spectroscopic Investigation of the Interfacial Transport and Energetics of Amorphous TiO_2/Si Heterojunctions. *J. Phys. Chem. C* **2016**, *120*, 3117−3129.

(5) Pham, H. H.; Wang, L.-W. Oxygen Vacancy and Hole Conduction in Amorphous TiO_2. *Phys. Chem. Chem. Phys.* **2015**, *17*, 541−550.

(6) Scheuermann, A. G.; Lawrence, J. P.; Kemp, K. W.; Ito, T.; Walsh, A.; Chidsey, C. E. D.; Hurley, P. K.; McIntyre, P. C. Design Principles for Maximizing Photovoltage in Metal-oxide-protected Water-Splitting Photoanodes. *Nat. Mater.* **2016**, *15*, 99−105.

(7) Chen, Y. W.; Prange, J. D.; Dühnen, S.; Park, Y.; Gunji, M.; Chidsey, C. E. D.; McIntyre, P. C. Atomic Layer-Deposited Tunnel Oxide Stabilizes Silicon Photoanodes for Water Oxidation. *Nat. Mater.* **2011**, *10*, 539−544.

(8) Scheuermann, A. G.; Prange, J. D.; Gunji, M.; Chidsey, C. E. D.; McIntyre, P. C. Effects of Catalyst Material and Atomic Layer Deposited TiO_2 Oxide Thickness on the Water Oxidation Performance of Metal-Insulator-Silicon Anodes. *Energy Environ. Sci.* **2013**, *6*, 2487−2496.

(9) Sivula, K. Defects Give New Life to an Old Material: Electronically Leaky Titania as a Photoanode Protection Layer. *ChemCatChem* **2014**, *6*, 2796−2797.

(10) Di Valentin, C.; Pacchioni, G.; Selloni, A. Reduced and n-Type Doped TiO_2: Nature of Ti^{3+} Species. *J. Phys. Chem. C* **2009**, *113*, 20543−20552.

(11) Wendt, S.; Sprunger, P. T.; Lira, E.; Madsen, G. K. H.; Li, Z.; Hansen, J. Ø.; Matthiesen, J.; Blekinge-Rasmussen, A.; Lægsgaard, E.; Hammer, B.; Besenbacher, F. The Role of Interstitial Sites in the Ti3d Defect State in the Band Gap of Titania. *Science* **2008**, *320*, 1755−1759.

(12) Hannula, M.; Lahtonen, K.; Ali-Löytty, H.; Zakharov, A.; Isotalo, T.; Saari, J.; Valden, M. Fabrication of Topographically Microstructured Titanium Silicide Interface for Advanced Photonic Applications. *Scr. Mater.* **2016**, *119*, 76−81.

(13) Jin, C.; Liu, B.; Lei, Z.; Sun, J. Structure and Photoluminescence of the TiO_2 Films Grown by Atomic Layer Deposition Using Tetrakis-Dimethylamino Titanium and Ozone. *Nanoscale Res. Lett.* **2015**, *10*, 95.

(14) Aarik, J.; Aidla, A.; Kiisler, A.-A.; Uustare, T.; Sammelselg, V. Effect of Crystal Structure on Optical Properties of TiO_2 Films Grown by Atomic Layer Deposition. *Thin Solid Films* **1997**, *305*, 270−273.

(15) Omicron Nanotechnology. *NanoESCA*, 2017; http://www.scientaomicron.com.

(16) Omicron Nanotechnology. *Atomic Hydrogen Source EFM-H*, 2017; http://www.scientaomicron.direct/16/thin-film-deposition-products/efm-h.

(17) *CasaXPS: Processing Software for XPS, AES, SIMS and More*, 2017; http://www.casaxps.com.

DOI: 10.1021/acs.chemmater.7b02938
Chem. Mater. 2018, 30, 1199−1208

(18) Tanuma, S.; Powell, C. J.; Penn, D. R. Calculations of Electron Inelastic Mean Free Paths. V. Data for 14 Organic Compounds Over the 50−2000 eV Range. *Surf. Interface Anal.* **1994**, *21*, 165−176.
(19) Tougaard, S. *QUASES: Software for Quantitative XPS/AES of Surface Nano-Structure by Analysis of the Peak Shape and Background*, version 2.2; University of Southern Denmark: Odense, Denmark, 2002; http://www.quases.com.
(20) Cai, J.; Wang, Y.; Zhu, Y.; Wu, M.; Zhang, H.; Li, X.; Jiang, Z.; Meng, M. In Situ Formation of Disorder-Engineered TiO_2(B)-Anatase Heterophase Junction for Enhanced Photocatalytic Hydrogen Evolution. *ACS Appl. Mater. Interfaces* **2015**, *7*, 24987−24992.
(21) Iancu, A. T.; Logar, M.; Park, J.; Prinz, F. B. Atomic Layer Deposition of Undoped TiO_2 Exhibiting p-Type Conductivity. *ACS Appl. Mater. Interfaces* **2015**, *7*, 5134−5140.
(22) Lichterman, M. F.; Hu, S.; Richter, M. H.; Crumlin, E. J.; Axnanda, S.; Favaro, M.; Drisdell, W.; Hussain, Z.; Mayer, T.; Brunschwig, B. S.; Lewis, N. S.; Liu, Z.; Lewerenz, H.-J. Direct Observation of the Energetics at a Semiconductor/Liquid Junction by Operando X-ray Photoelectron Spectroscopy. *Energy Environ. Sci.* **2015**, *8*, 2409−2416.
(23) McDowell, M. T.; Lichterman, M. F.; Carim, A. I.; Liu, R.; Hu, S.; Brunschwig, B. S.; Lewis, N. S. The Influence of Structure and Processing on the Behavior of TiO_2 Protective Layers for Stabilization of n-Si/TiO_2/Ni Photoanodes for Water Oxidation. *ACS Appl. Mater. Interfaces* **2015**, *7*, 15189−15199.
(24) Fan, C.; Chen, C.; Wang, J.; Fu, X.; Ren, Z.; Qian, G.; Wang, Z. Black Hydroxylated Titanium Dioxide Prepared via Ultrasonication with Enhanced Photocatalytic Activity. *Sci. Rep.* **2015**, *5*, 11712.
(25) Wang, Y.; Feng, C.; Zhang, M.; Yang, J.; Zhang, Z. Enhanced visible light photocatalytic activity of N-doped TiO_2 in relation to single-electron-trapped oxygen vacancy and doped-nitrogen. *Appl. Catal., B* **2010**, *100*, 84−90.
(26) Zhang, L.; Tse, M. S.; Tan, O. K.; Wang, Y. X.; Han, M. Facile fabrication and characterization of multi-type carbon-doped TiO_2 for visible light-activated photocatalytic mineralization of gaseous toluene. *J. Mater. Chem. A* **2013**, *1*, 4497−4507.
(27) Kuznetsov, M.; Zhuravlev, J.; Zhilyaev, V.; Gubanov, V. XPS study of the nitrides, oxides and oxynitrides of titanium. *J. Electron Spectrosc. Relat. Phenom.* **1992**, *58*, 1−9.
(28) Zhang, Y.; Li, X.; Chen, D.; Ma, N.; Hua, X.; Wang, H. Si Doping Effects on the Photocatalytic Activity of TiO_2 Nanotubes Film Prepared by an Anodization Process. *Scr. Mater.* **2009**, *60*, 543−546.
(29) Henderson, M. A. A Surface Perspective on Self-Diffusion in Rutile TiO_2. *Surf. Sci.* **1999**, *419*, 174−187.
(30) Diebold, U. The Surface Science of Titanium Dioxide. *Surf. Sci. Rep.* **2003**, *48*, 53−229.
(31) Park, K. T.; Pan, M.; Meunier, V.; Plummer, E. W. Reoxidation of TiO_2(110) via Ti Interstitials and Line Defects. *Phys. Rev. B: Condens. Matter Mater. Phys.* **2007**, *75*, 245415.
(32) Perkins, C. L.; Henderson, M. A. Photodesorption and Trapping of Molecular Oxygen at the TiO_2(110)-Water Ice Interface. *J. Phys. Chem. B* **2001**, *105*, 3856−3863.
(33) Pfeifer, V.; et al. The Electronic Structure of Iridium Oxide Electrodes Active in Water Splitting. *Phys. Chem. Chem. Phys.* **2016**, *18*, 2292−2296.
(34) Pfeifer, V.; et al. The Electronic Structure of Iridium and Its Oxides. *Surf. Interface Anal.* **2016**, *48*, 261−273.
(35) Pfeifer, V.; Jones, T. E.; Wrabetz, S.; Massué, C.; Velasco Vélez, J. J.; Arrigo, R.; Scherzer, M.; Piccinin, S.; Hävecker, M.; Knop-Gericke, A.; Schlögl, R. Reactive Oxygen Species in Iridium-Based OER Catalysts. *Chem. Sci.* **2016**, *7*, 6791−6795.
(36) Tuan, A.; Yoon, M.; Medvedev, V.; Ono, Y.; Ma, Y.; Rogers, J., Jr. Interface Control in the Chemical Vapor Deposition of Titanium Dioxide on Silicon(100). *Thin Solid Films* **2000**, *377*−*378*, 766−771.
(37) Fleming, L.; Fulton, C. C.; Lucovsky, G.; Rowe, J. E.; Ulrich, M. D.; Lüning, J. Local Bonding Analysis of the Valence and Conduction Band Features of TiO_2. *J. Appl. Phys.* **2007**, *102*, 033707.
(38) Pandiyan, R.; Delegan, N.; Dirany, A.; Drogui, P.; el Khakani, M. A. Probing the Electronic Surface Properties and Bandgap Narrowing of in situ N, W, and (W,N) Doped Magnetron-Sputtered TiO_2 Films Intended for Electro-Photocatalytic Applications. *J. Phys. Chem. C* **2016**, *120*, 631−638.
(39) Sanjinés, R.; Tang, H.; Berger, H.; Gozzo, F.; Margaritondo, G.; Lévy, F. Electronic Structure of Anatase TiO_2 Oxide. *J. Appl. Phys.* **1994**, *75*, 2945−2951.
(40) Fulton, C. C.; Lucovsky, G.; Nemanich, R. J. Electronic States at the Interface of Ti-Si Oxide on Si(100). *J. Vac. Sci. Technol., B: Microelectron. Process. Phenom.* **2002**, *20*, 1726−1731.
(41) Yaghoubi, H.; Li, Z.; Chen, Y.; Ngo, H. T.; Bhethanabotla, V. R.; Joseph, B.; Ma, S.; Schlaf, R.; Takshi, A. Toward a Visible Light-Driven Photocatalyst: The Effect of Midgap-States-Induced Energy Gap of Undoped TiO_2 Nanoparticles. *ACS Catal.* **2015**, *5*, 327−335.
(42) Perego, M.; Seguini, G.; Scarel, G.; Fanciulli, M.; Wallrapp, F. Energy Band Alignment at TiO_2/Si Interface with Various Interlayers. *J. Appl. Phys.* **2008**, *103*, 043509.
(43) Chen, X.; Burda, C. The Electronic Origin of the Visible-Light Absorption Properties of C-, N- and S-Doped TiO_2 Nanomaterials. *J. Am. Chem. Soc.* **2008**, *130*, 5018−5019.
(44) Xia, X.; Lu, L.; Walton, A.; Ward, M.; Han, X.; Brydson, R.; Luo, J.; Shao, G. Origin of Significant Visible-Light Absorption Properties of Mn-Doped TiO_2 Thin Films. *Acta Mater.* **2012**, *60*, 1974−1985.
(45) Asahi, R.; Morikawa, T.; Ohwaki, T.; Aoki, K.; Taga, Y. Visible-Light Photocatalysis in Nitrogen-Doped Titanium Oxides. *Science* **2001**, *293*, 269−271.
(46) Wang, G.; Wang, H.; Ling, Y.; Tang, Y.; Yang, X.; Fitzmorris, R. C.; Wang, C.; Zhang, J. Z.; Li, Y. Hydrogen-Treated TiO_2 Nanowire Arrays for Photoelectrochemical Water Splitting. *Nano Lett.* **2011**, *11*, 3026−3033.
(47) Kibria, M. G.; Zhao, S.; Chowdhury, F. A.; Wang, Q.; Nguyen, H. P. T.; Trudeau, M. L.; Guo, H.; Mi, Z. Tuning the Surface Fermi Level on p-Type Gallium Nitride Nanowires for Efficient Overall Water Splitting. *Nat. Commun.* **2014**, *5*, 3825.

DOI: 10.1021/acs.chemmater.7b02938
Chem. Mater. 2018, 30, 1199−1208

Paper II

Diversity of TiO_2: Controlling the molecular and electronic structure of atomic-layer-deposited black TiO_2

Harri Ali-Löytty, Markku Hannula, Jesse Saari, Lauri Palmolahti, Bela Bhuskute, Riina Ulkuniemi, Tuomo Nyyssönen, Kimmo Lahtonen, and Mika Valden

ACS Applied Materials and Interfaces, 11, p. 2758–2762, 2019
DOI: 10.1021/acsami.8b20608.

ACS APPLIED MATERIALS & INTERFACES

Letter

Cite This: ACS Appl. Mater. Interfaces 2019, 11, 2758−2762

www.acsami.org

Diversity of TiO_2: Controlling the Molecular and Electronic Structure of Atomic-Layer-Deposited Black TiO_2

Harri Ali-Löytty,*[†] Markku Hannula,[†] Jesse Saari,[†] Lauri Palmolahti,[†] Bela D. Bhuskute,[†] Riina Ulkuniemi,[†] Tuomo Nyyssönen,[‡] Kimmo Lahtonen,[†] and Mika Valden[†]

[†]Surface Science Group, Laboratory of Photonics, and [‡]Metals Technology Group, Laboratory of Materials Science, Tampere University of Technology, Tampere FI-33101, Finland

Supporting Information

ABSTRACT: Visually black, electrically leaky, amorphous titania (am-TiO_2) thin films were grown by atomic layer deposition (ALD) for photocatalytic applications. Broad spectral absorbance in the visible range and exceptional conductivity are attributed to trapped Ti^{3+} in the film. Oxidation of Ti^{3+} upon heat treatment leads to a drop in conductivity, a color change from black to white, and crystallization of am-TiO_2. ALD-grown black TiO_2, without any heat treatment, is subject to dissolution in alkaline photoelectrochemical conditions. The best photocatalytic activity for solar water splitting is obtained for completely crystalline white TiO_2.

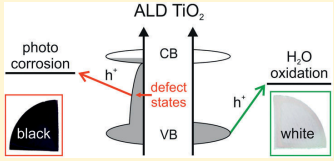

KEYWORDS: *atomic layer deposition, titanium dioxide, oxide defects, crystallization, protecting overlayers, photocatalysis, water splitting*

Black titania (TiO_2) is a promising material for providing increased photocatalytic efficiency due to its pronounced solar absorption compared to conventional white or transparent, nonconductive TiO_2 with large bandgap (3.0−3.2 eV) which is capable of absorbing light only in the UV range.[1] Black TiO_2 is often synthesized from white TiO_2 via treatment in a reductive H_2 atmosphere that introduces disorder via oxide defects or H dopants into the TiO_2 structure.[1−4] On the other hand, transparent amorphous TiO_2 (am-TiO_2) thin film grown by atomic layer deposition (ALD) has shown exceptional charge transfer properties and is therefore utilized as a protection layer for unstable semiconductor materials in photoelectrochemical (PEC) applications.[5] However, the stability of ALD grown am-TiO_2 under PEC conditions has remained controversial, since most studies have involved an additional catalyst overlayer on am-TiO_2.[6] Recent work by Yu et al.[7] revealed a metastable intermediate within an ALD grown am-TiO_2 thin film on Si photoanode that induced corrosion, despite the additional Ni overlayer. We have shown that bare ALD grown am-TiO_2 is subject to rapid photocorrosion under PEC conditions.[8] Even crystalline TiO_2 that is believed to be extremely stable, has been shown to suffer from photohole induced corrosion under PEC conditions.[9] There is an urgent need for better understanding of the TiO_2 corrosion mechanism to be able to develop TiO_2-based materials for photocatalytic energy conversion devices. Here we report a direct synthesis of black TiO_2 by ALD and address the question of inherent stability of ALD-grown electrically leaky titania.

ALD of TiO_2 was carried out at 200 °C in a commercial ALD reactor using tetrakis(dimethylamido)titanium(IV) (TDMAT) and water as precursors and Ar as carrier/purge/venting gas.[8] N-type Si(100) wafer was used as a substrate with the exceptions of optical and electrical measurements for which a transparent quartz (SiO_2) glass was used as a substrate. The TiO_2 film thickness of 30 nm was optimized in terms of PEC efficiency for water oxidation, and thus chosen for detailed analysis.

Figure 1 shows the UV−vis absorption results of ALD TiO_2 after deposition and after annealing in oxidizing (air) and reducing (UHV) conditions. The oxidized sample depicts characteristic absorption behavior of rutile TiO_2 with absorption edge at 387 nm (3.2 eV) and no absorption in the visible range. In contrast, the absorption edge for the as-deposited TiO_2 was observed at 344 nm (3.6 eV), which is strongly blue-shifted from the absorption edge of rutile TiO_2 and the absorption edge is followed by a broad absorption that gives rise to the black color of the TiO_2 film.

The increased absorption below the band gap energy is characteristic to free charge carrier absorption or absorption due to intraband gap states. The broad absorption of the as-deposited sample following approximately a logarithmic trend from 350 to 800 nm suggests trapped charge carriers within the band gap, which are assigned later to Ti^{3+}.[10] This is supported by the blue-shift in absorption edge compared to rutile TiO_2 which we interpret as the Moss−Burstein effect[11] due to the excess population of the conduction band. Interestingly, annealing under reductive conditions induced a clear decrease in the absorption at 528 nm that corresponds to the absorption of trapped holes in TiO_2.[12] Recently, we showed that the same

Received: November 23, 2018
Accepted: January 4, 2019
Published: January 4, 2019

DOI: 10.1021/acsami.8b20608
ACS Appl. Mater. Interfaces 2019, 11, 2758−2762

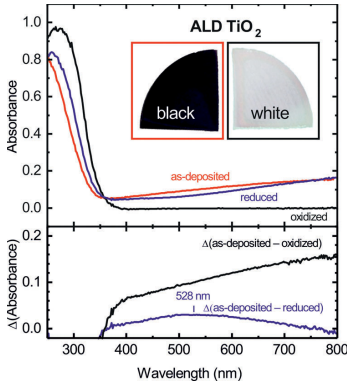

Figure 1. Absorbance of a 30 nm thick black TiO_2 film measured after ALD growth (as-deposited), after annealing in air at 500 °C (oxidized) and after annealing in ultrahigh vacuum (UHV) at 600 °C (reduced). The inset shows pictures of 200 nm thick TiO_2 films after deposition (black) and after annealing in air at 500 °C (white). The difference spectra in the bottom presents the change in absorbance induced by the heat treatments.

reductive heat treatment improved the stability of black am-TiO_2 under PEC conditions, which was attributed to the formation of O^- species via electron transfer from O to Ti.[8] The clear change in optical absorption suggests that the electron transfer is accompanied by the recombination of trapped holes.

Oxidation induced changes on the charge carrier distribution were studied in terms of electrical conductivity and optical absorption as shown in Figure 2. The oxidation treatment was carried out under ambient air by placing the sample into a preheated tube furnace for 45 min. In addition to the aforementioned broad absorbance in the Vis range and enlarged bandgap (Figure 2b, Figure S1) black TiO_2 exhibits exceptionally high conductivity of 150 S/m (Figure 2a). A slight change in the properties was observed upon oxidation at 200 °C followed by more dramatic change for increasing temperatures.

The slight change in the TiO_2 film properties after oxidation at 200 °C is reasonable since the ALD growth was performed at the same temperature. The drastic changes in the electrical and optical properties correlate perfectly with each other and can be explained by the oxidation of the trapped charge carriers that are responsible for the enhanced conductivity and absorption in the Vis range.

Figure 3 shows scanning electron microscope (SEM) images and grazing-incidence X-ray diffraction (GIXRD) patterns for the oxidized samples. The as-deposited black TiO_2 was found to be amorphous followed by gradual crystallization upon oxidation. In addition to rutile, the crystallized films were found to contain some brookite TiO_2, and quite surprisingly, after oxidation at 350 °C a strong anatase peak appeared. X-ray photoelectron spectroscopy (XPS) reveals that nitrogen (1.8 at. %) is segregated onto the surface at 350 °C that coincides with the formation of the anatase phase (Figure 3c inset). This implies that the small ALD residue concentration of nitrogen plays an important role in the phase stabilization of TiO_2 under these oxidative annealing conditions, although complete crystallization into the most stable rutile TiO_2 via less stable anatase TiO_2 is often observed in the annealing treatments of TiO_2.[13] Furthermore, the nitrogen concentration within the black am-TiO_2 structure is most likely contributing to the broad absorption in a range of 500−900 nm shown in Figure 1 by providing nitrogen induced in-gap states.

SEM images (Figure 3a) reveal that crystallization initiates at 250 °C, which is not yet clear from the GIXRD (Figure 3b). Most importantly, crystallization was found to follow the oxidation of the trapped charge carriers.

The influence of oxidation on the molecular and valence band structure of black TiO_2 was studied with XPS and ultraviolet photoelectron spectroscopy (UPS), respectively. Figure 4 shows photoelectron spectra by comparing the as-deposited and 500 °C oxidized samples. It is evident from the XP survey spectra that the surfaces of ALD grown TiO_2 films are clean with a small concentration of carbon, which is mainly due to impurities from the air exposure, and <0.3 at. % of nitrogen (Figure 4a). The Ti 2p XPS transitions appear as peaks in the binding energy range of 450−480 eV (Figure 4c). The main Ti $2p_{3/2}$ and Ti $2p_{1/2}$ peaks at binding energies of 458.8 and 464.5 eV, respectively, are accompanied by well-known charge transfer shakeup satellite peaks 13 eV above the main peaks.[14] These binding energies and satellite peaks are consistent with the Ti^{4+} state of the TiO_2. In addition, a clear shoulder at the binding energy of 457.5 eV can be seen in the XP spectrum measured from the as-deposited sample. This peak can be assigned to the Ti^{3+}, which can explain the increased absorption in the Vis range[15] and increased conductivity.

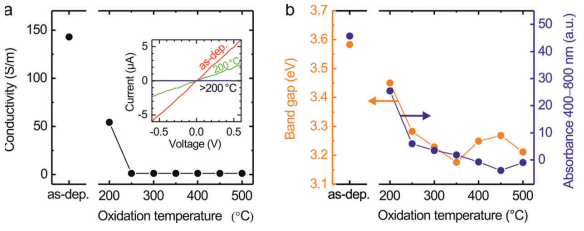

Figure 2. (a) Conductivity and (b) optical band gap and integrated absorbance from 400 to 800 nm for the ALD grown black TiO_2 films after they have been annealed at different oxidation temperatures. Inset in a shows the dramatic change of the $I-V$ characteristics for the as-deposited TiO_2 film and the TiO_2 films after oxidation treatment at 200 °C and higher temperatures.

DOI: 10.1021/acsami.8b20608
ACS Appl. Mater. Interfaces 2019, 11, 2758−2762

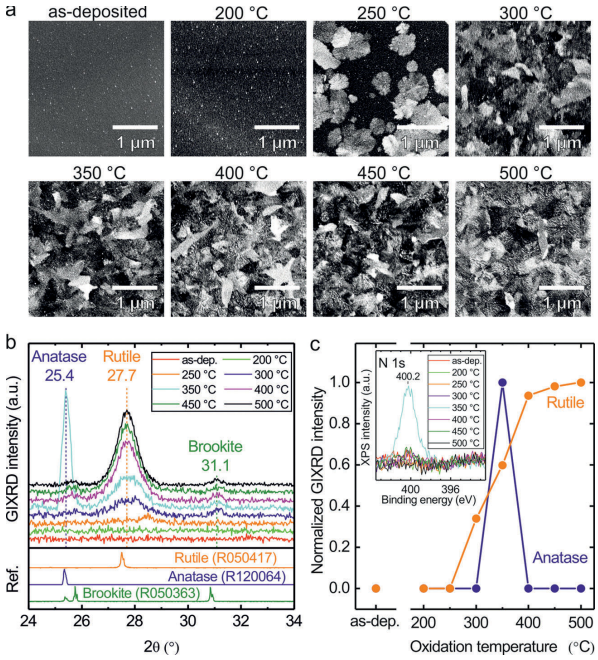

Figure 3. (a) SEM images, (b) GIXRD patterns, and (c) normalized GIXRD intensities of the anatase and rutile peaks for the ALD-grown black TiO_2 films at different oxidation temperatures. Inset in c shows XP spectra of N 1s.

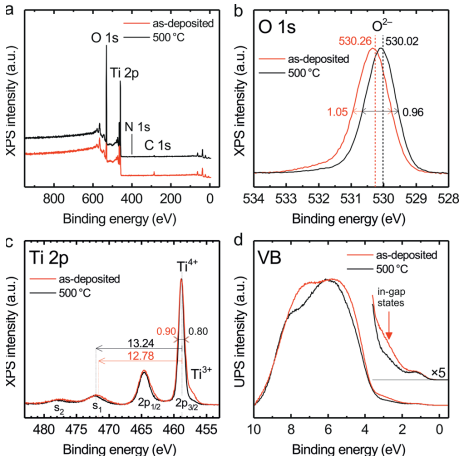

Figure 4. XP (a) survey spectra, (b) O 1s, (c) Ti 2p, and (d) UPS spectra of the valence band (VB) for the ALD-grown black TiO_2 film and 500 °C oxidized film.

The O 1s XPS peak is centered at 530 eV as expected for O^{2-} anions of the TiO_2 structure[16] and the peak is slightly shifted to a lower binding energy upon oxidation (Figure 4b). This 0.2 eV shift and the decrease in the full width at half-maximum (fwhm) of the O 1s and Ti 2p XPS peaks take place gradually with increasing oxidation temperature (Figure S2) and are a result of the ordering of the amorphous phase to the crystalline rutile phase of TiO_2. We note that no such gradual change in neither Ti^{3+} concentration or in O/Ti ratio with temperature was observed (Figure S2a). The majority of Ti^{3+} was oxidized already at 200 °C and the O/Ti ratio was close to 2 throughout the temperature range.

The shakeup satellite peak originates from the excitation of a valence electron to a previously unoccupied state by the outgoing Ti 2p photoelectron according to the sudden approximation of photoemission.[17] Thus, any change in the valence band structure, i.e. Ti−O bonding, may reflect to the charge transfer energy. Indeed, the UPS spectrum of the as-deposited sample (Figure 4d) reveals in-gap states at 2.5 eV that are efficiently removed upon oxidation treatments. Following the removal of in-gap states, the Ti $2p_{3/2}$ shakeup separation energy was observed to increase with oxidation temperature. The changes in the Ti−O bonding are also evident from the changes in the O 1s binding energy as pointed out above. Therefore, the in-gap states can be assigned to the lattice disorder[18] and the subtle deviations in electronic structure compared to crystalline rutile TiO_2 presented above characterize the unique electronic structure of amorphous

DOI: 10.1021/acsami.8b20608
ACS Appl. Mater. Interfaces 2019, 11, 2758−2762

ALD TiO_2. We note that the careful monitoring of the oxidation-treatment-induced changes in the electronic structure allowed the distinction between the doping,[19] $Ti^{2+/3+}$ defects,[8] oxygen vacancies,[20] and the lattice-disorder-induced in-gap states.

The influence of oxidation on the performance of initially black TiO_2 as a photocatalyst for H_2O oxidation was studied as shown in Figure 5 and Figure S3. In accordance with our

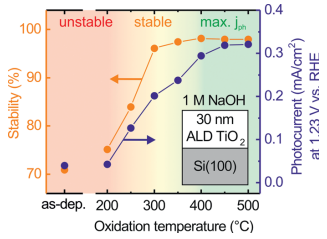

Figure 5. Photoelectrochemical stability and photocurrent (in 1 M NaOH) of the ALD grown, initially black, TiO_2 film after oxidation in temperature range from 200 to 500 °C.

previous work,[8] the as-deposited black TiO_2 exhibits PEC instability and negligible photocurrent at 1.23 V vs RHE in 1 M NaOH. Only slight change in the PEC stability was observed upon oxidation at 200 °C followed by more dramatic change for increasing temperatures. Therefore, the oxidation of trapped charge carriers at 200 °C does not alone provide an explanation for the PEC stability nor for the increase in photocurrent with oxidation temperature. A reasonable stability is obtained after oxidation at 300 °C and above, whereas photocurrent continues to increase reaching saturation value for samples oxidized at >400 °C. The photocurrent was found to improve with the degree of TiO_2 crystallization and reach saturation for crystallized rutile TiO_2.

The improvement in PEC stability was found to correlate with crystallization, which supports earlier results that the stability of crystalline TiO_2 outperforms the amorphous phase.[21] Albeit the complete crystallization of TiO_2 thin film required oxidation at >400 °C, the SEM images (Figure 3a) show that the surface is mostly crystallized already at 300 °C. Thus, the crystallized surface alone is sufficient requirement to endow improved PEC stability to the TiO_2 thin film. Although am-TiO_2 has been shown to both experimentally and theoretically exhibit several orders of magnitude higher dissolution rates in 1 M NaOH than crystalline polymorphs,[22] we emphasize that the stability of black am-TiO_2 can also be improved by controlling the defect distribution.[8]

The unique properties of disordered ALD-TiO_2 include controlling the Ti^{3+} self-doping via growth temperature and thermal modification of defect and crystal structure. Recently we showed that annealing in UHV results in increase in Ti^{3+} states in the film and promotes PEC stability via the formation of O^-.[8] The facile modification treatments manifest the diversity of ALD-TiO_2 in applications ranging from conductive interlayers, to electrically leaky protection layers and photocatalyst materials.

In the present study, we have shown that black TiO_2 with enhanced absorbance in the wavelength range of 400–800 nm can be deposited as a conformal amorphous thin film using ALD. We have demonstrated that the physicochemical properties of TiO_2 can be controlled by postannealing treatments either in reductive or oxidative conditions. The black as-deposited TiO_2 shows exceptionally high electrical conductivity of 150 S/m, but suffers from poor PEC stability and dissolves in alkaline conditions. Annealing treatment in extremely reductive conditions (UHV) at 500 °C transforms the black as-deposited TiO_2 into a photoelectrochemically stable phase of black TiO_2 retaining its amorphous structure.[8] On the other hand, oxidation in air at 500 °C crystallizes TiO_2 into rutile phase with the maximum efficiency as photocatalyst for photoelectrochemical H_2O oxidation. The unprecedented diversity of ALD-TiO_2 can be rationalized by the propensity of the molecular structure toward local changes in the bonding configuration that affects the charge carrier densities via modified electronic structure. This unfolds the tremendous optoelectronic properties of TiO_2.

■ ASSOCIATED CONTENT

Supporting Information

The Supporting Information is available free of charge on the ACS Publications website at DOI: 10.1021/acsami.8b20608.

UV–vis absorption, XPS, PEC data as a function of oxidation temperature, and experimental details (PDF)

■ AUTHOR INFORMATION

Corresponding Author

*Email: Harri.Ali-Loytty@tut.fi.

ORCID

Harri Ali-Löytty: 0000-0001-8746-7268
Markku Hannula: 0000-0003-1110-7439
Kimmo Lahtonen: 0000-0002-8138-7918

Present Address

Surface Science Group, Laboratory of Photonics, Tampere University of Technology, P.O. Box 692, FI-33101 Tampere, Finland

Notes

The authors declare no competing financial interest.

■ ACKNOWLEDGMENTS

This work was supported by the Academy of Finland (decision numbers 141481, 286713 and 309920). H.A. and B.D.B. were supported by the Jenny and Antti Wihuri Foundation. M.H. was supported by the TUT's Graduate School and Emil Aaltonen Foundation.

■ REFERENCES

(1) Liu, X.; Zhu, G.; Wang, X.; Yuan, X.; Lin, T.; Huang, F. Progress in Black Titania: A New Material for Advanced Photocatalysis. *Adv. Energy Mater.* **2016**, *6* (17), 1385–1388.

(2) Selcuk, S.; Zhao, X.; Selloni, A. Structural Evolution of Titanium Dioxide during Reduction in High-Pressure Hydrogen. *Nat. Mater.* **2018**, *17* (10), 923–928.

(3) Wang, B.; Shen, S.; Mao, S. S. Black TiO_2 for Solar Hydrogen Conversion. *J. Materiomics* **2017**, *3* (2), 96–111.

(4) Yan, X.; Li, Y.; Xia, T. Black Titanium Dioxide Nanomaterials in Photocatalysis. *Int. J. Photoenergy* **2017**, *2017*, No. 8529851.

(5) Hu, S.; Shaner, M. R.; Beardslee, J. A.; Lichterman, M.; Brunschwig, B. S.; Lewis, N. S. Amorphous TiO_2 Coatings Stabilize Si, GaAs, and GaP Photoanodes for Efficient Water Oxidation. *Science* **2014**, *344* (6187), 1005–1009.

DOI: 10.1021/acsami.8b20608
ACS Appl. Mater. Interfaces 2019, 11, 2758–2762

(6) Sivula, K. Defects Give New Life to an Old Material: Electronically Leaky Titania as a Photoanode Protection Layer. *ChemCatChem* **2014**, *6* (10), 2796−2797.
(7) Yu, Y.; Sun, C.; Yin, X.; Li, J.; Cao, S.; Zhang, C.; Voyles, P. M.; Wang, X. Metastable Intermediates in Amorphous Titanium Oxide: A Hidden Role Leading to Ultra-Stable Photoanode Protection. *Nano Lett.* **2018**, *18* (8), 5335−5342.
(8) Hannula, M.; Ali-Löytty, H.; Lahtonen, K.; Sarlin, E.; Saari, J.; Valden, M. Improved Stability of ALD Grown Amorphous TiO_2 Photoelectrode Coatings by Thermally Induced Oxygen Defects. *Chem. Mater.* **2018**, *30* (4), 1199−1208.
(9) Yang, Y.; Ling, Y.; Wang, G.; Liu, T.; Wang, F.; Zhai, T.; Tong, Y.; Li, Y. Photohole Induced Corrosion of Titanium Dioxide: Mechanism and Solutions. *Nano Lett.* **2015**, *15* (10), 7051−7057.
(10) Di Valentin, C.; Pacchioni, G.; Selloni, A. Reduced and N-Type Doped TiO_2: Nature of Ti^{3+} Species. *J. Phys. Chem. C* **2009**, *113* (48), 20543−20552.
(11) Burstein, E. Anomalous Optical Absorption Limit in InSb. *Phys. Rev.* **1954**, *93* (3), 632−633.
(12) Yoshihara, T.; Katoh, R.; Furube, A.; Tamaki, Y.; Murai, M.; Hara, K.; Murata, S.; Arakawa, H.; Tachiya, M. Identification of Reactive Species in Photoexcited Nanocrystalline TiO_2 Films by Wide-Wavelength-Range (400−2500 Nm) Transient Absorption Spectroscopy. *J. Phys. Chem. B* **2004**, *108* (12), 3817−3823.
(13) Hanaor, D. A. H.; Sorrell, C. C. Review of the Anatase to Rutile Phase Transformation. *J. Mater. Sci.* **2011**, *46* (4), 855−874.
(14) Woicik, J. C.; Weiland, C.; Rumaiz, A. K. Loss for Photoemission versus Gain for Auger: Direct Experimental Evidence of Crystal-Field Splitting and Charge Transfer in Photoelectron Spectroscopy. *Phys. Rev. B: Condens. Matter Mater. Phys.* **2015**, *91* (20), 201412.
(15) Zuo, F.; Wang, L.; Wu, T.; Zhang, Z.; Borchardt, D.; Feng, P. Self-Doped Ti^{3+} Enhanced Photocatalyst for Hydrogen Production under Visible Light. *J. Am. Chem. Soc.* **2010**, *132* (34), 11856−11857.
(16) Naumkin, A. V.; Kraut-Vass, A.; J, C. P. *NIST XPS Database 20*, Version 4.0; National Institute of Standards and Technology, 2008.
(17) Hedin, L.; Lee, J. D. Sudden Approximation in Photoemission and Beyond. *J. Electron Spectrosc. Relat. Phenom.* **2002**, *124* (2), 289−315.
(18) Chen, X.; Liu, L.; Yu, P. Y.; Mao, S. S. Increasing Solar Absorption for Photocatalysis with Black Hydrogenated Titanium Dioxide Nanocrystals. *Science* **2011**, *331* (6018), 746−750.
(19) Asahi, R.; Morikawa, T.; Ohwaki, T.; Aoki, K.; Taga, Y. Visible-Light Photocatalysis in Nitrogen-Doped Titanium Oxides. *Science* **2001**, *293* (5528), 269−271.
(20) Guo, Z.; Ambrosio, F.; Pasquarello, A. Hole Diffusion across Leaky Amorphous TiO_2 Coating Layers for Catalytic Water Splitting at Photoanodes. *J. Mater. Chem. A* **2018**, *6* (25), 11804−11810.
(21) Ros, C.; Andreu, T.; Hernández-Alonso, M. D.; Penelas-Pérez, G.; Arbiol, J.; Morante, J. R. Charge Transfer Characterization of ALD-Grown TiO2 Protective Layers in Silicon Photocathodes. *ACS Appl. Mater. Interfaces* **2017**, *9* (21), 17932−17941.
(22) Shkol'nikov, E. V. Thermodynamics of the Dissolution of Amorphous and Polymorphic TiO_2 Modifications in Acid and Alkaline Media. *Russ. J. Phys. Chem. A* **2016**, *90* (3), 567−571.

DOI: 10.1021/acsami.8b20608
ACS Appl. Mater. Interfaces 2019, 11, 2758−2762

Paper III

Fabrication of topographically microstructured titanium silicide interface for advanced photonic applications

Markku Hannula, Kimmo Lahtonen, Harri Ali-Löytty, Alexei A. Zakharov, Tero Isotalo, Jesse Saari, and Mika Valden

Scripta Materialia, 119, p. 76–81, 2016.
DOI: 10.1016/j.scriptamat.2016.03.016.

Scripta Materialia 119 (2016) 76–81

Contents lists available at ScienceDirect

Scripta Materialia

journal homepage: www.elsevier.com/locate/scriptamat

Regular Article

Fabrication of topographically microstructured titanium silicide interface for advanced photonic applications

M. Hannula [a], K. Lahtonen [a], H. Ali-Löytty [a], A.A. Zakharov [b], T. Isotalo [a], J. Saari [a], M. Valden [a,*]

[a] Surface Science Laboratory, Optoelectronics Research Centre, Tampere University of Technology, P.O. Box 692, FI-33101 Tampere, Finland
[b] MAX IV Laboratory, Lund University, P.O. Box 118, SE-22100 Lund, Sweden

ARTICLE INFO

Article history:
Received 4 February 2016
Accepted 15 March 2016
Available online 17 April 2016

Keywords:
Atomic layer deposition (ALD)
X-ray photoelectron spectroscopy (XPS)
Transition metal silicides
Semiconductors
Surface modification

ABSTRACT

We present a widely scalable, high temperature post-growth annealing method for converting ultra-thin films of TiO_2 grown by atomic layer deposition to topographically microstructured titanium silicide (TiSi). The photoemission electron microscopy results reveal that the transformation from TiO_2 to TiSi at 950 °C proceeds via island formation. Inside the islands, TiO_2 reduction and Si diffusion play important roles in the formation of the highly topographically microstructured TiSi interface with laterally nonuniform barrier height contact. This is advantageous for efficient charge transfer in Si-based heterostructures for photovoltaic and photoelectrochemical applications.

III

Titanium silicide (TiSi) nanostructures have been widely used in nano- and microelectronics as ohmic contacts and interconnect materials [1] and, in recent years, photoelectrochemical (PEC) devices developed for water splitting [2–4]. TiSi has an exceptionally broad band-gap from 1.5 eV to 3.4 eV that is alone large enough to allow photocatalytical splitting of water [4]. The efficiency of a PEC device can be increased by interfacing a semiconductor material with an electrocatalyst (EC). Key parameters in the optimization of PEC materials for water splitting are the electronic band positions with respect to water redox potentials. Under electrolyte contact, the Fermi levels of a photoelectrode and electrolyte redox species align via charge transfer resulting in band bending within the semiconductor photoelectrode. If an EC covers a semiconductor substrate completely, the electronic band alignment is determined by the EC. In contrast, if the EC layer is discontinuous, the band alignment can behave like the semiconductor but the surface has the catalytic activity of the EC. Based on the "pinch-off" theory this behavior is valid for catalyst particles with dimensions smaller than the depletion width of the semiconductor [5]. The depletion width is strongly affected by the degree of free charge carriers, and is in the range of few micrometers for a lightly doped Si [6].

Here we demonstrate a simple atomic layer deposition (ALD) and thermal annealing based method for fabricating a topographically microstructured discontinuous TiSi surface on Si substrate. This allows for energy band engineering of photoelectrodes via exploitation of the pinch-off effect. Hill et al. recently showed that the pinch-off effect produced by cobalt silicide heterostructures grown on silicon photoanodes can significantly improve their PEC performance [7]. The ALD process described in the present study is envisaged being a generic technological approach to the fabrication of metal silicide particles (e.g. TiSi, CoSi, NiSi) on Si [1,8,9].

In this study TiSi is fabricated from ALD grown TiO_2 ultra-thin film which is extremely conformal and homogenous. The film is transformed into TiSi by post-annealing which also makes it thermally stable for subsequent film depositions. Our results reveal the initial stages of the island mediated process where the titanium dioxide ultra-thin film undergoes a transformation to suboxides and subsequently to titanium silicide. Furthermore, the laterally resolved chemical composition of the resulting microstructured TiSi surface texture is analyzed.

The phosphorus doped (resistivity 1–20 Ω cm) n-type Si(100) wafers were purchased from Wafer World, Inc. (Florida, USA). The 400 μm thick, three inch diameter pre-polished wafers had been cut in (100) orientation with ±1° accuracy. For the experiments 10 × 10 mm^2 squares were cleaved. The details of the annealing and hydrogen plasma based in situ cleaning of the silicon substrates are described in the Supplementary Material. The cleaned silicon substrates were transferred ex situ to Picosun Sunale ALD R200 Advanced reactor for titanium oxide deposition. The air exposure during the sample transfer was kept as short as possible, approximately 5 min.

ALD of titanium dioxide was carried out at a substrate temperature of 200 °C. Deposition consisted of 804 cycles of tetrakis(dimethylamido)titanium(IV) (TDMAT) and deionized water leading to a film thickness of 28.7 ± 0.3 nm as verified

* Corresponding author.
E-mail address: mika.valden@tut.fi (M. Valden).
URL: http://www.tut.fi/surfsci (M. Valden).

http://dx.doi.org/10.1016/j.scriptamat.2016.03.016
1359-6462/

by ellipsometry (see Supplementary Material). After the deposition the samples were cooled down in N_2 atmosphere before transferring them back to UHV for high temperature annealing.

Two separate UHV systems with a base pressure below 1×10^{-10} mbar were employed for annealing and subsequent electron spectroscopy experiments. X-ray photoelectron spectroscopy (XPS) and energy filtered photoemission electron microscopy (EF-PEEM) measurements were carried out using NanoESCA (Omicron NanoTechnology GmbH) spectromicroscopy system [10]. Focused monochromatized Al Kα radiation ($h\nu = 1486.5$ eV) was utilized for core level spectroscopy and imaging whereas secondary electron tail cut-off maps for work function determination were measured with non-monochromatized He Iα radiation ($h\nu = 21.22$ eV) using HIS 13 VUV Source (Focus GmbH). The XP spectra were collected using a hemispherical analyzer with energy resolution of 400 meV or 50 meV (for high resolution (HR) XPS). For EF-PEEM measurements the energy resolution of an aberration correcting double hemispherical energy analyzer (IDEA) was set to 800 meV for core level imaging and 50 meV for secondary electron imaging. Lateral resolution for core level images was approximately 500 nm and for He Iα excited secondary electron images approximately 100 nm.

High spatial resolution EF-PEEM measurements were performed with a spectroscopic photoemission and low energy electron microscope (SPELEEM) III (Elmitech GmbH) [11] at the soft X-ray beamline I311 of MAX II storage ring in the MAX IV Laboratory synchrotron radiation (SR) facility (Lund, Sweden) [12]. SPELEEM was utilized in photoelectron emission, low energy electron microscopy (LEEM) and imaging X-ray absorption (XAS) secondary electron yield modes.

In addition to XPS and EF-PEEM studies the surface morphology of the 950 °C annealed island structured sample was studied by scanning electron microscopy (SEM; Zeiss Ultra 55, Carl Zeiss Microscopy GmbH) and atomic force microscopy (AFM; Veeco Dimension 3100 AFM, Veeco Instruments Inc.).

Both NanoESCA and SPELEEM III had a heating assembly in their preparation chambers for heat treatments of the samples. For studies performed in the NanoESCA system the ALD grown TiO_2 was initially annealed at 950 °C for 10 min to form titanium silicide islands. Studying the edge areas of these islands with PEEM revealed details of the reduction process involved in the transformation of titanium (sub)oxides to titanium silicide. Subsequently the sample was annealed to 960 °C for 10 min to reduce the remaining titanium oxide areas to continuous titanium silicide ridge-like microstructure.

SEM images in Fig. 1A–C illustrate the TiSi island structure after the 950 °C annealing. Islands nucleate at seemingly random locations and with inhomogeneous size distribution. The ALD grown TiO_2 film is homogenous, and therefore it is likely that the nucleation has been initiated by small impurity particles or crystal defects in the Si substrate. It is noteworthy that the nucleation does not happen instantaneously but requires 5 min to 10 min at 950 °C temperature. Temperatures of

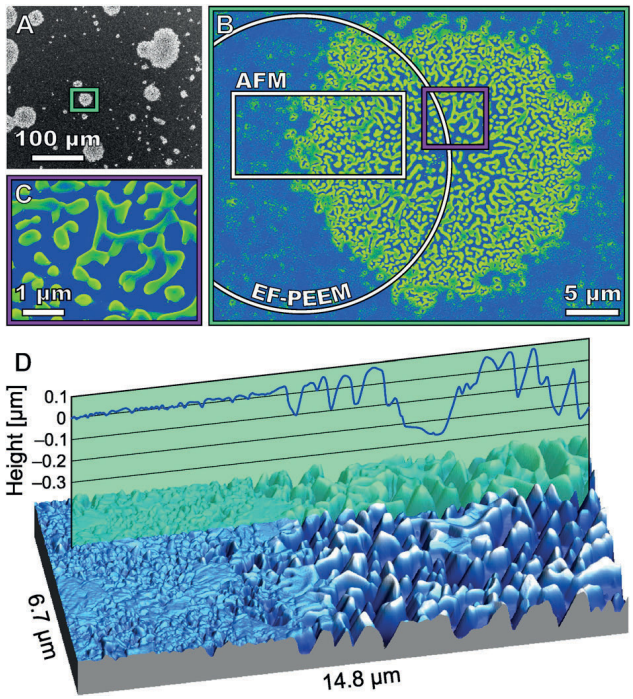

Fig. 1. A–C: SEM images of a highly topographically microstructured TiSi island after 950 °C annealing. Highest magnification in Fig. C shows the detailed TiSi ridge-like microstructure inside the island. The white circle in Fig. B shows the area selected for EF-PEEM studies and will be discussed later in detail. D: AFM image of the region framed with a white rectangle in Fig. B. AFM line profile illustrates the abrupt change in TiO_x surface topography when moving from the area outside the island (left side) to the heavily corrugated ridge-like area inside the island (right side).

920 °C and below were also tested but this only resulted in titanium suboxide formation without any indication of silicidation or evolution of island structures.

SEM images show distinct ridge-like microstructures inside the islands. Thus the true topography around a selected island was studied by AFM. Fig. 1D demonstrates that the remaining titanium (sub)oxide film outside the island has retained a smooth surface with a roughness value *Ra* of 8.0 ± 0.5 nm. However, inside the islands the roughness has increased to 79 ± 2 nm with maximum height variations of more than 300 nm which is ten times the thickness of the original TiO_2 film. Also the average height of the surface was approximately 40 nm lower in comparison with the surrounding partly reduced, but not silicidized, TiO_x surface. This suggests that the annealing process not only affects the TiO_2 film but also induces pronounced mass transfer in the silicon substrate by means of diffusion, corrugation and desorption. According to Zhao et al. [13] silicon from the substrate diffuses to titanium overlayer where it reacts with oxygen and sublimates as silicon monoxide. In our case, the titanium film has abundance of available oxygen released by the TiO_x reduction process.

An interesting detail in Fig. 1B and C is that the TiSi ridges near the center of the island, i.e. near the initial nucleation point, are small and almost spherical. When diverging from the center, the ridges became more elongated and interconnected. For both shapes the width of the structures is similar, approximately 200–300 nm. The constant width of the ridges could be explained with the shape stability of the clusters [14]. For small cluster the symmetrical compact shape is energetically favorable but as the cluster volume increases the growth proceeds preferably along the longitudinal direction thus increasing the aspect ratio.

The chemical composition of the islands was studied by XPS. Fig. 2A and B show the Ti 2p and Si 2p spectra measured inside the TiSi island and on the titanium suboxide surface between the islands. The surface between the islands is a combination of the original titanium dioxide and annealing induced suboxides. Three different oxidized states were identified corresponding to TiO_2 (458.7 eV), Ti_2O_3 (457.3 eV) and TiO (455.6 eV). Inside the islands titanium is completely reduced showing only the TiSi related component at 453.4 eV. The full width at half maximum (FWHM) of the Ti $2p_{3/2}$ spectrum inside the silicidized regions has decreased from 0.57 eV of clean Ti to 0.48 eV in TiSi which is in accordance with the observations by Tam et al. [15]. However, in contrast to their study, no chemical shift in Ti 2p between clean Ti and TiSi was observed. On the other hand, Si 2p shows a 0.42 eV shift to lower binding energy. This behavior agrees with the results from Palacio and Arranz [16] and thus consolidates the silicidation process on the islands. Also, all oxygen had desorbed from the islands.

To obtain more localized information about the chemical composition of the island structure, EF-PEEM measurements were conducted. The region of interest was selected from the left side of the island shown in Fig. 1B and images as a function of kinetic energy were recorded with a 29 μm field of view. For the analysis the image series was first energy dispersion corrected using a clean Si(100) substrate as a flat field reference (see Supplementary Material). After this the data was noise filtered using principal component analysis (PCA) with four abstract factors. Finally, the image stack was deconvoluted pixel-by-pixel to different chemical states using the components in Fig. 2A as a reference.

The chemical state resolved images of the Ti 2p transition (Fig. 3A–D) show an extremely sharp transformation interface between the titanium suboxide and silicide regions. Line profiles were extracted from the position indicated by the blue arrow in Fig. 3A. TiO_2 and Ti_2O_3 show relatively homogenous distribution when approaching the island edge. However, the TiO signal increases 4 μm before the edge. This can be interpreted to indicate that the island growth proceeds via a TiO rich rim which expands together with the island edge. In addition, no

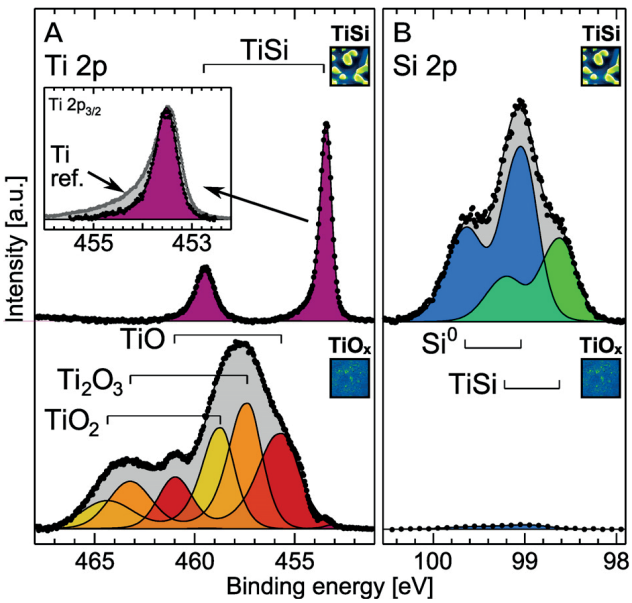

Fig. 2. Ti 2p and Si 2p XPS core level spectra of a titanium silicide island (top) and the TiO_x surface surrounding the island (bottom). The gray peak behind the Ti $2p_{3/2}$ TiSi spectrum in the inset is measured from a clean Ti reference sample thus showing that the FWHM of Ti $2p_{3/2}$ peak has decreased in titanium silicide.

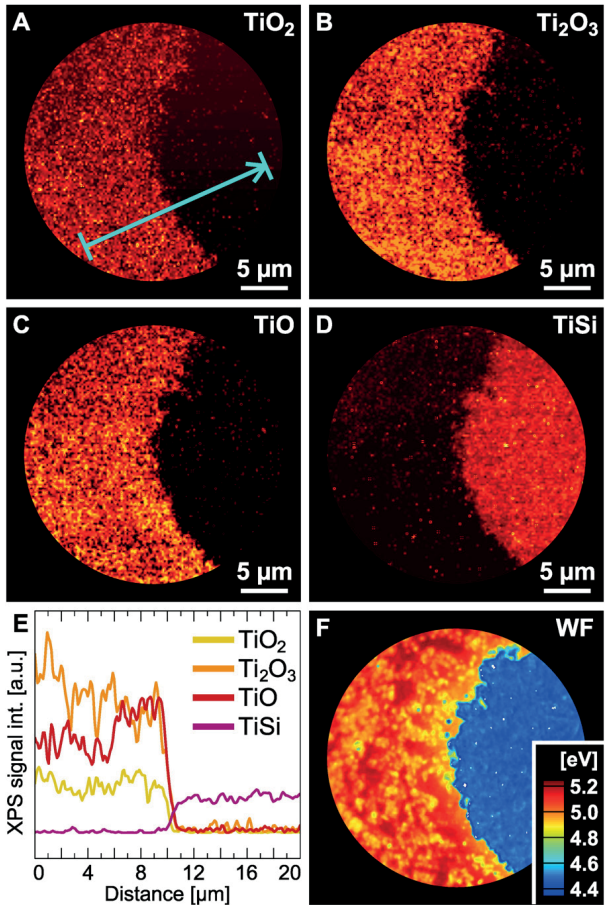

Fig. 3. A–D: Chemical state resolved EF-PEEM images of the Ti 2p. Region of interest selected from the left side of the island in Fig. 1B. E: XPS signal intensity line profiles for each titanium compound. The profile position is indicated by the blue arrow in A and the line segments at the ends of the arrow represent the line width used for averaging the signal. F: Surface electronic state resolved image (Work Function contrast).

silicon diffusion through the oxide film was observed. This is in contrast with experiments performed on metallic Ti/Si surfaces where diffusion is reported already at 400–800 °C [17–19].

The work function (WF) of the silicide island and the surrounding Ti suboxide region was determined by measuring the distance of secondary electron cut-off edge from the Fermi level. Fig. 3F shows a 0.6–0.8 eV decrease in WF inside the silicidized region. The WF inside the silicidized region is to a large extent homogeneous and corresponds to the WF of a clean Si(100) reference. In particular, the slight variation of the WF does not coincide with the TiSi particle distribution, which supports the pinch-off effect. The lowered WF value can be utilized in ohmic contacts to adjust the Schottky barrier height which is particularly important due to the efficient charge-transport properties of TiSi in nanoelectronics and solar energy harvesting applications [4].

Lateral resolution in core level imaging performed by the NanoESCA system is limited to approximately 500 nm. However, the SEM and AFM images revealed internal submicrometer scale structures inside the silicide islands. To better understand the chemistry of these structural features another TiO_2/Si sample was annealed to 960 °C and studied by SR-EF-PEEM which can achieve a lateral resolution down to 40 nm [20]. The increase in annealing temperature from 950 °C to 960 °C completed the reduction process causing the TiSi islands to coalesce into the highly topographically microstructured TiSi ridge pattern covering the whole Si substrate (Fig. 4). An SR-EF-PEEM image series of Si 2p region was recorded and deconvoluted to elemental silicon and TiSi states based on the components in Fig. 2B. For titanium a corresponding image series was recorded using XAS in secondary electron yield mode and the titanium distribution was determined from the area of the Ti L_{III} peak area

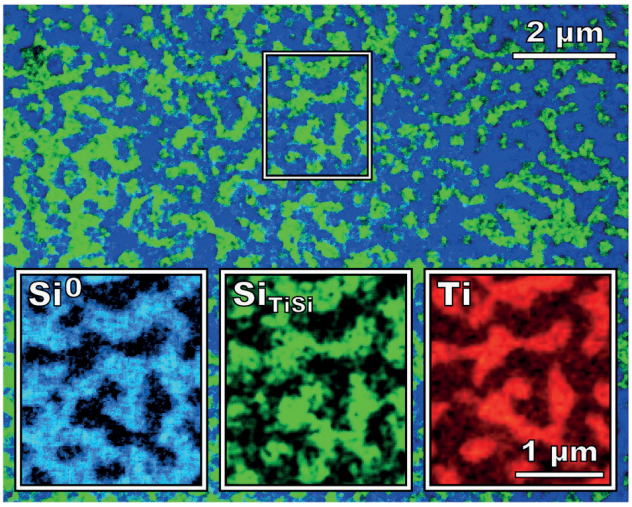

Fig. 4. SR-EF-PEEM image of the topographically microstructured TiSi ridge pattern after annealing to 960 °C. Blue and green areas correspond to elemental silicon and silicon in TiSi, respectively (see Fig. 2B for peak reference). Insets show a magnified view of both silicon chemical states together with the Ti XAS signal from the same area.

in each pixel. The insets in Fig. 4 show a clear correspondence between Si_{TiSi} and Ti. In addition, these signals originate from the areas which are observed as high ridges in SEM and AFM images. However, there is some Ti left also in the depressions (Fig. S1). This has not been identified in previous studies on metallic Ti–Si/SiO_2 systems which claim that the valleys are composed of pure silicon [21,22]. Aside from the slight difference in the initial conditions, this discrepancy could be explained by the use of XAS in secondary electron mode with decreased surface sensitivity. Thus it cannot be concluded whether the remaining titanium in the depressions is on the surface or buried deeper inside the silicon.

Low energy electron diffraction (LEED) measurement of the silicidized surface showed a 2×1 pattern typical for reconstructed Si(100). The pattern was, however, much dimmer and with a high background intensity (Fig. S2) when compared to the LEED pattern that was measured from the UHV cleaned Si(100). The 2×1 intensity maxima showed replicas which could be attributed to the lattice distortion produced by the Ti atoms in the valleys. However, the pattern did not show any new maxima which suggests that the surface structure of the TiSi ridges has no clear long range order. The same conclusion was obtained from the LEEM images (not shown) that showed the (0,0) diffraction maximum for the valley regions but not for the TiSi ridges.

The formation of the highly topographically microstructured TiSi surface phase can be explained based on the total surface and bulk energy minimization. The classical nucleation theory suggests that in most cases the surface energy increases and the bulk energy decreases with increasing cluster size. The total free energy is the sum of these two and can be reduced by the formation of larger clusters. [21] Cluster formation requires that sufficient energy is available for overcoming the nucleation barrier. According to Jeon and Nemanich [19] the nucleation barrier is higher for C54 $TiSi_2$ phase than C49 $TiSi_2$. Based on their results the ≥950 °C annealing is, however, sufficient for the formation of the thermodynamically more stable C54 $TiSi_2$ phase. This phase is also more desirable for photoelectrochemical applications, such as photoanodes used in water oxidation, due to its lower resistivity.

In order to study the chemical stability of the silicidized surface it was exposed to air (1 ATM) for 48 h. Only 28% of the silicidized titanium oxidized back to Ti^{4+} (25%) and Ti^{3+} (3%). On a clean Ti reference surface 77% of titanium became oxidized during the same oxidation treatment. This high oxidation resistance in ambient conditions can be seen as one of the key factors that make TiSi compounds so widely exploited in semiconductor industry.

In summary, we have demonstrated a widely scalable method for synthesizing a highly topographically microstructured titanium silicide texture on silicon substrates which allows for energy band engineering of Si based photoelectrodes via the exploitation of the pinch-off effect. The synthesis is based on vacuum post-annealing of ALD grown TiO_2 ultra-thin film and can thus be implemented inside one processing chamber. This makes the TiSi fabrication feasible in production chains that include several consecutive conformal coatings used in e.g. surface protection, passivation or formation of catalytically active surface/interface layer. The presented synthesis route opens up the possibility for new state-of-the-art interface engineering for photoelectrochemical devices and nano- and microelectronics.

The authors acknowledge the TUT's Graduate School. We also acknowledge financial support by the Academy of Finland (decision numbers 141481 and 286713) and by KAUTE Foundation (201500457). We are grateful to the staff of the MAX IV laboratory for affording the use of the research facilities.

Appendix A. Supplementary data

Supplementary data to this article can be found online at http://dx.doi.org/10.1016/j.scriptamat.2016.03.016.

References

[1] S.-L. Zhang, M. Östling, Crit. Rev. Solid State Mater. Sci. 28 (2003) 1–129, http://dx.doi.org/10.1080/10408430390802431.
[2] S. Banerjee, S.K. Mohapatra, M. Misra, J. Phys. Chem. C 115 (2011) 12643–12649, http://dx.doi.org/10.1021/jp106879p.

[3] Y. Lin, S. Zhou, X. Liu, S. Sheehan, D. Wang, J. Am. Chem. Soc. 131 (2009) 2772–2773, http://dx.doi.org/10.1021/ja808426h.
[4] P. Ritterskamp, A. Kuklya, M.-A. Wüstkamp, K. Kerpen, C. Weidenthaler, M. Demuth, Angew. Chem. Int. Ed. 46 (2007) 7770–7774, http://dx.doi.org/10.1002/anie.200701626.
[5] R.C. Rossi, N.S. Lewis, J. Phys. Chem. B 105 (2001) 12303–12318, http://dx.doi.org/10.1021/jp011861c.
[6] J.-P. Colinge, C.A. Colinge, Physics of Semiconductor Devices, Kluwer Academic Publishers, 2002 (eBook ISBN: 9780306476228).
[7] J.C. Hill, A.T. Landers, J.A. Switzer, Nat. Mater. 14 (2015) 1150–1155, http://dx.doi.org/10.1038/nmat4408.
[8] S. Hu, M.R. Shaner, J.A. Beardslee, M. Lichterman, B.S. Brunschwig, N.S. Lewis, Science 344 (2014) 1005–1009, http://dx.doi.org/10.1126/science.1251428.
[9] M.J. Kenney, M. Gong, Y. Li, J.Z. Wu, J. Feng, M. Lanza, H. Dai, Science 342 (2013) 836–840, http://dx.doi.org/10.1126/science.1241327.
[10] Omicron NanoTechnology NanoESCA, 2016. See www.scientaomicron.com for details of the instrument.
[11] Elmitec SPELEEM III, 2016. See www.elmitec.de for details of the instrument.
[12] R. Nyholm, J. Andersen, U. Johansson, B. Jensen, I. Lindau, Nucl. Instrum. Methods Phys. Res. Sect. A 467468 (Part 1) (2001) 520–524, http://dx.doi.org/10.1016/S0168-9002(01)00399-0 (7th Int. Conf. on Synchrotron Radiation Instrumentation).
[13] F. Zhao, X. Cui, B. Wang, J. Hou, Appl. Surf. Sci. 253 (2006) 2785–2791, http://dx.doi.org/10.1016/j.apsusc.2006.05.054.
[14] W.-C. Yang, H. Ade, R.J. Nemanich, J. Appl. Phys. 95 (2004) 1572–1576, http://dx.doi.org/10.1063/1.1636526.
[15] P. Tam, Y. Cao, L. Nyborg, Surf. Sci. 606 (2012) 329–336, http://dx.doi.org/10.1016/j.susc.2011.10.015.
[16] C. Palacio, A. Arranz, Appl. Surf. Sci. 253 (2007) 4283–4288, http://dx.doi.org/10.1016/j.apsusc.2006.09.031.
[17] S. Ogawa, T. Kouzaki, T. Yoshida, R. Sinclair, J. Appl. Phys. 70 (1991) 827–832, http://dx.doi.org/10.1063/1.349641.
[18] C. Kim, S.-W. Kim, C.-H. Hong, D.-W. Kim, H.-K. Baik, C. Whang, J. Cryst. Growth 189–190 (1998) 720–724, http://dx.doi.org/10.1016/S0022-0248(98)00270-X.
[19] H. Jeon, R. Nemanich, Thin Solid Films 184 (1990) 357–363, http://dx.doi.org/10.1016/0040-6090(90)90432-D.
[20] The MAX IV Laboratory, 2016. See information about MAX II beamline I311: www.maxlab.lu.se.
[21] H. Jeon, C.A. Sukow, J.W. Honeycutt, G.A. Rozgonyi, R.J. Nemanich, J. Appl. Phys. 71 (1992) 4269–4276, http://dx.doi.org/10.1063/1.350808.
[22] J.C. Barbour, A.E.M.J. Fischer, J.F. van der Veen, J. Appl. Phys. 62 (1987) 2582–2584, http://dx.doi.org/10.1063/1.339433.

Paper IV

Highly efficient charge separation in model Z-scheme $TiO_2/TiSi_2/Si$ photoanode by micropatterned titanium silicide interlayer

Markku Hannula, Harri Ali-Löytty, Kimmo Lahtonen, Jesse Saari, Antti Tukianen, and Mika Valden

Acta Materialia, 174, p. 237–245, 2019.
DOI: 10.1016/j.actamat.2019.05.032.

Acta Materialia 174 (2019) 237–245

Contents lists available at ScienceDirect

Acta Materialia

journal homepage: www.elsevier.com/locate/actamat

Full length article

Highly efficient charge separation in model Z-scheme $TiO_2/TiSi_2/Si$ photoanode by micropatterned titanium silicide interlayer

M. Hannula [a], H. Ali-Löytty [a], K. Lahtonen [a], J. Saari [a], A. Tukiainen [b], M. Valden [a, *]

[a] Surface Science Group, Laboratory of Photonics, Physics Unit, Tampere University, P.O. Box 692, FI-33014 Tampere, Finland
[b] Optoelectronics Research Centre, Laboratory of Photonics, Physics Unit, Tampere University, P.O. Box 692, FI-33014 Tampere, Finland

ARTICLE INFO

Article history:
Received 1 October 2018
Received in revised form
11 April 2019
Accepted 15 May 2019
Available online 21 May 2019

Keywords:
Titanium dioxide
Electronic band structure
Transition metal silicides
X-ray photoelectron spectroscopy (XPS)
Electrochemical characterization

ABSTRACT

Atomic layer deposited (ALD) TiO_2 is an attractive material for improving the photoactivity and chemical stability of semiconductor electrodes in artificial photosynthesis. Using photoelectrochemical (PEC) measurements, we show that an interfacial, topographically microstructured $TiSi_2$ layer inside the TiO_2/Si heterojunction improves the charge carrier separation and shifts the water dissociation onset potential to more negative values. These observations are correlated with the X-ray photoelectron spectroscopy (XPS) and ultra-violet photoelectron spectroscopy (UPS) measurements, which reveal an increased band bending due to the $TiSi_2$ interlayer. Combined with the UV–Vis absorption results, the photoelectron spectroscopy measurements allow the reconstruction of the complete energy band diagram for the $TiO_2/TiSi_2/Si$ heterojunction and the calculation of the valence and conduction band offsets. The energy band alignment and improvements in PEC results reveal that the charge transfer across the heterojunction follows a Z-scheme model, where the metal-like $TiSi_2$ islands act as recombination centers at the interface.

IV

1. Introduction

Converting solar energy directly into clean, easily storable hydrogen fuel has attracted a great deal of interest since its original discovery by Fujishima and Honda [1]. The method is based on photosynthetic water splitting, where semiconductor electrodes are used for photon absorption and charge transfer for enabling water oxidation and reduction [2]. A typical device consists of two electrodes: photoexcited holes are transferred to the photoanode for an oxygen evolution reaction (OER) and photoexcited electrons to the photocathode for a hydrogen evolution reaction (HER). Effective operation of the device requires that the photogenerated charge carriers (electron–hole pairs) can be separated efficiently and the charge transfer resistance can be minimized.

In recent years, especially TiO_2 has attracted tremendous research interest as both a photoactive and a protective layer on the surface of other small-band gap semiconductors such as Si, GaAs, and GaP. Especially the atomic layer deposited, electronically "leaky" TiO_2 has proven to be a very beneficial material for both OER and HER electrode coatings due to its electrical conductance and passivating properties [3–7]. However, the coupling between the TiO_2 overlayer and the semiconductor substrate requires careful interface engineering such that the charge transfer and the charge separation can be optimized. For example, on Si based electrodes the insulating SiO_2 native oxide at the interface can produce an excess barrier for charge transfer and cause a voltage loss across the heterojunction [8]. The problem has been mitigated, e.g., by depositing metallic Ti between the Si and TiO_2 layers immediately after cleaning the Si substrate from native oxide [5,9]. Another option for improving the charge transfer across the heterojunction is to nanotexture the interface [10]. Also the charge separation capabilities, i.e. band bending, have been studied extensively [4,8,11]. For example Perego et al. [12] have measured how different interlayer materials at the TiO_2/Si interface affect the band alignment of the heterojunction.

Also the Schottky barrier formation at the transition metal silicide/Si interface in general has attracted a lot of interest [13–18]. Different models have related the barrier properties, for example, to the phase stoichiometry and structure [13], the chemical interactions at the interface [14] or heat of formation [15]. However, the results have often been contradictory with only a few details of the silicide fabrication process, layer thickness or oxide impurities

* Corresponding author.
E-mail address: mika.valden@tuni.fi (M. Valden).
URL: http://research.tuni.fi/surfsci

https://doi.org/10.1016/j.actamat.2019.05.032
1359-6454/

and how they may affect the energy band structure. Additionally, lateral nano- or micro-scale variations in the interface structure produce further anomalies as the electric field gets pinched off inside the silicide structures, as analytically predicted by Tung [19,20] and later verified by e.g. Rossi et al. [21,22].

In this study, a micropatterned, laterally inhomogeneous $TiSi_2$ interlayer structure has been fabricated by thermally reducing a predeposited ALD grown TiO_2 film on an Si electrode into $TiSi_2$ followed by an ALD growth of a photoactive TiO_2 thin film onto the $TiSi_2$ layer. $TiSi_2$ has almost metal-like conductance, and due to the high temperature annealing in ultra-high vacuum, the insulating SiO_2 film can be removed between the Si and the $TiSi_2$ islands. Also, the properties of the $TiSi_2$ patterns can be adjusted by altering the thickness of the original TiO_2 interlayer before annealing. Furthermore, our photoelectrochemical measurements show that this affects the heterojunction band alignment and thus the onset potential for water splitting. We have used a combination of photoelectron spectroscopy (PES) and UV–Vis absorption spectroscopy to obtain complete understanding of the band energy diagram of the $TiO_2/TiSi_2/Si$ heterojunction. The effects of the band alignment modifications have been verified by photoelectrochemistry (PEC) and surface photovoltage (SPV) measurements. The results show that an ultra-thin $TiSi_2$ interlayer induces a significant improvement (decrease) on the onset potential for photoelectrochemical water oxidation. The band alignment studies clearly show that the charge transfer follows the Z-scheme mechanism [23–27], where the interlayer acts as a charge recombination region.

2. Materials and methods

The P-doped (resistivity 1–20 Ω·cm) n-type Si(100) wafers were purchased from Wafer World, Inc. (Florida, USA). The 400 μm thick, 3 in. diameter prepolished wafers had been cut in the (100) orientation with a ± 1° accuracy. For the experiments 10× 10 mm^2 squares were cleaved. The Si substrates were first cleaned by sonicating them for 45 min in 99.5% EtOH followed by a combination of annealing and atomic hydrogen treatments in UHV. The details of the UHV cleaning procedure are described in Ref. [28]. In short, the samples were first annealed to 1000 °C to remove native oxide. After this they were exposed to atomic hydrogen at 800 °C (10 min) and 400 °C (10 min) at $p_H = 1.0 \times 10^{-7}$ mbar, which removed the segregated Cu and Ni impurities, respectively. In all stages the sample temperature was monitored with a pyrometer (Land Cyclops 160B) using an emissivity value of $\varepsilon = 0.60$. The pyrometer reading was calibrated against a type K thermocouple in a separate system. After annealing, the surface cleanness and structure were verified by X-ray photoelectron spectroscopy and low energy electron diffraction (LEED) (See Refs. [28,29]). After the UHV cleaning, the samples were cooled down in UHV and transferred to the ALD system through the atmosphere. The exposure to air was kept less than 5 min.

2.1. Atomic layer deposition

The ALD deposition of TiO_2 was carried out using a Picosun Sunale ALD R200 Advanced reactor. Tetrakis(dimethylamido)titanium(IV) ($Ti(N(CH_3)_2)_4$, TDMAT, 99%, Strem Chemicals Inc., France), deionized water, and Ar (99.9999%, Oy AGA Ab, Finland) were used as the Ti precursor, O precursor, and carrier/purge/venting gas, respectively. The film growth rate was calibrated by ellipsometry (Rudolph Auto EL III Ellipsometer, Rudolph Research Analytical). During the ALD, the Si substrate temperature was kept at 200 °C. The vapor pressure of the TDMAT was increased to 3.6 mbar by heating the precursor bubbler to 76 °C, and the precursor gas delivery line was heated to 85 °C to prevent condensation. The water bubbler was sustained at 18 °C by a Peltier element for stability control. The substrate temperature was stabilized for 30 min before starting the deposition. The 200 °C ALD growth temperature was selected because it results in an amorphous growth whereas higher ALD temperatures produce strongly crystallized anatase TiO_2 [30,31]. On the other hand, much lower substrate temperature would result in an incomplete precursor dissociation leading to higher remnant impurity concentrations, especially nitrogen from TDMAT. Low temperature deposition also produces more stoichiometric TiO_2 which, based on our previous research, cannot be modified by the post-treatments as effectively as the films grown at 200 °C [29].

Three separate depositions were conducted for each $TiO_2/TiSi_2/Si$ sample: (1) a 3, 10, or 30 nm thick film (84, 280, or 804 ALD cycles, respectively), which was converted into $TiSi_2$ by post annealing, (2) a 3 nm thick film was deposited on top of the previous $TiSi_2$ interlayer to enable interface analysis by XPS and UPS, and (3) finally a 27 nm film was deposited to reach a total TiO_2 film thickness of 30 nm, which is shown to be practical for PEC applications. Additionally, a control sample without any $TiSi_2$ interlayer (i.e. without step 1) was grown. After each ALD deposition step the samples were cooled down in nitrogen gas before transferring them back to UHV for post-treatments and photoelectron spectroscopy (PES) measurements. The exposure to ambient atmosphere during the transfer was approximately 5 min.

2.2. Formation of the $TiSi_2$ island structure

The post-annealing for converting TiO_2 film into $TiSi_2$ was performed in the preparation chamber of the NanoESCA spectromicroscopy system (Omicron NanoTechnology GmbH) [32]. The sample was annealed at 950 °C for 10 min. The heating setup consisted of a resistive PBN-heating element mounted to a manipulator close to the backside of the sample and the sample held in a Mo sample plate. The temperature was increased to the target value in approximately 5 min and monitored with a pyrometer. After the annealing the sample was transferred to the analysis chamber under UHV conditions for PES measurements.

2.3. Photoelectron spectroscopy

The PES measurements were conducted in the analysis chamber of the NanoESCA system with a base pressure below 1×10^{-10} mbar. Focused monochromatized Al Kα radiation ($h\nu = 1486.5$ eV) was utilized for core level XPS whereas valence band UPS spectra were measured with a focused nonmonochromatized He Iα radiation ($h\nu = 21.22$ eV) using HIS 13 VUV Source (Focus GmbH). Under the normal operation mode the X-ray source produces 36 W (12 kV × 3 mA) of emission power. In some cases this induced measurable surface photovoltages (SPV) (< 0.15 eV) on the studied samples thus distorting the band position measurements [33]. To compensate this, the Si 2p spectra were measured also with 6 W X-ray power and the true band positions were deduced from these two measurements. Similar compensation was made for He Iα induced SPV by comparing the X-ray excited Si 2p core level position with and without He Iα radiation.

The XPS and UPS spectra were collected at the 0° takeoff angle with a photoemission electron microscope (PEEM) paired with a double hemispherical energy analyzer. The spectroscopic data was collected with only one hemisphere and a channeltron detector. For energy filtered imaging the second hemisphere was connected in series with the first one and the data was collected with a full field 2D multichannel plate detector. The energy resolution of the analyzer was set to 400 meV (pass energy 100 eV, slit 1 μm) and

100 meV (pass energy 50 eV, slit 0.5 μm) for XPS and UPS, respectively. In the spectroscopic mode the analysis area was set to 230 μm in diameter for XPS and 95 μm for UPS, corresponding to the maximum spot sizes of the radiation sources. Large analysis areas ensured that the results represent the average surface composition. In imaging mode the FoV was reduced to 35 μm to obtain better spatial resolution.

The chemical states of the elements were determined from the core level XP spectra by least-squares fitting of asymmetric Gaussian–Lorentzian line shapes after subtracting a Shirley type background. The analysis was made in CasaXPS software version 2.3.17PR1.1 [34] using the Scofield photoionization cross-sections as relative sensitivity factors. The valence band maximum (VBM) and work function (WF) values were analyzed from UPS spectra and energy filtered image stacks. The value for the VBM was determined as the intersection between the background and the linear portion of the valence band leading edge and finally shifted 0.10 eV to a higher binding energy due to the analyzer related broadening, as measured on an Ag(111) reference sample. Similarly, the WF value was determined as the intersection between the background and the linear portion of the secondary electron cutoff edge. The WF value was corrected for the Schottky effect by shifting them to 98 meV higher energy [35]. The binding energy (E_b) scale of the energy analyzer was calibrated by setting the Ag(111) single crystal VBM to 0 eV.

2.4. Photoelectrochemical analysis

In order to improve the stability of the ALD deposited amorphous TiO_2 film against alkaline PEC conditions the samples used for the PEC measurements were annealed in a tube furnace in air at 400 °C for 45 min [29,36]. The heat treatment induced crystallization of amorphous TiO_2 into rutile TiO_2 with a band gap of 3.2 eV [36]. After this the photoelectrochemical performance was studied in a homemade PEC cell (PTFE body, volume 3.5 cm^3), using a three-electrode system controlled by the Autolab PGSTAT12 potentiostat (Metrohm AG). The PEC tests were conducted for the same four samples that were used in the PES measurements. This approach allowed us one-to-one correlation between the PES and PEC results. First, the back side of the samples was gently ground using a diamond file, and then the samples were inserted between a rubber O-ring and a stainless steel plate. The steel plate on the back side provided the electrical contact and the O ring ensured a well defined 0.28 cm^2 planar projected electrode surface area. An Ag/AgCl electrode (Leak-Free LF-2, Warner Instruments, LLC) and a Pt wire (surface area 0.82 cm^2) were used as reference and counter electrodes, respectively, in an aqueous solution of 1 M NaOH (pH = 13.6). The potential values were converted to the reversible hydrogen electrode (RHE) scale by the equation $V_{RHE} = V_{Ag/AgCl} + 0.197\ V + pH \times 0.059\ V$. Simulated solar spectrum was produced with a HAL-C100 solar simulator (Asahi Spectra Co., Ltd., JIS Class A at 400–1100 nm with AM1.5G filter) and the intensity was adjusted to 1.00 Sun using a 1 sun checker (model CS-30, Asahi Spectra Co., Ltd.). The photon flux was directed to the sample front surface through a 5 mm thick quartz glass window and a 18 mm thick electrolyte layer.

A unified PEC test program containing all the procedures was applied to test the samples using Nova 1.11 software. The PEC testing was started after a 10 min stabilization time by electrochemical impedance spectroscopy (EIS) at the open circuit potential (OCP) in dark with a frequency range from 0.1 Hz to 43 kHz. Then, the sample was subjected to a chopped light OCP measurement. Finally, a linear scan voltammetry (LSV) measurement was performed at 50 mV/s between the OCP and 2.0 V vs. RHE. Three potential scans were performed in the following order: 1. under simulated solar illumination, 2. in dark, 3. under simulated solar illumination. The first scan was omitted from the results.

2.5. Grazing incidence X-ray diffraction

The phase structure of the samples was investigated with Grazing Incidence X-ray diffraction (GIXRD, Panalytical X'Pert^3 PRO MRD) using Cu Kα radiation ($\lambda = 1.5405$ Å, $h\nu = 8.04$ keV) and 45 kV and 40 mA cathode voltage and current, respectively. The samples were scanned in 2θ between 22° and 52° by using a grazing-incidence angle of 0.3° for X-rays. The GIXRD measurements were conducted after the 3 + 27 nm TiO_2 ALD depositions and the tube furnace annealing. Thus the crystallinity of both the $TiSi_2$ film and the topmost TiO_2 film could be studied.

3. Results and discussion

3.1. Topographical and structural properties of the $TiSi_2$ islands

As shown in our previous study [28], a 30 nm thick ALD grown TiO_2 layer can be converted into highly topographically microstructured $TiSi_2$ patterns. In the present study, more attention is paid to controlling and understanding the structural and electronic properties of the $TiSi_2$ interlayer. Fig. 1 shows the scanning electron microscope (SEM) images of three different $TiSi_2$ layers that are fabricated from the 3, 10, and 30 nm thick TiO_2 ALD films. As can be seen, the thickness strongly affects the structure of the $TiSi_2$ surface. In the case of a 3 nm film, the structure consists of clearly separated $TiSi_2$ islands with a diameter variation approximately from 10 to 100 nm. With a thicker 10 nm film the TiO_2 to $TiSi_2$ transformation leads to much bigger islands with a diameter range from approximately 50 nm to 500 nm. In addition, some coalescence can be observed in this case but most of the islands are still detached from each other. Interesting change happens between the 10 nm and 30 nm layer thicknesses, where most of the $TiSi_2$ patterns start to coalesce into a continuous $TiSi_2$ network. As will be discussed later in more detail, this has a significant effect on the charge transfer properties. $TiSi_2$ has much lower resistivity than, for example, the underlying Si substrate. Thus a continuous $TiSi_2$ network enables the photogenerated charge carriers to escape along the surface plane instead of conducting them through the layer structure. Also the total coverage of the $TiSi_2$ patterns increases as the original TiO_2 film and island size become bigger. This is illustrated in Fig. 1(d).

Fig. 2 shows the GIXRD patterns measured from the $TiO_2/TiSi_2/Si(100)$ heterojunction systems without $TiSi_2$ and with 3, 10 and 30 nm $TiSi_2$ interlayers. Only rutile (α-TiO_2) and $TiSi_2$ related diffraction maxima can be observed. The intensity of the rutile peaks remains similar on all four samples, which is expected because the TiO_2 film thickness is 30 nm on all four samples. On the other hand, the intensity of the $TiSi_2$ main peak at $2\theta = 39.2°$ shows some correlation with the thickness of the TiO_2 film that was used for $TiSi_2$ fabrication and also the $TiSi_2$ coverage.

3.2. Photoelectrochemical activity and charge transfer resistance

Fig. 3 illustrates the results of the PEC analysis for all four α-$TiO_2/TiSi_2/Si$ samples with varying $TiSi_2$ interlayer thicknesses. The EIS data in (a) reveals that the samples with a $TiSi_2$ interlayer show lower impedance compared to the sample without $TiSi_2$, in particular, in the medium frequency range (0.1–1 kHz). The simplified electric equivalent circuit (EEC) that adequately describes the measured EIS data in (a) has three parallel R and C elements in series, $(RC)(RC)(RC)$. The first (R_1C_1) describes the depletion zone of the Si substrate, the second (R_2C_2) the TiO_2/Si interface, and the third (R_3C_3) the TiO_2 layer capacitance. We note

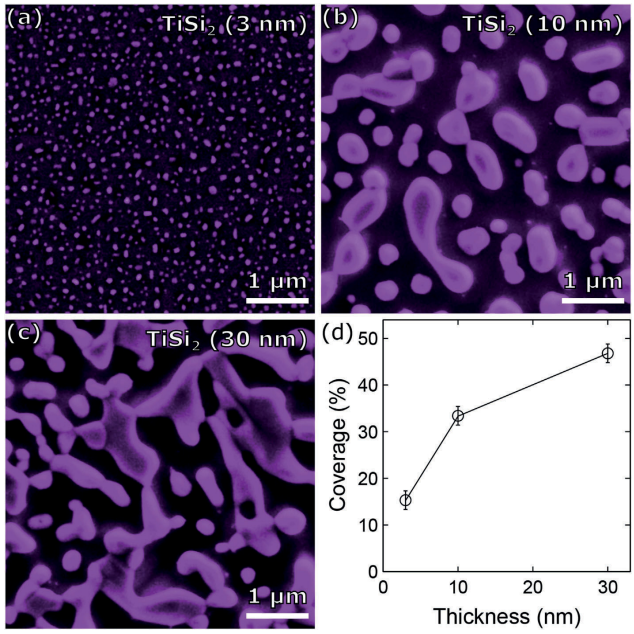

Fig. 1. (a–c) Scanning electron microscopy (SEM) images of $TiSi_2$/Si surfaces. The thickness value (3, 10 or 30 nm) indicates the original TiO_2 layer thickness used for the silicide formation. (d) The $TiSi_2$ island coverage shows sublinear growth as a function of the TiO_2 layer thickness.

that the two time constant model (*RC*)(*RC*) that is typically applied to SiO_2/Si electrodes is not adequate to describe the samples with the interfacial $TiSi_2$, which gives rise to the additional time constant in the medium frequency range (0.1–1 kHz) [39]. The fitted EEC parameters are presented in Table 1. The TiO_2 layer capacitance (C_3) is directly proportional to the electrochemically active surface area. Therefore, the increased C_3 value of the sample with the 30 nm $TiSi_2$ interlayer stems from the more rough surface morphology in line with Ref. [28].

The chopped light OCP measurement in Fig. 3 (b) shows a negative shift in the OCP upon illumination for all four samples, which is characteristic to n-type photoelectrodes. However, the photoresponse is faster and the photovoltage is higher for the 3 and 10 nm $TiSi_2$ interlayers when compared to the samples without $TiSi_2$ or with the 30 nm coalesced $TiSi_2$ layer. Also, the photocurrent onset potentials were more negative than the ones we reported for similar ALD TiO_2 (30 nm)/Si photoanodes after different heat-treatment temperatures between 200 °C and 500 °C [36]. Therefore, it can be concluded that thin enough $TiSi_2$ interlayers improve the charge carrier separation at the TiO_2/Si interface and facilitate a more favorable band bending. Finally, the photocurrent onset potential for water oxidation in Fig. 3(c) shows a significant shift (70–100 mV) to more negative values for the 3 and 10 nm $TiSi_2$ interlayers when compared to the samples without $TiSi_2$ or with the 30 nm coalesced $TiSi_2$ layer. The improved charge separation and more negative onset potential are also supported by the SPV experiments made in UHV conditions. Under strong UV illumination the samples with the 3 and 10 nm $TiSi_2$ interlayers exhibit highest surface photovoltage (See Supplementary Information Fig. S1 for details.)

An interesting detail in Fig. 3(c) is the rapid increase in both dark and light currents around 1.5 V vs. RHE for the sample with the 30 nm $TiSi_2$ interlayer. Such an increase in the dark current, i.e. oxidation of H_2O without light, is an indication of low charge transfer resistance of the $TiSi_2$/Si substrate, which may be a consequence of the possible doping of n-Si with Ti [40] during the $TiSi_2$ synthesis at 950 °C. The slightly higher saturation photocurrent of the sample with the 30 nm $TiSi_2$ interlayer, on the other hand, is assigned to stronger TiO_2 absorption that is induced by more rough surface morphology as pointed out above.

3.3. Molecular bonding of the TiO_2/$TiSi_2$/Si heterojunction

Understanding how the $TiSi_2$ interlayer affects the charge transfer properties, the molecular bonding in addition to the band energy diagram of the TiO_2/$TiSi_2$/Si heterojunction needs to be determined. Therefore, the samples were studied in a stepwise manner with both XPS and UPS. Ti 2p, Si 2p, O 1s, VB and WF values (secondary electron cutoff features) were measured and analyzed at each step: on a clean Si surface, after formation of the $TiSi_2$ interlayers, and finally after deposition of the 3 nm TiO_2 layer on top of the $TiSi_2$ interlayers. Fig. S2 illustrates the development of the Si 2p and Ti 2p core level spectra measured on a clean Si surface and the three different $TiSi_2$ layers. As can be seen, the 950 °C $TiSi_2$ formation temperature is adequate for removing practically all oxide components from both Si and Ti, i.e. there are no $2p_{3/2}$

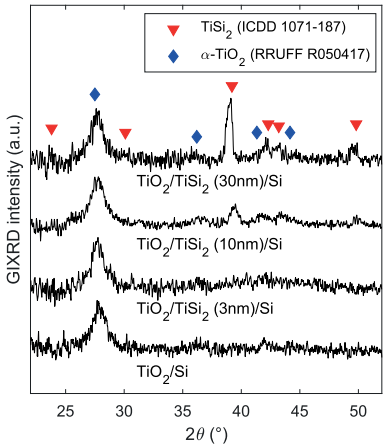

Fig. 2. GIXRD patterns from $TiO_2/TiSi_2/Si(100)$ heterojunction systems. The diffraction patterns show that the original 3, 10 or 30 nm thick TiO_2 film has been converted into $TiSi_2$ during the UHV annealing. The topmost TiO_2 film has been crystallized into rutile (α-TiO_2) during the 400 °C annealing in air. The numbers in the legend correspond to XRD references in ICDD [37] and RRUFF [38] databases.

photoelectron peaks at 103 or 459 eV binding energy regions corresponding to the Si and Ti oxides, respectively [41]. The Si 2p spectrum of the cleaned substrate consists only of the doublet separated elemental 1/2 and 3/2 states at $E_{b,(3/2)} = 99.25 \pm 0.05$ eV. After the $TiSi_2$ formation, an additional doublet state appears at $E_{b,(3/2)} = 98.85 \pm 0.05$ eV corresponding to the Ti bound Si atoms. The area of this peak correlates well with the increasing $TiSi_2$ coverage observed in the SEM images. For Ti 2p, only one doublet state is detected at $E_{b,(3/2)} = 458.68 \pm 0.05$ eV originating from the silicidized Ti. Also in this case the area of the peak increases concurrently with the Si_{TiSi_2} peak area and the $TiSi_2$ island coverage. Fig. S3 shows the valence band maxima (VBM) for the Si and $TiSi_2/Si$ surfaces, and the corresponding WF values analyzed from the secondary electron cutoff are depicted in Fig. S4. The VBM of $TiSi_2$ is located at the Fermi level within the experimental error. This is as expected, because $TiSi_2$ in known to be nearly metallic material with a low resistivity [42].

The WF values for both the clean Si and the three different $TiSi_2/Si$ surfaces are close to each other. The 3 and 10 nm $TiSi_2$ layers exhibits a slightly higher WF value of 4.72 eV if compared to the WF value of clean Si (4.61 eV). However, the 30 nm $TiSi_2$ layer shows again almost the same average WF value as the clean Si. One noticeable difference is the increased dispersion in WF values in the case of the 30 nm $TiSi_2$ layer. The work function map shows a clear contrast between the $TiSi_2$ regions (highest WF) and the intervening Si areas (lowest WF). For the clean Si and the 3 and 10 nm $TiSi_2$ layers the work function maps are rather homogeneous. The difference between the TiSi surfaces can be explained by the "pinch-off" effect [43] where the barrier variation of sufficiently small island features becomes pinched off by the surrounding semiconductor regions. For example Rossi et al. [21,22] have studied this phenomenon on electrolyte/Ni island/n-Si systems. With small Ni islands the effective barrier height drifts closer to that of the surrounding semiconductor surface. However, as the islands become larger, the band bending inside the islands behaves more independently and the barrier height moves closer to the barrier height of a continuous metallized surface. The size of the Ni islands studied by Rossi et al. varied from 20 nm to 1500 nm, and the upper limit of the island diameter for pinch-off was found to be approximately 350 nm. The result is in agreement with our measurements, where the 3 and 10 nm $TiSi_2$ layers with clearly sub-micrometer sized $TiSi_2$ features show almost no WF variation and the thickest

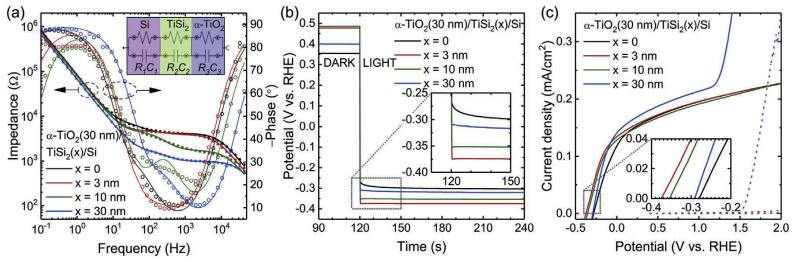

Fig. 3. Photoelectrochemical analysis of α-$TiO_2/TiSi_2/Si$ heterojunction systems in 1 M NaOH. (a) EIS Bode plots showing impedance (solid symbols) and phase shift (open symbols) measured at the OCP in dark before applying any bias potential. Electrochemical equivalent circuit used for EIS data modelling is shown as an inset in (a) and solid lines show the fits. (b) Chopped light OCP measurement. (c) Linear scan voltammetry measured at 50 mV/s in dark (dashed lines) and under simulated solar illumination (solid lines).

Table 1
Fitted EIS data for α-$TiO_2/TiSi_2/Si$ heterojunction systems using $(RC)(RC)(RC)$ electric equivalent circuit.

TiO_2(30 nm)/$TiSi_2$(x)/Si	R_1 (kΩ)	C_1 (nF)	R_2 (kΩ)	C_2 (μF)	R_3 (MΩ)	C_3(μF)	χ^2
x = 0 nm	4.1	4.7	2.2	1.4	14.3	1.9	0.13
x = 3 nm	3.9	6.1	0.8	0.9	2.8	2.0	0.35
x = 10 nm	1.7	7.2	2.5	0.4	1.2	2.0	0.54
x = 30 nm	1.0	6.2	0.6	1.2	11.0	2.4	0.04

IV

30 nm $TiSi_2$ has clearly distinct areas of different WF values. These large $TiSi_2$ islands prevent the pinch-off effect and lead to a lowered barrier height (lowered band bending), which decreases the charge separation performance. In the 3 and 10 nm layers the negative effect of the $TiSi_2$ particles on the barrier height gets pinched off, but the particles can still act as effective minority carrier collectors and thus promote the water splitting reaction [21].

Fig. 4 shows the Ti 2p and Si 2p XP spectra after the 3 nm TiO_2 deposition. The 3 nm film is thin enough so that all three layers (the Si substrate, $TiSi_2$ interlayer and TiO_2 film) can contribute their own chemical states to the spectra. The oxidized components of Ti (Ti^{4+} and Ti^{3+}) are similar for each sample and represent a partially reduced ALD deposited TiO_2 film as reported in our previous studies [29,36]. Also the previously mentioned $TiSi_2$ can be detected through the TiO_2 film enabling the full band energy diagram reconstruction of the whole heterojunction. The Si 2p spectra resemble those measured in the previous step, just strongly attenuated due to the 3 nm TiO_2 overlayer. Additionally, a small amount of Si oxide is detected. The spatial distribution of SiO_x could not be resolved with the available resolution, but as we have previously shown [28], the $TiSi_2$ structures are resilient to oxidation. Thus the oxidation is assumed to happen on the Si areas that are not covered by the $TiSi_2$ islands.

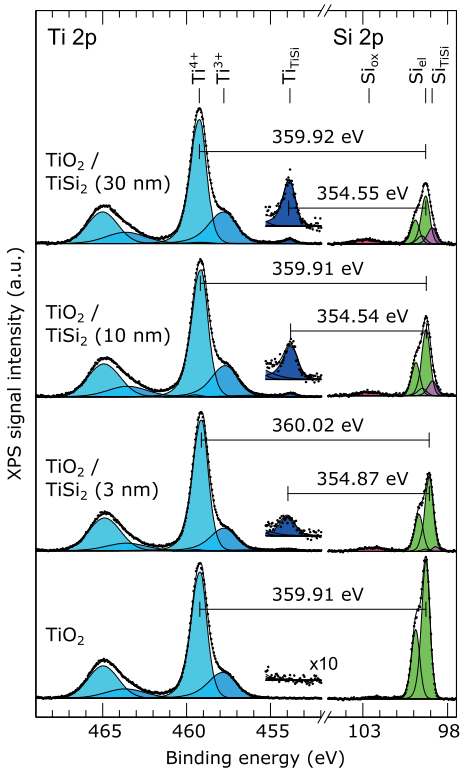

Fig. 4. Ti 2p and Si 2p XP spectra of the $TiO_2/TiSi_2/Si$ heterojunctions. The spectral features originate from all three layers: the Si substrate, $TiSi_2$ interlayer (the bottom spectrum without $TiSi_2$, the upper spectra with $TiSi_2$ interlayers that were formed from the 3, 10, or 30 nm thick TiO_2 films) and the TiO_2 film (3 nm thick).

3.4. Determination of the band energy diagram of the $TiO_2/TiSi_2/Si$ heterojunction

In order to understand why the $TiSi_2$ interlayer affects the onset potential and charge transport properties of the three-layer photoanode system, a complete band energy diagram was reconstructed. Fig. 5 shows the band positions of VBM, CBM, E_{vac} and selected core levels for each intermediate deposition step and all three different $TiSi_2$ film thicknesses. The band energy diagram of the cleaned Si substrate is shown in Fig. 5(a). The E_g value of 1.12 eV for Si bulk was taken from the literature [4] and the $(E_F - VBM)_{bulk}$ distance of 0.85 eV was calculated from the silicon wafer resistivity [44]. The band gap for amorphous TiO_2 was determined by measuring the optical absorption of the film with a spectrophotometer. The details of this measurement are shown in the supplementary information (Fig. S5).

The SPV corrected binding energy of the Si $2p_{Surf}$ was evaluated from XPS measurements. Based on the silicon resistivity, the depletion width is several hundreds of nanometers [45]. Thus, it is valid to assume that the band positions within the XPS and UPS information depth are constant and reflect the band positions of the surface.

The distance between the Si 2p and Si VBM was evaluated from XPS and UPS measurements. The obtained value of 98.68 eV is in good agreement with the value of 98.72 eV for the TiO_2/Si heterojunction by Hu et al. [4] The knowledge of the above-mentioned energies allowed the calculation of the 0.23 eV upward band bending for the cleaned Si surface. Combining this information with the WF value (4.61 eV) determined from the UPS secondary electron cutoff edge and the literature based E_g (1.12 eV) allowed us to calculate the CBM and E_{vac} positions above the E_F for both the surface and the bulk phases of Si. As a result of these calculations we obtained an electron affinity (χ) value of 4.11 eV for bulk Si. This is in reasonable agreement with the generally accepted value of 4.05 eV [46,47] and the value of 4.07 eV obtained by Hu et al. [4]. This result can thus be considered as a convenient validation of all the previously mentioned calculations and literature value based assumptions.

Fig. 5(b)–(d) illustrate the similar band diagrams for $TiSi_2$/Si systems, where the $TiSi_2$ structure has been fabricated from the 3, 10, or 30 nm thick TiO_2 films. Most notably, the 3 and 10 nm $TiSi_2$ structures increase the band bending of the underlying Si substrate by about 0.1 eV leading to a total upward bending of 0.34 eV. Also the Si with the 30 nm $TiSi_2$ interface shows a 0.03 eV higher band bending than the clean Si substrate, but this small change is near the experimental detection limit. It should be noted, that the band positions represent the spatially averaged values at the surface. It is possible that the band bending is even stronger near the $TiSi_2$ islands but the small size of the islands prevents the spatially resolved mapping of the localized band energies.

Based on the E_{vac} values of the Si and $TiSi_2$, there is a 0.1 eV surface dipole (δ) at the $TiSi_2$/Si interface with the redistribution of electron density towards the Si substrate. This dipole at least partially accounts for the increased Si band bending when the $TiSi_2$ structure is fabricated on the surface [4,33].

Fig. 5(e)–(h) represent the band diagrams for TiO_2/Si and TiO_2/$TiSi_2$/Si interfaces, where the $TiSi_2$ interfaces, the thickness of which range from 3 to 30 nm, are covered by the 3 nm TiO_2 overlayer. Also in this case the strongest Si band bending is observed for the junctions where the $TiSi_2$ structure has been fabricated from the 3

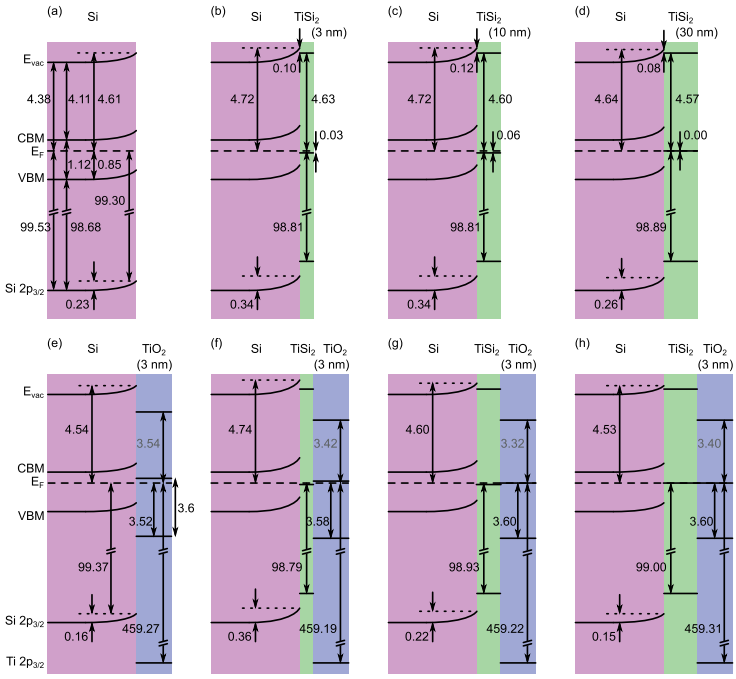

Fig. 5. Band energy diagram of the clean Si (a), titanium silicide coated Si with different $TiSi_2$ interlayers (3, 10, and 30 nm) (b–d), and $TiO_2/TiSi_2/Si$ heterojunction systems where 3 nm of TiO_2 has been deposited on top of structure (e–h).

and 10 nm TiO_2 films. On the other hand, the TiO_2/Si system without a $TiSi_2$ interlayer and also the $TiO_2/TiSi_2$/Si with the 30 nm $TiSi_2$ interlayer express a weaker band bending. Given that the $TiSi_2$ induced band bending of Si is only little affected by the TiO_2 overlayer, it is reasonable to assume that the band bending is similar under the amorphous TiO_2 that was used in the PES measurements and the rutile TiO_2 that was used in the PEC test.

The possibility of adjusting the band bending by altering the $TiSi_2$ layer thickness and coverage provides a powerful way to tune the VBM and CBM offsets. This on the other hand affects the charge separation and charge transport properties across the heterojunction. The band offset between the Si and TiO_2 can be calculated based on the Kraut's method [48,49] using the following equation

$$\Delta E_{VBM} = (E_{Ti\ 2p} - E_{Si\ 2p})_{TiO_2/Si} - \left[(E_{Ti\ 2p} - E_{VBM})_{TiO_2} - (E_{Si\ 2p} - E_{VBM})_{Si}\right], \quad (1)$$

where the subscripts inside the parentheses denote the specific energy levels and the subscripts outside the parentheses denote the material systems, i.e. TiO_2/Si heterojunction or Si and TiO_2 bulk references. In our case the Si and TiO_2 VBMs are located far from each other and the underlying Si substrate gives only a very weak signal in the extremely surface sensitive UPS measurement. Thus, the TiO_2 VBM position can be determined more accurately by measuring it directly from the studied heterojunction samples instead of a bulk reference sample. For this reason the equation can be simplified to

$$\Delta E_{VBM} = (E_{VBM})_{TiO_2} - (E_{Si\ 2p})_{TiO_2/Si} - (E_{Si\ 2p} - E_{VBM})_{Si}. \quad (2)$$

Knowing the band gap for both Si and TiO_2 also enables the calculation of the CBM offsets when the VBM offsets are known Fig. 6 illustrates these offsets for the heterojunction samples with the 3, 10, and 30 nm $TiSi_2$ interlayers. Smallest offsets are observed when the TiO_2 film is deposited directly to the clean Si surface and also in the case of the 30 nm $TiSi_2$ interlayer. On the other hand, the 3 and 10 nm $TiSi_2$ layers increase the band offsets thus leading to a higher photovoltage, which improves the separation of excited charge carriers. VBM offsets ranging from 1 eV up to 2.73 eV have been reported for TiO_2/Si heterojunctions [12,50–52]. The large variation shows that the VBM offset is sensitive to both the preparation method of the TiO_2 film and the interlayer between the Si substrate and the TiO_2 film. For example Perego et al. [12] have reported an offset variation of 0.3 eV by changing the composition of an approximately 2 nm thick interlayer between the Si and TiO_2 layers. The magnitude of the variation is well in line with our observations, although in our case only the topographical properties instead of the composition are varied.

Despite the improved photovoltage and charge carrier separation, higher band offset also means larger barrier height against

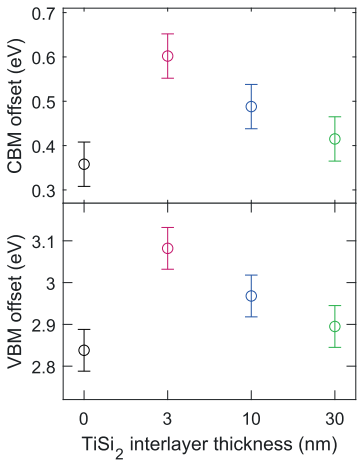

Fig. 6. Valence band maximum (VBM) and conduction band minimum (CBM) offsets for TiO_2/$TiSi_2$/Si heterojunction systems with 0, 3, 10, and 30 nm $TiSi_2$ interlayer thicknesses.

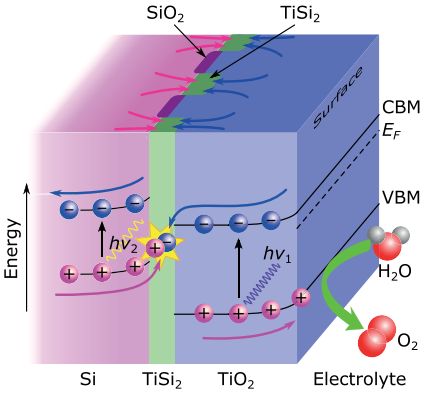

Fig. 7. Schematic illustration of the charge transfer channels in a Z-scheme TiO_2/$TiSi_2$/Si three-layer photoanode in PEC conditions.

charge transport across the junction. This means that the hole injection from the Si side to the TiO_2 side along the VB or the electron injection from the TiO_2 side to the Si side along the CB becomes more obstructed. At first this may seem contradictory to the PEC results, where the 3 and 10 nm $TiSi_2$ interlayers resulted in smaller onset potential and larger or equal photocurrent than without the $TiSi_2$ interlayer or with the 30 nm $TiSi_2$ interlayer.

The above mentioned results can be rationalized based on a Z-scheme model [23–25]. In this model the non-interconnected metal-like $TiSi_2$ islands endow recombination centers inside the heterojunction. As schematically illustrated in Fig. 7, the $TiSi_2$ islands improve the charge separation by increasing the Si band bending and also provide a low resistance charge transfer channel through the native SiO_2. Electrons from the TiO_2 overlayer recombine with the holes from the Si substrate inside the metallic $TiSi_2$ islands according to the Z-scheme mechanism for overall charge transport.

Photons that have higher energy than the TiO_2 band gap can be absorbed in the TiO_2 film and thus produce photogenerated electron–hole pairs. Similarly lower energy photons excite electrons in the underlying Si substrate. In the Z-scheme model the net charge transfer leads to the accumulation of holes on the outer surface of the TiO_2 film and electron accumulation in the Si bulk. In PEC conditions the surface accumulated holes are then readily available for water oxidation.

4. Conclusions

The results constitute a comprehensive study of the electronic structure of TiO_2/$TiSi_2$/Si systems that can be utilized as photoanodes in water splitting reaction. ALD grown "leaky" TiO_2 has been found to exhibit protective and photoactive properties, and it can be used as a buffer layer between the electrolyte and small band gap semiconductors. In this study we used micropatterned $TiSi_2$ interlayer for tailoring the electronic properties of the TiO_2/Si interface. XPS and UPS measurements show that the modification of the $TiSi_2$ interlayer has direct effect on the band alignment across the heterojunction. $TiSi_2$ layers that are thermally formed from the 3 and 10 nm thick TiO_2 films lead to the strongest band bending and largest band offsets. The $TiSi_2$ islands in these structures are small enough for the pinch-off effect, whereas the $TiSi_2$ interlayer formed from the 30 nm TiO_2 film leads to large coalesced $TiSi_2$ islands where the pinch-off effect does not affect any more. This lowers the band bending and decreases the photovoltaic efficiency by reducing the charge carrier separation and shifting the onset potential to more positive values. Based on the photoelectrochemical measurements, the samples with the highest band offset ($TiSi_2$ from the 3 and 10 nm films) yield the best water splitting performance despite their increased barrier height for minority carriers migrating across the junction. This can be explained by the Z-scheme model, where the $TiSi_2$ islands at the heterojunction interface act as recombination centers providing an energetically favorable route for overall charge transport.

Acknowledgement

This work was supported by the Academy of Finland [grant numbers 141481, 286713 and 309920]. M. H. was supported by the TUT's Graduate School and Emil Aaltonen foundation. H. A. was supported by the Jenny and Antti Wihuri Foundation. We thank R. Ulkuniemi for operating the spectrophotometer during the UV–Vis absorption measurements.

Appendix A. Supplementary data

Supplementary data to this article can be found online at https://doi.org/10.1016/j.actamat.2019.05.032.

References

[1] A. Fujishima, K. Honda, Electrochemical photolysis of water at a semiconductor electrode, Nature 238 (1972) 37, https://doi.org/10.1038/238037a0.
[2] M.G. Walter, E.L. Warren, J.R. McKone, S.W. Boettcher, Q. Mi, E.A. Santori, N.S. Lewis, Solar water splitting cells, Chem. Rev. 110 (11) (2010) 6446–6473.
[3] Y.W. Chen, J.D. Prange, S. Dühnen, Y. Park, M. Gunji, C.E.D. Chidsey, P.C. McIntyre, Atomic layer-deposited tunnel oxide stabilizes silicon photoanodes for water oxidation, Nat. Mater. 10 (2011) 539–544.

[4] S. Hu, M.H. Richter, M.F. Lichterman, J. Beardslee, T. Mayer, B.S. Brunschwig, N.S. Lewis, Electrical, photoelectrochemical, and photoelectron spectroscopic investigation of the interfacial transport and energetics of amorphous TiO_2/Si heterojunctions, J. Phys. Chem. C 120 (6) (2016) 3117–3129, https://doi.org/10.1021/acs.jpcc.5b09121.

[5] B. Seger, D.S. Tilley, T. Pedersen, P.C.K. Vesborg, O. Hansen, M. Gratzel, I. Chorkendorff, Silicon protected with atomic layer deposited TiO_2: durability studies of photocathodic H_2 evolution, RSC Adv. 3 (2013) 25902–25907, https://doi.org/10.1039/C3RA45966G.

[6] K. Sivula, Defects give new life to an old material: electronically leaky titania as a photoanode protection layer, ChemCatChem 6 (10) (2014) 2796–2797. https://doi.org/10.1002/cctc.201402532.

[7] J. Gu, Y.D. Yan, J.L. Young, K.X. Steirer, N.R. Neale, J.A. Turner, Water reduction by a p-$GaInP_2$ photoelectrode stabilized by an amorphous TiO_2 coating and a molecular cobalt catalyst, Nat. Mater. 15 (2016) 456–460, https://doi.org/10.1038/nmat4511.

[8] J. Klett, J. Ziegler, A. Radetinac, B. Kaiser, R. Schäfer, W. Jaegermann, F. Urbain, J.-P. Becker, V. Smirnov, F. Finger, Band engineering for efficient catalyst-substrate coupling for photoelectrochemical water splitting, Phys. Chem. Chem. Phys. 18 (2016) 10751–10757, https://doi.org/10.1039/C5CP06230F.

[9] B. Seger, T. Pedersen, A.B. Laursen, P.C.K. Vesborg, O. Hansen, I. Chorkendorff, Using TiO_2 as a conductive protective layer for photocathodic H_2 evolution, J. Am. Chem. Soc. 135 (3) (2013) 1057–1064, https://doi.org/10.1021/ja309523t, pMID: 23289745.

[10] J. Yang, K. Walczak, E. Anzenberg, F.M. Toma, G. Yuan, J. Beeman, A. Schwartzberg, Y. Lin, M. Hettick, A. Javey, J.W. Ager, J. Yano, H. Frei, I.D. Sharp, Efficient and sustained photoelectrochemical water oxidation by cobalt oxide/silicon photoanodes with nanotextured interfaces, J. Am. Chem. Soc. 136 (17) (2014) 6191–6194, https://doi.org/10.1021/ja501513t, pMID: 24720554.

[11] M.F. Lichterman, S. Hu, M.H. Richter, E.J. Crumlin, S. Axnanda, M. Favaro, W. Drisdell, Z. Hussain, T. Mayer, B.S. Brunschwig, N.S. Lewis, Z. Liu, H.-J. Lewerenz, Direct observation of the energetics at a semiconductor/liquid junction by operando X-ray photoelectron spectroscopy, Energy Environ. Sci. 8 (2015) 2409–2416. https://doi.org/10.1039/C5EE01014D.

[12] M. Perego, G. Seguini, G. Scarel, M. Fanciulli, F. Wallrapp, Energy band alignment at TiO_2/Si interface with various interlayers, J. Appl. Phys. 103 (4) (2008) 043509, https://doi.org/10.1063/1.2885109.

[13] P.E. Schmid, P.S. Ho, T.Y. Tan, Summary abstract: correlation between Schottky barrier height and phase stoichiometry/structure of silicidesilicon interfaces, J. Vac. Sci. Technol. 20 (3) (1982) 688–689, https://doi.org/10.1116/1.571629.

[14] J. Freeouf, Silicide Schottky barriers: an elemental description, Solid State Commun. 33 (10) (1980) 1059–1061. https://doi.org/10.1016/0038-1098(80)90317-8.

[15] J.M. Andrews, J.C. Phillips, Chemical bonding and structure of metal-semiconductor interfaces, Phys. Rev. Lett. 35 (1975) 56–59, https://doi.org/10.1103/PhysRevLett.35.56.

[16] J.L. Freeouf, Silicide interface stoichiometry, J. Vac. Sci. Technol. 18 (3) (1981) 910–916, https://doi.org/10.1116/1.570993.

[17] M.A. Taubenblatt, C.R. Helms, Silicide and Schottky barrier formation in the Ti–Si and the Ti–SiO_x–Si systems, J. Appl. Phys. 53 (9) (1982) 6308–6315, https://doi.org/10.1063/1.331551.

[18] R.T. Tung, J.M. Gibson, Single crystal silicide silicon interfaces: structures and barrier heights, J. Vac. Sci. Technol., A 3 (3) (1985) 987–991, https://doi.org/10.1116/1.573372.

[19] R.T. Tung, Electron transport of inhomogeneous Schottky barriers, Appl. Phys. Lett. 58 (24) (1991) 2821–2823, https://doi.org/10.1063/1.104747.

[20] R.T. Tung, Electron transport at metal-semiconductor interfaces: general theory, Phys. Rev. B 45 (1992) 13509–13523, https://doi.org/10.1103/PhysRevB.45.13509.

[21] R.C. Rossi, M.X. Tan, N.S. Lewis, Size-dependent electrical behavior of spatially inhomogeneous barrier height regions on silicon, Appl. Phys. Lett. 77 (17) (2000) 2698–2700, https://doi.org/10.1063/1.1319534.

[22] R.C. Rossi, N.S. Lewis, Investigation of the size-scaling behavior of spatially nonuniform barrier height contacts to semiconductor surfaces using ordered nanometer-scale nickel arrays on silicon electrodes, J. Phys. Chem. B 105 (49) (2001) 12303–12318, https://doi.org/10.1021/jp011861c.

[23] S. Li, Q. Zhao, D. Wang, T. Xie, Work function engineering derived all-solid-state Z-scheme semiconductor-metal-semiconductor system towards high-efficiency photocatalytic H_2 evolution, RSC Adv. 6 (2016) 66783–66787, https://doi.org/10.1039/C6RA14680E.

[24] J.-M. Li, H.-Y. Cheng, Y.-H. Chiu, Y.-J. Hsu, ZnO-Au-SnO_2Z-scheme photoanodes for remarkable photoelectrochemical water splitting, Nanoscale 8 (2016) 15720–15729, https://doi.org/10.1039/C6NR05605A.

[25] H. Tada, T. Mitsui, T. Kiyonaga, T. Akita, K. Tanaka, All-solid-state Z-scheme in $CdSAuTiO_2$ three-component nano junction system, Nat. Mater. 5 (2006) 782, https://doi.org/10.1038/nmat1734, 09/10.

[26] A. Zhang, G. Zheng, C. Lieber, Nanowires: Building Blocks for Nanoscience and Nanotechnology, first ed., Springer International Publishing, 2016.

[27] C. Liu, Y.J. Hwang, H.E. Jeong, P. Yang, Light-induced charge transport within a single asymmetric nanowire, Nano Lett. 11 (9) (2011) 3755–3758, https://doi.org/10.1021/nl201798e.

[28] M. Hannula, K. Lahtonen, H. Ali-Löytty, A. Zakharov, T. Isotalo, J. Saari, M. Valden, Fabrication of topographically microstructured titanium silicide interface for advanced photonic applications, Scripta Mater. 119 (2016) 76–81. https://doi.org/10.1016/j.scriptamat.2016.03.016.

[29] M. Hannula, H. Ali-Löytty, K. Lahtonen, E. Sarlin, J. Saari, M. Valden, Improved stability of atomic layer deposited amorphous TiO_2 photoelectrode coatings by thermally induced oxygen defects, Chem. Mater. 30 (4) (2018) 1199–1208, https://doi.org/10.1021/acs.chemmater.7b02938.

[30] C. Jin, B. Liu, Z. Lei, J. Sun, Structure and photoluminescence of the TiO_2 films grown by atomic layer deposition using tetrakis-dimethylamino titanium and ozone, Nanoscale Res. Lett. 10 (1) (2015) 95.

[31] J. Aarik, A. Aidla, A.-A. Kiisler, T. Uustare, V. Sammelselg, Effect of crystal structure on optical properties of TiO_2 films grown by atomic layer deposition, Thin Solid Films 305 (1) (1997) 270–273. https://doi.org/10.1016/S0040-6090(97)00135-1.

[32] Omicron Nanotechnology, NanoESCA. http://www.scientaomicron.com, 2017.

[33] D.C. Gleason-Rohrer, B.S. Brunschwig, N.S. Lewis, Measurement of the band bending and surface dipole at chemically functionalized Si(111)/vacuum interfaces, J. Phys. Chem. C 117 (35) (2013) 18031–18042. https://doi.org/10.1021/jp401585s.

[34] CasaXPS, Processing software for XPS, AES, SIMS and more. http://www.casaxps.com, 2017.

[35] O. Renault, R. Brochier, P.-H. Haumesser, N. Barrett, B. Krmker, D. Funnemann, Energy-filtered peem imaging of polycrystalline Cu surfaces with work function contrast and high lateral resolution, E-j. of Surf. Sci. and Nanotechnol. 4 (2006) 431–434.

[36] H. Ali-Löytty, M. Hannula, J. Saari, L. Palmolahti, B.D. Bhuskute, R. Ulkuniemi, T. Nyyssönen, K. Lahtonen, M. Valden, Diversity of TiO_2: controlling the molecular and electronic structure of atomic-layer-deposited black TiO_2, ACS Appl. Mater. Interfaces 11 (3) (2019) 2758–2762, https://doi.org/10.1021/acsami.8b20608.

[37] ICDD, International Centre for Diffraction Data, 2018.

[38] RRUFF, Integrated Database of Raman Spectra, X-Ray Diffraction and Chemistry Data for Minerals, 2018.

[39] V. Bertagna, R. Erre, F. Rouelle, M. Chemla, S. Petitdidier, D. Levy, Electrochemical study for the characterisation of wet silicon oxide surfaces, Electrochim. Acta 47 (1) (2001) 129–136. https://doi.org/10.1016/S0013-4686(01)00569-2. http://www.sciencedirect.com/science/article/pii/S0013468601005692.

[40] T. Zhou, Y. Zuo, L. Li, K. Qiu, J. Zheng, Q. Wang, Structural, optical and electrical properties of Ti doped amorphous silicon prepared by co-sputtering, Vacuum 104 (2014) 65–69. https://doi.org/10.1016/j.vacuum.2014.01.004.

[41] NIST X-Ray Photoelectron Spectroscopy Database, NIST Standard Reference Database Number 20, vol. 2000, National Institute of Standards and Technology, Gaithersburg MD, 2018, p. 20899, https://doi.org/10.18434/T4T88K.

[42] S.P. Murarka, D.B. Fraser, A.K. Sinha, H.J. Levinstein, Refractory silicides of titanium and tantalum for low-resistivity gates and interconnects, IEEE J. Solid State Circuits 15 (4) (1980) 474–482, https://doi.org/10.1109/JSSC.1980.1051425.

[43] J.L. Freeouf, T.N. Jackson, S.E. Laux, J.M. Woodall, Effective barrier heights of mixed phase contacts: size effects, Appl. Phys. Lett. 40 (7) (1982) 634–636, https://doi.org/10.1063/1.93171.

[44] W.R. Thurber, R.L. Mattis, Y.M. Liu, J.J. Filliben, Resistivity–dopant density relationship for phosphorus-doped silicon, J. Electrochem. Soc. 127 (1980) 1807–1812, https://doi.org/10.1149/1.2130006.

[45] H. Lüth, Solid Surfaces, Interfaces and Thin Films, sixth ed., Springer, 2014.

[46] S.M. Sze, K.K. Ng, Physics of Semiconductor Devices, John Wiley & Sons, 2006.

[47] R. Hunger, R. Fritsche, B. Jaeckel, W. Jaegermann, L.J. Webb, N.S. Lewis, Chemical and electronic characterization of methyl-terminated Si(111) surfaces by high-resolution synchrotron photoelectron spectroscopy, Phys. Rev. B 72 (2005) 045317, https://doi.org/10.1103/PhysRevB.72.045317.

[48] E.A. Kraut, R.W. Grant, J.R. Waldrop, S.P. Kowalczyk, Precise determination of the valence-band edge in X-Ray photoemission spectra: application to measurement of semiconductor interface potentials, Phys. Rev. Lett. 44 (1980) 1620–1623, https://doi.org/10.1103/PhysRevLett.44.1620.

[49] E.A. Kraut, R.W. Grant, J.R. Waldrop, S.P. Kowalczyk, Semiconductor core-level to valence-band maximum binding-energy differences: precise determination by X-ray photoelectron spectroscopy, Phys. Rev. B 28 (1983) 1965–1977, https://doi.org/10.1103/PhysRevB.28.1965.

[50] C.C. Fulton, G. Lucovsky, R.J. Nemanich, Electronic states at the interface of Ti-Si oxide on Si(100), J. Vac. Sci. Technol. B: Microelectron. and Nanom. Struct. Process., Meas., and Phenom. 20 (4) (2002) 1726–1731, https://doi.org/10.1116/1.1493785, arXiv, https://avs.scitation.org/doi/pdf/10.1116/1.1493785, https://avs.scitation.org/doi/abs/10.1116/1.1493785.

[51] C.C. Fulton, G. Lucovsky, R.J. Nemanich, Process-dependent band structure changes of transition-metal (Ti,Zr,Hf) oxides on Si(100), Appl. Phys. Lett. 84 (4) (2004) 580–582, https://doi.org/10.1063/1.1639944.

[52] S.A. Campbell, D.C. Gilmer, X.-C. Wang, M.-T. Hsieh, H.-S. Kim, W.L. Gladfelter, J. Yan, MOSFET transistors fabricated with high permitivity TiO_2 dielectrics, IEEE Trans. Electron Devices 44 (1) (1997) 104–109, https://doi.org/10.1109/16.554800.